A VARIATIONAL MULTISCALE A-POSTERIORI ERROR ESTIMATION METHOD FOR NEARLY INCOMPRESSIBLE ELASTICITY

BY

TIMOTHY JAMES TRUSTER

THESIS

Submittal in partial fulfillment of the requirements
for the degree of Master of Science in Civil Engineering
in the Graduate College of the
University of Illinois at Urbana-Champaign, 2010

Urbana, Illinois

Advisor:

Professor Arif Masud

Abstract

This work presents an error estimation framework for a mixed displacement-pressure finite element method for nearly incompressible elasticity that is based on variational multiscale concepts. The displacement field is decomposed into coarse scales captured by the finite element mesh and fine scales representing the part of the physics unresolved by the mesh. This solution field decomposition addresses the artificial length scales resulting from discretization of a continuum problem at the variational level to produce a stabilized method equipped with naturally derived error estimators. Two error estimators are proposed. The first employs a representation by bubble functions that arises consistently during the development of the stabilized method and is computed by a simple, direct post-solution evaluation. The second involves solving the fine scale error equation through localization to overlapping patches spread across the domain. The performance of the stabilized method and the error estimators is investigated through numerical convergence tests conducted for two model problems on uniform and distorted meshes. The sharpness and robustness of the estimators is observed to be consistent across the simulations performed.

Acknowledgements

This work was made possible with the support of certain individuals and funding agencies. Many thanks to my advisor, Prof. Arif Masud, for his guidance, encouragement, and critiques during the development of this work. I also wish to acknowledge Prof. Lawrence Bergman and Prof. Andreas Polycarpou for their feedback on the methods proposed herein. This material is based upon work supported by the National Science Foundation under a Graduate Research Fellowship and under Grant No. 0800208. Any opinions, findings, conclusions or recommendations expressed in this publication are those of the author(s) and do not necessarily reflect the views of the National Science Foundation.

Table of Contents

List of Figures

List of Tables

Chapter 1: Introduction

Numerical methods are commonly employed to solve problems of engineering interest, and the finite element method has been invariably employed because of its mathematical robustness and its versatility of implementation. The general philosophy of the finite element method is to use the notion of discretization to subdivide the problem into simpler subregions, called elements, coupled with a simple set of shape functions to approximate the form of the true solution to the problem. Typically, this limited set of functions can capture the features of the solution that are larger than the diameter of any single element while they do a poor job at representing the finer features of the solution that fall within an element. Although the mesh can be refined and more functions can be added to this approximation set, certain components of the true solution may still be lost. This phenomenon is discretization error: the inability of a finite set of functions to represent an otherwise arbitrary function; this trait is universal among all numerical methods. Therefore, the two most important features of a finite element formulation are its ability to minimize the discretization error in the approximate solution computed on a given mesh and its ability to provide a measure of the error in the computed solution. This second feature is known as the field of a posteriori error estimation.

A variety of techniques has been and continues to be investigated that attempt to quantify the level of accuracy in numerically computed solutions. Historically, the investigation of error estimation began with a focus on elliptical boundary value problems as studied by Babuška and Rheinbolt [7]. Significant contributions following this work were presented by Zienkiewicz and Zhu [58] and Eriksson and Johnson [25]. As the field evolved, work was also conducted on mixed formulations for fluid and solid mechanics, of which representative sources include [16,55]. Fairly comprehensive reviews of error estimation are contained in the works of Ainsworth and Oden [2,3], Babuška and Strouboulis [10], and Verfürth [56].

Almost all frameworks for error estimation can be placed into one of three major categories based on the manner by which the error is evaluated:

1) *Explicit Methods*: These methods invoke equations involving the residuals of a governing equation evaluated in element interiors and across element boundaries. Typically the

finite element solution is employed directly without any additional projections or equation solving. While these estimators are relatively simple to compute, the expressions often include problem-dependent constants that can be approximated using dual problems [26]. These methods, also called residual-based methods, were proposed by Babuška and Rheinbolt [9]; later works include [6,13].

2) *Implicit Methods*: These techniques employ the finite element solution indirectly by posing residual-driven problems to be solved for the error. Often, a global error equation is approximated through localization to subdomains consisting of either individual elements or clusters of elements, respectively termed the Element Residual Method (ERM) and the Subdomain Residual Method (SRM). These methods offset increased complexity by providing improved levels of robustness. Some of the pioneering work was conducted by Babuška and Rheinbolt [7,8] and by Bank and Weiser [12]; more recent works include extensions to linear elasticity by Parés *et al*. [50] and Carstensen and Thiele [20].
3) *Recovery-based Methods*: These methods focus on post-processing the numerical solution to produce an enhanced reference solution. Typically, the difference between the discontinuous gradient field obtained directly from the finite element solution and a smoothed gradient field obtained through a projection operation is computed to provide an error estimate. These methods often inherit superconvergence properties from the smoothing projections. Fundamental contributions were provided by Zienkiewicz and Zhu [58,59], followed by [60,61]; more recent studies have conducted studies on irregular meshes [57] and used the estimators to evaluate quantities of interest [39].

Almost all of the above works focus on computing the error only after the numerical solution has been obtained. One of the first attempts to account for the effects of fine scales on a coarse approximation is presented by Oden in [49]. In their study of the advection-diffusion-reaction equation, they segregated the basis functions into coarse scale functions and fine scale functions by invoking the concept of mesh hierarchy. Then, they combined the fine scale functions with a secondary independent bilinear form to inspire the development of optimal coarse mesh trial and test functions. The resulting stiffness matrix was symmetric and well-conditioned, properties which do not hold for the standard formulations of advection-dominated problems. They also suggested that the fine scales represent the relative error between the optimal coarse mesh

solution and the solution obtained on a refined mesh. Thus, the incorporation of fine scales resulted in improved algorithmic properties and also provided a means to quantify the accuracy of a solution.

The concept of introducing a scale separation directly into the variational form for the purpose of modeling subgrid effects was made rigorous by Hughes in [35,38] and is referred to as the variational multiscale method (VMS). In this novel approach, a decomposition is applied to separate the solution field into resolved scales, which are captured by a given mesh, and unresolved scales, the finer features giving rise to discretization error, from the outset. This decomposition is introduced into the variational structure of the desired problem and gives rise to separate equations for the resolved and unresolved scales. This system of variational equations serves as a launching point for the derivation of enhanced numerical methods.

One of the applications of this method is to use the fine scale component either as an a posteriori error estimator or as a driving component for adaptive meshing algorithms. In [24], Elsheik *et al*. recast the classical techniques of the ERM and the SRM in a unified manner by starting from the fine scale equation and applying localization to solve the equation over elements or subdomains. They illustrated the performance of the framework for the Poisson problem and discussed conceptual benefits such as relaxation assumptions on boundary conditions for the subdomains. The performance of the fine scales as a residual-based error estimator has been studied by Hauke *et al.* in the context of the transport equation [31,32]. Their approach was to represent the fine scales using residual-free bubble functions to evaluate the error in various norms at the element level and across the domain in order to drive mesh adaptivity. While beginning with one-dimensional domains, the method has been extended to higher order elements and to higher dimensions [30,33]. Finally, Larson and Målqvist employed the variational multiscale method to develop an adaptive framework to solve problems possessing multiple scales [40,41,42]. They solved the variational system of equations in a staggered fashion and localized the fine scale equation on patches which are refined automatically as the error in both scales is monitored.

Another area of computational mechanics where VMS has led to significant contributions is stabilized methods. In particular, the model problem which we have selected for our study is the mixed formulation of elasticity, which is often the subject of stabilized methods. This formulation introduces a pressure field alongside the displacement field in order to model

incompressible phenomenon characterizing the behavior of rubber-like materials and metals undergoing plastic deformation. While this mixed formulation can overcome the volumetric-locking exhibited by the classical pure displacement method, it is also subject to the LBB inf-sup condition [5], which is a mathematical statement of the reduced stability of the pressure field. This numerical deficiency is manifested when certain combinations of displacement and pressure interpolations are employed and leads to unphysical pressure oscillations. Therefore, careful attention must be paid to design stable frameworks to avoid pathologic behavior. Further treatment of mixed formulations is given by Brezzi and Fortin [17]; other enlightening discussions are given in [14,15]. Out of the many remedies for instability which have been proposed, some focus on developing stable interpolation combinations for particular elements while others focus on enhancing the underlying numerical framework. A sampling of stable elements is contained in the following references: [22,34,4,53]. Noteworthy advancements of the latter approach include Brezzi and Pitkäranta [19] and Hughes *et al*. [37,27]. In recent years, stabilized formulations have been pursued through the application of the variational multiscale method to the mixed form of elasticity and the Stokes flow problem, which are form-equivalent in the incompressible limit. In [21], Codina presented equivalence between two methods for stabilizing the Stokes problem: pressure gradient projections and orthogonal sub-grid scales. For the second method, Codina employed a stabilization matrix in the fine scale equation which is approximated with mesh-dependent constants. In [46] and [48], Masud and co-workers applied the variational multiscale method to the mixed form of linear elasticity and derived the structure of the stabilization matrix $\boldsymbol{\tau}$ by employing bubble functions to represent the fine scales.

The purpose of this thesis is to present an error estimation framework for a mixed displacement-pressure finite element method that is based on variational multiscale concepts. Herein, a decomposition of the displacement field into coarse and fine scales serves as a point of departure for developing a stabilized solution procedure and subsequently generating natural a posteriori error estimators. As mentioned previously, the same fine scale features which are not captured by a crude discretization also tend to contribute to instability and locking phenomenon. The proposed formulation provides a mechanism to model these subgrid effects through residual or error based terms that arise consistently during the derivation of the fine scale equation. This mechanism ensures consistency and increases the accuracy of the formulation when the model for the fine scales is substituted back into the coarse scale problem, overcoming the lack of

stability in the standard Galerkin method. Once the coarse solution is obtained, the model for the subgrid effects can be revisited to evaluate the fine scales or error in the solution. The most obvious procedure is to simply compute the fine scales using the same approximation invoked for the purpose of stabilization, yielding an explicit error estimator. However, the fine scale equation could also be solved again using alternative representations of the fine scale component of displacement, leading to a class of implicit error estimators. Therefore, this method aims to both remedy the numerical deficiencies of the pure displacement formulation and quantify discretization error together within a unified, consistent framework through the modeling of fine scale effects.

We begin our discussion by posing the strong form of elasticity followed by a mixed form and the corresponding standard Galerkin form in Chapter 2. Next, we describe the application of the Hughes variational multiscale method to the standard Galerkin form and the resulting fine scale equation in Chapter 3. Chapter 4 provides a derivation of the stabilized form from the fine scale equation; Chapter 5 describes two methods for using the fine scale equation as a mechanism for estimating the discretization error. Finally, Chapter 6 presents numerical results for two standard benchmark problems, and conclusions are drawn in Chapter 7.

Chapter 2: Governing Equations

2.1 Strong Form

Let $\Omega \subset \mathbb{R}^{n_{sd}}$ be an open bounded domain with a piece-wise smooth boundary Γ, where $n_{sd} \geq 2$ is the number of spatial dimensions. The boundary Γ is divided into two subsets Γ_g and Γ_h on which Dirchlet and Neumann conditions are applied, respectively, and these subsets satisfy $\Gamma_g \cup \Gamma_h = \Gamma,\ \Gamma_g \cap \Gamma_h = \varnothing$. With these definitions, the governing equations of linear elasticity are:

$$\nabla \cdot \boldsymbol{\sigma} + \boldsymbol{b} = \boldsymbol{0} \qquad \text{in } \Omega \tag{2.1}$$

$$\boldsymbol{u} = \boldsymbol{g} \qquad \text{on } \Gamma_g \tag{2.2}$$

$$\boldsymbol{\sigma} \cdot \boldsymbol{n} = \boldsymbol{h} \qquad \text{on } \Gamma_h \tag{2.3}$$

where $\boldsymbol{u} : \Omega \to \mathbb{R}^{n_{sd}}$ represents the displacement field, $\boldsymbol{\sigma}$ is the Cauchy stress tensor, $\boldsymbol{b}$ is the body force, $\boldsymbol{g}$ is the prescribed displacement, $\boldsymbol{h}$ is the prescribed traction, and $\boldsymbol{n}$ is the unit outward normal on Γ. An isotropic constitutive model is assumed, where the relationship between $\boldsymbol{\sigma}$ and $\boldsymbol{u}$ is given as:

$$\boldsymbol{\varepsilon} = \boldsymbol{\varepsilon}(\boldsymbol{u}) = \tfrac{1}{2}\left(\nabla \boldsymbol{u} + (\nabla \boldsymbol{u})^T\right) \tag{2.4}$$

$$\boldsymbol{\sigma} = \lambda \operatorname{tr}\left[\boldsymbol{\varepsilon}(\boldsymbol{u})\right] + 2\mu \boldsymbol{\varepsilon}(\boldsymbol{u}) \tag{2.5}$$

where $\boldsymbol{\varepsilon}$ is the linearized strain tensor, λ and μ are the Lame parameters, and $\boldsymbol{I}$ is the second-order identity tensor. In the above and throughout this work, these conventions are used for vector and tensor operators: $\nabla(\cdot)$ represents the gradient, $\nabla \cdot (\cdot)$ is the divergence, $\Delta(\cdot)$ is the Laplacian, $\operatorname{tr}(\cdot)$ is the trace, and $(\cdot)^T$ is the transpose. As a function of the Young's modulus E and Poisson's ratio ν for the material, the Lame parameters are given as

$$\lambda = \frac{E\nu}{(1-2\nu)(1+\nu)},\ \mu = \frac{E}{2(1+\nu)} \tag{2.6}$$

To represent significant resistance to volume change exhibited by incompressible materials, the value of ν is taken nearly 0.5, which implies that $\lambda \to \infty$. This unbounded value of λ becomes a

source of numerical instability for standard displacement-based finite elements that manifests itself as volumetric locking [36]. To combat the unsatisfactory performance of the pure displacement formulation near the incompressible limit, an independent pressure field is introduced, which gives rise to the following mixed constitutive law and associated kinematic constraint:

$$\boldsymbol{\sigma} = p\boldsymbol{I} + 2\mu\boldsymbol{\varepsilon}(\boldsymbol{u}) \tag{2.7}$$

$$\nabla \cdot \boldsymbol{u} = p/\lambda \tag{2.8}$$

where $p : \Omega \to \mathbb{R}$ denotes the pressure field. While p does not correspond exactly to the hydrostatic stress, which is $\sigma = \mathrm{tr}(\boldsymbol{\sigma})/3$, it does reflect the volumetric behavior of the material.

Substituting (2.7) into (2.1) and (2.3) results in a set of governing equations capable of modeling the incompressible limit:

$$\nabla p + \nabla \cdot \left(2\mu\boldsymbol{\varepsilon}(\boldsymbol{u})\right) + \boldsymbol{b} = \boldsymbol{0} \qquad \text{in } \Omega \tag{2.9}$$

$$\nabla \cdot \boldsymbol{u} = p/\lambda \qquad \text{in } \Omega \tag{2.10}$$

$$\boldsymbol{u} = \boldsymbol{g} \qquad \text{on } \Gamma_g \tag{2.11}$$

$$\left[p\boldsymbol{I} + 2\mu\boldsymbol{\varepsilon}(\boldsymbol{u})\right] \cdot \boldsymbol{n} = \boldsymbol{h} \qquad \text{on } \Gamma_h \tag{2.12}$$

Both the displacement field $\boldsymbol{u}$ and the pressure field p are taken as unknowns to be determined in the solution process, and they must satisfy these equations at every point in Ω as well as satisfy the boundary conditions on Γ.

2.2 Weak Form

For the purpose of computing approximate solutions to boundary value problems such as elasticity, the governing equations are typically transformed into an equivalent expression called the weak or variational form. The general procedure is to relax the condition of pointwise satisfaction by multiplying each expression by a weighting function and integrating over the domain Ω, thereby allowing the solution to satisfy the governing equations in an integral sense. Therefore, this technique is called the method of weighted residuals, and details of its application can be bound in any standard finite element analysis textbook [36].

An important ingredient of this procedure is to select proper spaces of functions to which the trial solution and weighting functions belong. The function spaces appropriate for the displacement and pressure trial solutions and weighting functions are:

$$\mathcal{S} = \left\{ \boldsymbol{u} \middle| \boldsymbol{u} \in \left(H^1(\Omega) \right)^{n_{\text{sd}}}, \boldsymbol{u} = \boldsymbol{g} \text{ on } \Gamma_g \right\} \tag{2.13}$$

$$\mathcal{V} = \left\{ \boldsymbol{w} \middle| \boldsymbol{w} \in \left(H^1(\Omega) \right)^{n_{\text{sd}}}, \boldsymbol{w} = \boldsymbol{0} \text{ on } \Gamma_g \right\} \tag{2.14}$$

$$\mathcal{P} = \left\{ p \middle| p \in L_2(\Omega) \right\} \tag{2.15}$$

where $L_2(\Omega)$ and $H^1(\Omega)$ are standard Hilbertian-Sobolev spaces. The weak form corresponding to the governing equations can be expressed as: Find $\boldsymbol{u} \in \mathcal{S}$, $p \in \mathcal{P}$ such that for all $\boldsymbol{w} \in \mathcal{V}, q \in \mathcal{P}$:

$$\int_\Omega \nabla \boldsymbol{w} : \left[p\boldsymbol{I} + 2\mu\boldsymbol{\varepsilon}(\boldsymbol{u}) \right] \mathrm{d}\Omega = \int_\Omega \boldsymbol{w} \cdot \boldsymbol{b} \, \mathrm{d}\Omega + \int_{\Gamma_h} \boldsymbol{w} \cdot \boldsymbol{h} \, \mathrm{d}\Gamma \tag{2.16}$$

$$\int_\Omega q \left(\nabla \cdot \boldsymbol{u} - p/\lambda \right) \mathrm{d}\Omega = 0 \tag{2.17}$$

The next step in the classical approach is to extract finite dimensional subspaces of the trial and weighting function spaces on which the weak form is solved numerically to obtain an approximate solution; this process of restricting the infinite dimensional problem to a finite dimensional problem is called discretization.

While the standard weak form given in (2.16) and (2.17) is well-posed in the continuum setting, the process of discretization gives rise to non-trivial issues that need further consideration. First, the discretized form must satisfy the Ladyzenskaya–Babuška–Brezzi (LBB) inf-sup condition to ensure uniqueness and stability of the pressure field [5]. Various discussions of this criterion and its implications for numerical methods are included in [17,15]. This condition imposes additional constraints that a combination of displacement field and pressure field interpolations must satisfy in order to produce solutions which do not possess spurious oscillations in the pressure field. In particular, simple combinations such as equal-order polynomial interpolations may produce unstable discrete solutions [17,36].

Discretization also introduces an arbitrary filter that limits the resolution to which the solution fields can be determined. For example, the trial functions generated from a finite element mesh typically approximate well the characteristics of the true solution which span multiple elements but are unable to capture significant variations in the solution within a single element. Those

features of the continuum solution that are larger than the characteristic element length are resolvable scales, and smaller features are unresolved or subgrid scales. The inability of a given mesh to capture the subgrid scales results in discretization error.

Chapter 3: Variational Multiscale Method

In order to address the aspects of discretization discussed in Chapter 2, we employ the variational multiscale method as first proposed by Hughes [35,38]. The philosophy of this method is to assume that the primal field can be separated into components of varying scale and then substitute this decomposition directly into the weak form. While the continuum solution does not inherently possess scales, an artificial scale separation is induced by the limited resolution capacity of a spatial discretization. The variational multiscale method provides a mechanism to account for those features which would otherwise be lost in the numerical approximation. The motivation for using this method is two-fold: the derivation of a stabilized formulation and the development of an error-estimation framework. In the first case, assumptions are made on the form of the fine scale components in order to derive an expression to be injected into the coarse scale weak form with the goal of reducing the portion of the true solution lost to discretization error and thereby returning stability to the formulation. In the second case, an expression for the fine scales emanating from the weak form is evaluated using the computed numerical solution for the coarse scale in order to quantify the fine scales as a measure of the error.

3.1 Multiscale Decomposition

We begin by describing the process of discretization in the context of the finite element method. Consider a partition of the domain Ω into n_{umel} non-overlapping open subregions Ω^e, called finite elements, where $e = 1, 2, ..., n_{umel}$. Let Γ^e denote the boundary of element Ω^e, and let Ω' and Γ' denote the union of element interiors and element boundaries, respectively:

$$\Omega' = \bigcup_{e=1}^{n_{umel}} \Omega^e \tag{3.1}$$

$$\Gamma' = \bigcup_{e=1}^{n_{umel}} \Gamma^e \tag{3.2}$$

This partition satisfies the following closure property:

$$\bar{\Omega} = \text{closure}\left(\Omega'\right) \tag{3.3}$$

Finally, let $\Gamma_{\text{int}} = \Gamma' \setminus \Gamma$ denote the set of element boundaries on the interior of domain Ω.

Now, consider a multiscale overlapping decomposition of the displacement field into coarse and fine scales:

$$\boldsymbol{u} = \underbrace{\bar{\boldsymbol{u}}}_{\text{coarse scale}} + \underbrace{\boldsymbol{u}'}_{\text{fine scale}} \tag{3.4}$$

The coarse scales represent the component of the solution resolved by a given mesh, while the fine scales can be viewed as the relative component of error between the coarse scale and the exact solution; an example is given in Figure 1. In the context of the finite element method, the approximate solution computed using nodal shape functions plays the role of the coarse scale. However, since our goal is the development of a general framework, we postpone prescribing explicit sets of basis functions to the coarse or fine scales until later in the derivation. A similar decomposition is assumed for the weighting functions:

$$\boldsymbol{w} = \underbrace{\bar{\boldsymbol{w}}}_{\text{coarse scale}} + \underbrace{\boldsymbol{w}'}_{\text{fine scale}} \tag{3.5}$$

In the most general setting, an analogous multiscale separation could be applied to the pressure field. However, for simplicity, we neglect the fine scale component of the pressure field for this discussion.

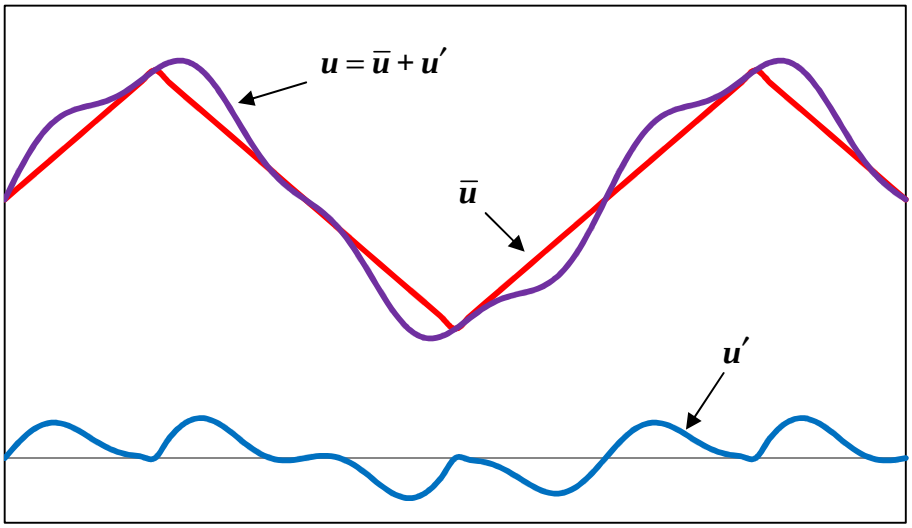

Figure 1. Multiscale decomposition of the total solution into coarse and fine scales

We define the appropriate spaces for $\bar{\boldsymbol{u}}$ and $\boldsymbol{u}'$ as

$$\bar{\mathcal{S}} = \left\{ \bar{\boldsymbol{u}} \middle| \bar{\boldsymbol{u}} \in C^0(\Omega) \cap \mathcal{S},\ \bar{\boldsymbol{u}}\big|_{\Omega^e} \in \mathcal{P}^k\left(\Omega^e\right) \text{ for } e = 1, 2, ..., n_{umel} \right\} \tag{3.6}$$

$$\mathcal{S}' = \left\{ \boldsymbol{u}' \middle| \boldsymbol{u}' \in \left(H^1(\Omega)\right)^{n_{sd}},\ \boldsymbol{u}' = \boldsymbol{0} \text{ on } \Gamma_g \right\} \tag{3.7}$$

where $\mathcal{P}^k\left(\Omega^e\right)$ denotes the set of complete polynomials of order *k* spanning Ω^e. The functions assumed for $\bar{\boldsymbol{u}}$ are permitted to be non-smooth across element boundaries, which will be an important consideration during the subsequent modification of the weak form (2.16) and (2.17). Additionally, for completeness, the functions representing $\boldsymbol{u}'$ are not assumed to vanish on element boundaries. While such an assumption is typical for stabilized variational multiscale methods, this generality will be important for error estimation. The relaxation that $\boldsymbol{u}' \neq \boldsymbol{0}$ on Γ is the major difference in the developments presented herein and in the study conducted in [46].

Similarly, the functions for the displacement weighting functions are

$$\bar{\mathcal{V}} = \left\{ \bar{\boldsymbol{w}} \middle| \bar{\boldsymbol{w}} \in C^0(\Omega) \cap \mathcal{V},\ \bar{\boldsymbol{w}}\big|_{\Omega^e} \in \mathcal{P}^k\left(\Omega^e\right) \text{ for } e = 1, 2, ..., n_{umel} \right\} \tag{3.8}$$

$$\mathcal{V}' = \mathcal{S}' \tag{3.9}$$

These spaces must satisfy $\mathcal{S} = \bar{\mathcal{S}} \oplus \mathcal{S}'$ and $\mathcal{V} = \bar{\mathcal{V}} \oplus \mathcal{V}'$, namely that the spaces are linearly independent. This ensures that the decomposition of $\boldsymbol{u}$ given in (3.4) is uniquely defined.

Furthermore, the strain tensor $\boldsymbol{\varepsilon}$ may be decomposed into coarse and fine scale components due to its linearity with respect to displacements. To simplify notation, the coarse and fine scale components will be represented by $\bar{\boldsymbol{\varepsilon}}$ and $\boldsymbol{\varepsilon}'$, respectively:

$$\bar{\boldsymbol{\varepsilon}} = \bar{\boldsymbol{\varepsilon}}\left(\bar{\boldsymbol{u}}\right) = \tfrac{1}{2}\left(\nabla \bar{\boldsymbol{u}} + \left(\nabla \bar{\boldsymbol{u}}\right)^T\right) \tag{3.10}$$

$$\boldsymbol{\varepsilon}' = \boldsymbol{\varepsilon}'\left(\boldsymbol{u}'\right) = \tfrac{1}{2}\left(\nabla \boldsymbol{u}' + \left(\nabla \boldsymbol{u}'\right)^T\right) \tag{3.11}$$

3.2 Multiscale Variational Problem

We now substitute the decomposed trial solutions and weighting functions of expressions (3.4) and (3.5) into the weak form (2.16) and (2.17) to give the multiscale variational problem:

$$\int_{\Omega'} \nabla\left(\bar{\boldsymbol{w}} + \boldsymbol{w}'\right) : \left[\, p\boldsymbol{I} + 2\mu\boldsymbol{\varepsilon}\left(\bar{\boldsymbol{u}} + \boldsymbol{u}'\right)\right] \mathrm{d}\Omega = \int_{\Omega'} \left(\bar{\boldsymbol{w}} + \boldsymbol{w}'\right) \cdot \boldsymbol{b}\, \mathrm{d}\Omega + \int_{\Gamma_h} \left(\bar{\boldsymbol{w}} + \boldsymbol{w}'\right) \cdot \boldsymbol{h}\, \mathrm{d}\Gamma \tag{3.12}$$

$$\int_{\Omega'} q\left(\nabla \cdot \left(\bar{\boldsymbol{u}} + \boldsymbol{u}'\right) - p/\lambda\right) \mathrm{d}\Omega = 0 \tag{3.13}$$

By observing that the above equations are linear with respect to the displacement weighting function, (3.12) and (3.13) can be separated into a coarse scale problem and fine scale problem:

Coarse Scale Problem $\mathcal{C}$

$$\int_{\Omega'} \nabla \bar{\boldsymbol{w}} : \left[p\boldsymbol{I} + 2\mu\boldsymbol{\varepsilon}\left(\bar{\boldsymbol{u}} + \boldsymbol{u}'\right)\right] \mathrm{d}\Omega = \int_{\Omega'} \bar{\boldsymbol{w}} \cdot \boldsymbol{b}\, \mathrm{d}\Omega + \int_{\Gamma_h} \bar{\boldsymbol{w}} \cdot \boldsymbol{h}\, \mathrm{d}\Gamma \tag{3.14}$$

$$\int_{\Omega'} q\left(\nabla \cdot \left(\bar{\boldsymbol{u}} + \boldsymbol{u}'\right) - p/\lambda\right) \mathrm{d}\Omega = 0 \tag{3.15}$$

Fine Scale Problem $\mathcal{F}$

$$\int_{\Omega'} \nabla \boldsymbol{w}' : \left[p\boldsymbol{I} + 2\mu\boldsymbol{\varepsilon}\left(\bar{\boldsymbol{u}} + \boldsymbol{u}'\right)\right] \mathrm{d}\Omega = \int_{\Omega'} \boldsymbol{w}' \cdot \boldsymbol{b}\, \mathrm{d}\Omega + \int_{\Gamma_h} \boldsymbol{w}' \cdot \boldsymbol{h}\, \mathrm{d}\Gamma \tag{3.16}$$

We now focus on the fine scale equation $\mathcal{F}$. This equation is infinite dimensional since no particular form has been assumed for the fine scale functions. Our goal will be to analyze (3.16) and extract a generalized representation for the fine scales which will serve as a reference point for developing a stabilized formulation and subsequently the error estimators.

3.3 Additional Notation

Before proceeding, we will define additional notation that will be used in subsequent derivations. As noted previously, the coarse component of displacement $\bar{\boldsymbol{u}}$ is permitted to be non-smooth across element boundaries; therefore, its derivatives may experience discontinuities. For the benefit of the reader, we shall elaborate on the proper application of integration by parts to fields experiencing discontinuities. For example, suppose that we wish to evaluate the following integral over a domain composed of two elements Ω^+ and Ω^-:

$$\int_{\Omega} \nabla \boldsymbol{w} : \boldsymbol{\varepsilon}\, \mathrm{d}\Omega = \int_{\Omega^+} \nabla \boldsymbol{w}^+ : \boldsymbol{\varepsilon}^+\, \mathrm{d}\Omega + \int_{\Omega^-} \nabla \boldsymbol{w}^- : \boldsymbol{\varepsilon}^-\, \mathrm{d}\Omega \tag{3.17}$$

where $\boldsymbol{w}$ is a displacement weighting function and $\boldsymbol{\varepsilon}$ is the linear strain tensor, and the $\pm$ superscript designates the element from which the decorated quantity is derived, as shown in Figure 2. A straightforward application of the divergence theorem (integration by parts) to each term on the right-hand side of (3.17) gives

$$\int_{\Omega^+} \nabla \boldsymbol{w}^+ : \boldsymbol{\varepsilon}^+\, \mathrm{d}\Omega = -\int_{\Omega^+} \boldsymbol{w}^+ \cdot \left(\nabla \cdot \boldsymbol{\varepsilon}^+\right) \mathrm{d}\Omega + \int_{\Gamma^+} \boldsymbol{w}^+ \cdot \left(\boldsymbol{\varepsilon}^+ \cdot \boldsymbol{n}^+\right) \mathrm{d}\Omega \tag{3.18}$$

$$\int_{\Omega^-} \nabla \boldsymbol{w}^- : \boldsymbol{\varepsilon}^-\, \mathrm{d}\Omega = -\int_{\Omega^-} \boldsymbol{w}^- \cdot \left(\nabla \cdot \boldsymbol{\varepsilon}^-\right) \mathrm{d}\Omega + \int_{\Gamma^-} \boldsymbol{w}^- \cdot \left(\boldsymbol{\varepsilon}^- \cdot \boldsymbol{n}^-\right) \mathrm{d}\Omega \tag{3.19}$$

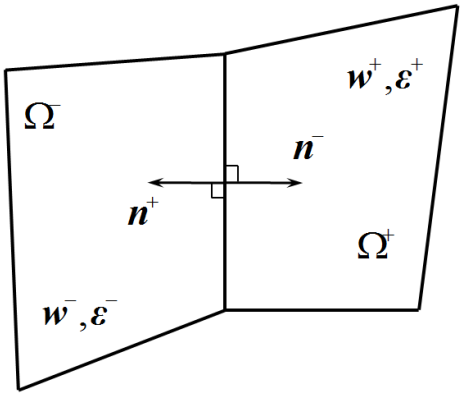

Figure 2. Depiction of unit outward normals on element interface

Along the shared interface boundary between the domains, Γ_i, the two boundary integrals may be combined:

$$\int_{\Gamma^+\cap\Gamma_i} \boldsymbol{w}^+\cdot\left(\boldsymbol{\varepsilon}^+\cdot\boldsymbol{n}^+\right)\mathrm{d}\Omega+\int_{\Gamma^-\cap\Gamma_i} \boldsymbol{w}^-\cdot\left(\boldsymbol{\varepsilon}^-\cdot\boldsymbol{n}^-\right)\mathrm{d}\Omega=\int_{\Gamma_i} \boldsymbol{w}\cdot\left[\boldsymbol{\varepsilon}^+\cdot\boldsymbol{n}^++\boldsymbol{\varepsilon}^-\cdot\boldsymbol{n}^-\right]\mathrm{d}\Omega \tag{3.20}$$

where we have used the fact that $\boldsymbol{w}^+=\boldsymbol{w}^-=\boldsymbol{w}$ on Γ_i because $\boldsymbol{w}$ is continuous everywhere in Ω. Considering the term in brackets and defining $\boldsymbol{n}=\boldsymbol{n}^+=-\boldsymbol{n}^-$, we observe that

$$\begin{aligned}\boldsymbol{\varepsilon}^+\cdot\boldsymbol{n}^++\boldsymbol{\varepsilon}^-\cdot\boldsymbol{n}^- &= \boldsymbol{\varepsilon}^+\cdot\boldsymbol{n}^+-\boldsymbol{\varepsilon}^-\cdot\boldsymbol{n}^+\\ &=\left(\boldsymbol{\varepsilon}^+-\boldsymbol{\varepsilon}^-\right)\cdot\boldsymbol{n}\end{aligned} \tag{3.21}$$

which vanishes only if $\boldsymbol{\varepsilon}^+=\boldsymbol{\varepsilon}^-$, which is not true when the strain field is discontinuous. This quantity represents the "jump" in the value of strain across element boundaries and is commonly expressed using the jump operator, denoted by $[\![\ \cdot\ ]\!]$, which is defined as

$$[\![\boldsymbol{\varepsilon}\cdot\boldsymbol{n}]\!]=\left(\boldsymbol{\varepsilon}^+-\boldsymbol{\varepsilon}^-\right)\cdot\boldsymbol{n} \tag{3.22}$$

We point out that (3.22) is invariant under a reassignment of the ± designations, and therefore represents a unique quantity. To conclude, we combine (3.18) - (3.22) into (3.17) and remove the superscripts to obtain:

$$\int_\Omega \nabla\boldsymbol{w}:\boldsymbol{\varepsilon}\,\mathrm{d}\Omega=-\int_\Omega \boldsymbol{w}\cdot\left(\nabla\cdot\boldsymbol{\varepsilon}\right)\mathrm{d}\Omega+\int_\Gamma \boldsymbol{w}\cdot\left(\boldsymbol{\varepsilon}\cdot\boldsymbol{n}\right)\mathrm{d}\Omega+\int_{\Gamma_i} \boldsymbol{w}\cdot[\![\boldsymbol{\varepsilon}\cdot\boldsymbol{n}]\!]\,\mathrm{d}\Omega \tag{3.23}$$

3.4 Analysis of Fine Scale Problem

Returning to the fine scale problem $\mathcal{F}$ and using the expressions for the components of strain (3.10) and (3.11), those terms depending only upon the fine scale quantities can be isolated from the coarse scale quantities:

$$\int_{\Omega'} \nabla \boldsymbol{w}' : (2\mu\boldsymbol{\varepsilon}') \, \mathrm{d}\Omega = -\int_{\Omega'} \nabla \boldsymbol{w}' : [\, p\boldsymbol{I} + 2\mu\bar{\boldsymbol{\varepsilon}}\,] \, \mathrm{d}\Omega + \int_{\Omega'} \boldsymbol{w}' \cdot \boldsymbol{b} \, \mathrm{d}\Omega + \int_{\Gamma_h} \boldsymbol{w}' \cdot \boldsymbol{h} \, \mathrm{d}\Gamma \tag{3.24}$$

Integration by parts will now be applied to the first term on the right-hand side of this equation. Because the fine scale functions do not vanish on Γ', this operation will give rise to boundary integrals; the result is:

$$-\int_{\Omega'} \nabla \boldsymbol{w}' : [\, p\boldsymbol{I} + 2\mu\bar{\boldsymbol{\varepsilon}}\,] \, \mathrm{d}\Omega = \int_{\Omega'} \boldsymbol{w}' \cdot \left[\nabla p + \nabla \cdot (2\mu\bar{\boldsymbol{\varepsilon}}) \right] \mathrm{d}\Omega - \int_{\Gamma'} \boldsymbol{w}' \cdot \left[\!\left[[\, p\boldsymbol{I} + 2\mu\bar{\boldsymbol{\varepsilon}}\,] \cdot \boldsymbol{n} \right]\!\right] \mathrm{d}\Gamma \tag{3.25}$$

Although the pressure field p is continuous in the present formulation, we point out that the jump term appearing in (3.25) arises in a consistent fashion from integration by parts and would accommodate more general formulations involving discontinuous approximations for p.

Recalling from (3.7) that $\boldsymbol{u}' = \boldsymbol{0}$ on Γ_g, we may substitute (3.25) into $\mathcal{F}$ to obtain the following result:

$$\begin{aligned} \int_{\Omega'} \nabla \boldsymbol{w}' : (2\mu\boldsymbol{\varepsilon}') \, \mathrm{d}\Omega = & \int_{\Omega'} \boldsymbol{w}' \cdot \left[\nabla p + \nabla \cdot (2\mu\bar{\boldsymbol{\varepsilon}}) \right] \mathrm{d}\Omega + \int_{\Omega'} \boldsymbol{w}' \cdot \boldsymbol{b} \, \mathrm{d}\Omega \\ & + \int_{\Gamma_h} \boldsymbol{w}' \cdot \left\{ \boldsymbol{h} - [\, p\boldsymbol{I} + 2\mu\bar{\boldsymbol{\varepsilon}}\,] \cdot \boldsymbol{n} \right\} \mathrm{d}\Gamma \\ & - \int_{\Gamma_{\mathrm{int}}} \boldsymbol{w}' \cdot \left[\!\left[[\, p\boldsymbol{I} + 2\mu\bar{\boldsymbol{\varepsilon}}\,] \cdot \boldsymbol{n} \right]\!\right] \mathrm{d}\Gamma \end{aligned} \tag{3.26}$$

We now make the important observation that the right-hand side of (3.26) is entirely a function of the residual of the Euler-Lagrange equations (2.9) with respect to the coarse scale displacement and boundary residuals representing the satisfaction of the traction boundary condition (2.12) and point-wise continuity of the stress field across Γ'. To clarify, we introduce the following definitions:

$$\boldsymbol{r}_{\Omega'} = \nabla p + \nabla \cdot (2\mu\bar{\boldsymbol{\varepsilon}}) + \boldsymbol{b} \tag{3.27}$$

$$\boldsymbol{r}_{\Gamma_h} = \boldsymbol{h} - [\, p\boldsymbol{I} + 2\mu\bar{\boldsymbol{\varepsilon}}\,] \cdot \boldsymbol{n} \tag{3.28}$$

$$\boldsymbol{r}_{\Gamma_{\mathrm{int}}} = -\left[\!\left[[\, p\boldsymbol{I} + 2\mu\bar{\boldsymbol{\varepsilon}}\,] \cdot \boldsymbol{n} \right]\!\right] \tag{3.29}$$

Substituting these definitions into (3.26) gives:

Fine Scale Equation $\mathcal{F}_r$

$$\int_{\Omega'} \nabla \boldsymbol{w}' : (2\mu\boldsymbol{\varepsilon}') \, \mathrm{d}\Omega = \int_{\Omega'} \boldsymbol{w}' \cdot \boldsymbol{r}_{\Omega'} \, \mathrm{d}\Omega + \int_{\Gamma_h} \boldsymbol{w}' \cdot \boldsymbol{r}_{\Gamma_h} \, \mathrm{d}\Gamma + \int_{\Gamma_{\mathrm{int}}} \boldsymbol{w}' \cdot \boldsymbol{r}_{\Gamma_{\mathrm{int}}} \, \mathrm{d}\Gamma \tag{3.30}$$

This compact form represents a paradigm for both the construction of a stabilized formulation and of error estimators for the coarse scale quantities. Since all terms depending on the fine scale trial displacement functions have been isolated on the left-hand side of (3.30), we can see that the fine scales are in essence driven by the residuals of the coarse scale variables. Thus, the fine scales vanish exactly under the conditions expected: when the coarse scale exactly satisfies the governing equations and the residuals identically vanish everywhere in Ω. This fact is central to the consistency of the resultant stabilized formulation in Section 4 and to the validatity of the error estimators in Section 5.

3.5 Analytical Solution of Fine Scale Equation

To conclude our analysis of $\mathcal{F}_r$, we invoke the theory of Green's functions for linear partial differential equations (PDEs) in order to derive a general expression for $\boldsymbol{u}'$. Details of Green's functions can be found in many textbooks on PDEs [29,54]. The fundamental concept is the following: given the strong form of a PDE, the solution can be immediately written down in an integral expression using only the associated Green's function and supplied problem data. For example, consider the following strong form:

$$\mathcal{L}(u) = -f(\boldsymbol{x}) \qquad \text{for } \boldsymbol{x} \in \Omega, \qquad u = 0 \qquad \text{for } \boldsymbol{x} \in \partial\Omega \tag{3.31}$$

where $\mathcal{L}$ is a linear differential operator and $f(\boldsymbol{x})$ is a forcing function. Then the exact solution is given by

$$u(\boldsymbol{x}) = -\int_{\Omega} g(\boldsymbol{x}, \boldsymbol{y}) \, f(\boldsymbol{y}) \, \mathrm{d}\Omega \qquad \text{for } \boldsymbol{x} \in \Omega \tag{3.32}$$

where $g(\boldsymbol{x}, \boldsymbol{y})$ is the Green's function of operator $\mathcal{L}$, which can be found by solving the following equation:

$$\mathcal{L}^*\left(g(\boldsymbol{x}, \boldsymbol{y})\right) = -\delta(\boldsymbol{x} - \boldsymbol{y}) \qquad \text{for } \boldsymbol{x} \in \Omega, \qquad g(\boldsymbol{x}, \boldsymbol{y}) = 0 \quad \text{for } \boldsymbol{x} \in \partial\Omega \tag{3.33}$$

where $\delta(\cdot)$ is the Dirac-delta function and $\mathcal{L}^*$ is the adjoint of $\mathcal{L}$. This general theory holds for vector-valued PDEs as well and can be applied to analyze the fine scale problem. Considering the form of (3.30), we can write the associated strong form as:

$$\nabla \cdot (2\mu \boldsymbol{\varepsilon}') = -\boldsymbol{r}_{\Omega'} \qquad \text{in } \Omega' \tag{3.34}$$

$$[2\mu \boldsymbol{\varepsilon}'] \cdot \boldsymbol{n} = -\boldsymbol{r}_{\Gamma_h} \qquad \text{on } \Gamma_h \tag{3.35}$$

$$[\![2\mu \boldsymbol{\varepsilon}' \cdot \boldsymbol{n}]\!] = -\boldsymbol{r}_{\Gamma_{\text{int}}} \qquad \text{on } \Gamma_{\text{int}} \tag{3.36}$$

$$\boldsymbol{u} = \boldsymbol{0} \qquad \text{on } \Gamma_g \tag{3.37}$$

The first two equations (3.34) and (3.35) show that $\boldsymbol{u}'$ is driven by the coarse scale residuals of the equilibrium equation (2.9) and the traction boundary condition (2.12); the third equation states that the jump in the fine scale stresses should balance the jump in coarse scale stresses.

In lieu of (3.32), the exact expression for the fine scale solution $\boldsymbol{u}'$ is given by

$$\begin{aligned} \boldsymbol{u}'(\boldsymbol{x}) = &-\int_{\Omega'} \boldsymbol{g}'(\boldsymbol{x},\boldsymbol{y}) \cdot \boldsymbol{r}_{\Omega'}(\boldsymbol{y}) \, \mathrm{d}\Omega_y - \int_{\Gamma_h} \boldsymbol{g}'(\boldsymbol{x},\boldsymbol{y}) \cdot \boldsymbol{r}_{\Gamma_h}(\boldsymbol{y}) \, \mathrm{d}\Gamma_y \\ &- \int_{\Gamma_{\text{int}}} \boldsymbol{g}'(\boldsymbol{x},\boldsymbol{y}) \cdot \boldsymbol{r}_{\Gamma_{\text{int}}}(\boldsymbol{y}) \, \mathrm{d}\Gamma_y \end{aligned} \tag{3.38}$$

In the above, $\boldsymbol{g}'(\boldsymbol{x},\boldsymbol{y})$ is the Green's function for the fine scale problem, in this case a second order tensor.

While the concept of a Green's function is fairly straightforward, deriving a closed-form expression for $\boldsymbol{g}'(\boldsymbol{x},\boldsymbol{y})$ is often much harder than directly finding the solution for $\boldsymbol{u}'$. However, in their discussion of the variational multiscale method, Hughes observed that the modeling assumptions applied to $\boldsymbol{u}'$ can ultimately be linked to making approximations to the form of $\boldsymbol{g}'(\boldsymbol{x},\boldsymbol{y})$ [38]. Also, by analyzing the form of (3.38) and considering $\boldsymbol{u}'$ as the error between $\boldsymbol{u}$ and $\bar{\boldsymbol{u}}$, we may infer that each of the residual terms $\boldsymbol{r}_{\Omega'}$, $\boldsymbol{r}_{\Gamma_h}$, and $\boldsymbol{r}_{\Gamma_{\text{int}}}$ acts as a source of error, while the Green's function $\boldsymbol{g}'(\boldsymbol{x},\boldsymbol{y})$ serves as a distributor of error. For certain classes of problems such as nodally-exact formulations for one-dimensional boundary value problems, $\boldsymbol{g}'(\boldsymbol{x},\boldsymbol{y})$ has been linked to so-called residual-free bubbles [18]. This fact was utilized by Hauke *et al.* in their error estimation techniques using the fine scales [31]. Therefore, our subsequent derivations using the fine scale equation can be viewed in light of making approximations to the Green's function.

Chapter 4: Stabilized Formulation

The main objective of this section is to use the fine scale equation $\mathcal{F}_r$ to determine an analytical expression for $\boldsymbol{u}'$ that can be substituted into the coarse scale problem $\mathcal{C}$. This will be accomplished by making simplifying assumptions on the functional form of the fine scales. This functional form will be substituted into (3.30) in order to rearrange and solve for $\boldsymbol{u}'$. This technique is more insightful than directly approximating $\boldsymbol{g}'$ in (3.38). In this way, the explicit appearance of $\boldsymbol{u}'$ as an independent field will be removed from $\mathcal{C}$; however, the presence of additional terms will implicitly account for their effects, thereby stabilizing the resulting modified coarse scale problem. These derivations follow along the lines of the derivation in [46,48].

4.1 Solution to Fine Scale Equation

Toward the goal of solving (3.30), we now make the simplifying assumption that the fine scale functions vanish on element boundaries, namely:

$$\boldsymbol{u}' = \boldsymbol{0} \quad \text{on } \Gamma', \qquad \boldsymbol{w}' = \boldsymbol{0} \quad \text{on } \Gamma' \tag{4.1}$$

One consequence of this assumption is that second and third terms on the right-hand side of (3.30) vanish identically, which dramatically simplifies the equation. Since the remaining terms are integrals over element interiors Ω', (3.30) can be evaluated as a sum of integrals in an element-by-element fashion:

$$\int_{\Omega^e} \nabla \boldsymbol{w}' : (2\mu\boldsymbol{\varepsilon}') \, \mathrm{d}\Omega = \int_{\Omega^e} \boldsymbol{w}' \cdot \boldsymbol{r}_{\Omega'} \, \mathrm{d}\Omega \qquad \text{for each } e = 1, 2, \ldots, n_{umel} \tag{4.2}$$

This equation can now be solved independently within each element of the mesh. While a multi-dimensional basis could be used to represent the fine scales, a single basis function typically provides a sufficient approximation for the purpose of stabilization. Therefore, in each element we represent the fine scales by the following expressions:

$$\boldsymbol{u}'\big|_{\Omega^e} = b^e(\boldsymbol{\xi})\boldsymbol{\beta} \qquad \rightarrow \qquad u_i'\big|_{\Omega^e} = b^e(\boldsymbol{\xi})\beta_i \quad \text{on } \Omega^e \tag{4.3}$$

$$\boldsymbol{w}'\big|_{\Omega^e} = b^e(\boldsymbol{\xi})\boldsymbol{\gamma} \qquad \rightarrow \qquad w_i'\big|_{\Omega^e} = b^e(\boldsymbol{\xi})\gamma_i \quad \text{on } \Omega^e \tag{4.4}$$

where $b^e(\boldsymbol{\xi})$ denotes the bubble shape function over element domain Ω^e, as shown in Figure 3, $i = 1, 2, ..., n_{sd}$, and $\boldsymbol{\beta}$ and $\boldsymbol{\gamma}$ represent the scaling coefficients for the fine scale trial solutions and weighting functions, respectively. The following section discusses bubble functions in greater depth. In general, a bubble function is any interpolating or basis function that is zero on the entire boundary of an element. These functions are chosen to satisfy the characteristics of $\boldsymbol{u}'$ as specified by (3.7) and (4.1).

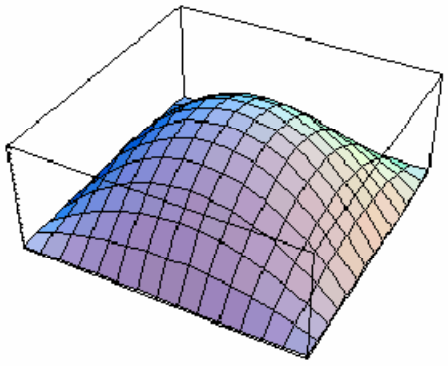

Figure 3. Quadratic polynomial bubble function on a typical quadrilateral element

Substituting these forms of $\boldsymbol{u}'$ and $\boldsymbol{w}'$ into the quantity inside the integral on the left-hand side of (4.2), we can derive an expression that is valid in each element of the discretization:

$$\begin{aligned}\nabla \boldsymbol{w}' : \boldsymbol{\varepsilon}' &= \boldsymbol{w}' : \tfrac{1}{2}\left(\nabla \boldsymbol{u}' + (\nabla \boldsymbol{u}')^T\right) \\ &= \left(\boldsymbol{\gamma} \otimes \nabla b^e\right) : \left(\boldsymbol{\beta} \otimes \nabla b^e + \nabla b^e \otimes \boldsymbol{\beta}\right) \\ &= \tfrac{1}{2}\left[\left(\nabla b^e \cdot \nabla b^e\right)\mu \boldsymbol{\gamma}^T \boldsymbol{\beta} + \boldsymbol{\gamma}^T \mu \left(\nabla b^e \otimes \nabla b^e\right)\boldsymbol{\beta}\right] \\ &= \tfrac{1}{2}\boldsymbol{\gamma}^T\left[\left(\nabla b^e \cdot \nabla b^e\right)\mu \boldsymbol{I} + \mu\left(\nabla b^e \otimes \nabla b^e\right)\right]\boldsymbol{\beta}\end{aligned} \tag{4.5}$$

Using this expression with (4.3) and (4.4), we may rewrite (4.2) as

$$\boldsymbol{\gamma}^T\left[\int_{\Omega^e}\left(\nabla b^e \cdot \nabla b^e\right)\mu \boldsymbol{I} + \mu\left(\nabla b^e \otimes \nabla b^e\right)\mathrm{d}\Omega\right]\boldsymbol{\beta} = \boldsymbol{\gamma}^T \int_{\Omega^e} b^e \boldsymbol{r}_{\Omega'}\mathrm{d}\Omega \tag{4.6}$$

where the vectors of constant coefficients have been factored out of the integrals. Since this equation must be valid for all admissible weighting functions, the vector $\boldsymbol{\gamma}$ must be arbitrary, and consequently we have

$$\boldsymbol{\beta} = \boldsymbol{K}^{-1}\boldsymbol{R} \tag{4.7}$$

where $\boldsymbol{K}$ and $\boldsymbol{R}$ are defined as follows:

$$\boldsymbol{K} = \int_{\Omega^e} \left(\nabla b^e \cdot \nabla b^e \right) \mu \boldsymbol{I} + \mu \left(\nabla b^e \otimes \nabla b^e \right) \mathrm{d}\Omega \tag{4.8}$$

$$\boldsymbol{R} = \int_{\Omega^e} b^e \boldsymbol{r}_{\Omega'} \mathrm{d}\Omega \tag{4.9}$$

Substituting (4.7) into (4.3) gives an analytical expression for $\boldsymbol{u}'$:

$$\boldsymbol{u}'\big|_{\Omega^e} = b^e(\boldsymbol{\xi}) \boldsymbol{K}^{-1} \boldsymbol{R} \tag{4.10}$$

Based on our assumptions, this expression is valid within each element and expresses a relationship between the fines scales $\boldsymbol{u}'$ and the coarse scale residual $\boldsymbol{r}_{\Omega'}$.

Finally, in order to write (4.10) in a form analogous to traditional stabilized methods, we assume a projection that extracts the mean value of $\boldsymbol{r}_{\Omega'}$ over element interiors. From a practical viewpoint, on a sufficiently refined mesh, $\boldsymbol{r}_{\Omega'}$ will be essentially constant on the interior of each element. Therefore, we may approximate (4.9) by taking the residual out of the integral:

$$\boldsymbol{R} \approx \left(\int_{\Omega^e} b^e \mathrm{d}\Omega \right) \boldsymbol{r}_{\Omega'} \tag{4.11}$$

Making this substitution into (4.10), we arrive at a succinct expression for the fine scale displacement $\boldsymbol{u}'$ in each element:

$$\boldsymbol{u}'\big|_{\Omega^e} = \boldsymbol{\tau} \boldsymbol{r}_{\Omega'} \tag{4.12}$$

where $\boldsymbol{\tau}$ is a second-order stabilization tensor with the following form:

$$\boldsymbol{\tau} = \left(b^e \int_{\Omega^e} b^e \mathrm{d}\Omega \right) \left[\left(\int_{\Omega^e} \mu \nabla b^e \cdot \nabla b^e \mathrm{d}\Omega \right) \boldsymbol{I} + \int_{\Omega^e} \mu \nabla b^e \otimes \nabla b^e \mathrm{d}\Omega \right]^{-1} \tag{4.13}$$

Therefore, under our assumptions, we conclude that $\boldsymbol{u}'$ is a function of the shear modulus μ, the bubble function b^e, and the residual of the equilibrium equation $\boldsymbol{r}_{\Omega'}$. We can also determine the approximation of $\boldsymbol{g}'$ resulting from this method. By comparing (4.12) and (4.13) with the general formula for $\boldsymbol{u}'$ (3.38), we can deduce that our approximate fine scale Green's function $\tilde{\boldsymbol{g}}'$ is given by the following expression:

$$\begin{aligned} \tilde{\boldsymbol{g}}' &= -\left\{ b^e(\boldsymbol{x}) \int_{\Omega^e} b^e \mathrm{d}\Omega \right\} \left[\left(\int_{\Omega^e} \mu \nabla b^e \cdot \nabla b^e \mathrm{d}\Omega \right) \boldsymbol{I} + \int_{\Omega^e} \mu \nabla b^e \otimes \nabla b^e \mathrm{d}\Omega \right]^{-1} \delta(\boldsymbol{y} - \boldsymbol{x}) \\ &= -\boldsymbol{\tau}(\boldsymbol{x}) \delta(\boldsymbol{y} - \boldsymbol{x}) \end{aligned} \tag{4.14}$$

Indeed, by substituting (4.14) into (3.38) and using the definition of $\delta(\cdot)$, we obtain

$$\begin{aligned}\boldsymbol{u}'(\boldsymbol{x}) &\approx -\int_{\Omega'} \tilde{\boldsymbol{g}}'(\boldsymbol{x},\boldsymbol{y})\cdot\boldsymbol{r}_{\Omega'}(\boldsymbol{y})\,\mathrm{d}\Omega_y - \int_{\Gamma_h}\boldsymbol{0}\cdot\boldsymbol{r}_{\Gamma_h}(\boldsymbol{y})\,\mathrm{d}\Gamma_y - \int_{\Gamma_{\mathrm{int}}}\boldsymbol{0}\cdot\boldsymbol{r}_{\Gamma_{\mathrm{int}}}(\boldsymbol{y})\,\mathrm{d}\Gamma_y \\ &= -\int_{\Omega'}\left[-\boldsymbol{\tau}(\boldsymbol{x})\delta(\boldsymbol{y}-\boldsymbol{x})\right]\cdot\boldsymbol{r}_{\Omega'}(\boldsymbol{y})\,\mathrm{d}\Omega_y \\ &= \boldsymbol{\tau}(\boldsymbol{x})\boldsymbol{r}_{\Omega'}(\boldsymbol{x})\end{aligned} \tag{4.15}$$

which is exactly equation (4.12). This formula is analogous to the expression given by Hughes in their discussion of stabilized methods in section 7 of [38]. This approximation replaces the nonlocal character of $\boldsymbol{g}'$ within an element by a purely local one.

4.2 Discussion of Bubble Functions

In this section, we briefly elaborate on the characteristics of bubble functions. The minimum requirements for a function b^e to be a valid basis function for $\boldsymbol{u}'$ used for the purpose of stabilization is that it must belong to the following set $\widehat{\mathcal{S}}'_e$, which is a subset of $\mathcal{S}'$:

$$\widehat{\mathcal{S}}'_e = \left\{\boldsymbol{u}' \,\middle|\, \boldsymbol{u}'(\boldsymbol{x}) = \boldsymbol{0}\ \forall\ \boldsymbol{x} \notin \Omega^e\right\} \tag{4.16}$$

This simply states that b^e is nonzero only in element Ω^e and has square-integrable first partial derivatives. A more detailed procedure to ensure that a bubble function satisfies the patch test is provided in [48]. Simple choices for bubble functions are higher-order Lagrange or hierarchical polynomial functions that vanish on element boundaries; however, more sophisticated functions are possible. Bubble functions have been used extensively over the years in the analysis of mixed methods to produce stable elements. One of the first such elements was the MINI element, proposed by Arnold *et al*. [4]. Discussions about bubble functions in the context of mixed methods and associated proofs of stability are given in [17]. Another popular class of functions is the residual-free bubbles, which are designed to satisfy the governing partial differential equation at each point in an element. A sampling of references on this topic are [11,28]. Other procedures for designing bubble functions were explored by Masud and Franca in the context of problems with multiscale source terms [44] and by Masud and Kwack in the case of the advection-diffusion equation [45].

The bubble functions used for this implementation are given by the expressions shown in Table 1 in terms of element natural coordinates (ξ,η). The element type abbreviations designate the shape of the element, either triangular (T) or quadrilateral (Q), and the number of nodes per element, varying between 3 and 9.

Table 1. Bubble functions employed for stabilization

Element	Bubble Function
T3	$\xi\eta(1-\xi-\eta)$
Q4	$(1-\xi^2)(1-\eta^2)$
T6	$\xi\eta(1-\xi-\eta)$
Q9	$16\xi^2\eta^2(1-\xi^2)(1-\eta^2)$

These bubble functions are fairly standard and simple polynomial functions. A nonstandard bubble function was used for the Q9 elements in order to satisfy the linear independence property and because it provided improved accuracy for the problems investigated compared to the following bubble function:

$$b^e(\boldsymbol{\xi}) = (1-\xi^4)(1-\eta^4) \tag{4.17}$$

4.3 Solution to Coarse Scale Problem

We will now prepare (3.14) and (3.15) for substitution of (4.12) in place of $\boldsymbol{u}'$ to eliminate its explicit appearance. To do so, we will isolate those terms involving $\boldsymbol{u}'$ and apply integration by parts wherever necessary to remove derivatives. Beginning with (3.14), we employ the decomposition of strain given by (3.10) and (3.11) to separate the term on the left-hand side of (3.14) and obtain:

$$\int_{\Omega'} \nabla\bar{\boldsymbol{w}}:[\,p\boldsymbol{I} + 2\mu\bar{\boldsymbol{\varepsilon}}\,]\,\mathrm{d}\Omega + \int_{\Omega'} 2\mu(\nabla\bar{\boldsymbol{w}}:\boldsymbol{\varepsilon}')\,\mathrm{d}\Omega = \int_{\Omega'} \bar{\boldsymbol{w}}\cdot\boldsymbol{b}\,\mathrm{d}\Omega + \int_{\Gamma_h} \bar{\boldsymbol{w}}\cdot\boldsymbol{h}\,\mathrm{d}\Gamma \tag{4.18}$$

Focusing on the second term in (4.18), by recalling that $\boldsymbol{u}' = \boldsymbol{0}$ on Γ' and recalling the identity $\nabla\boldsymbol{a}:\boldsymbol{\varepsilon}(\boldsymbol{b}) = \boldsymbol{\varepsilon}(\boldsymbol{a}):\nabla\boldsymbol{b}$ which holds for all vector fields $\boldsymbol{a}$ and $\boldsymbol{b}$, we may integrate by parts to obtain:

$$\int_{\Omega'} 2\mu(\nabla\bar{\boldsymbol{w}}:\boldsymbol{\varepsilon}')\,\mathrm{d}\Omega = -\int_{\Omega'} 2\mu\left[\nabla\cdot\boldsymbol{\varepsilon}(\bar{\boldsymbol{w}})\right]\cdot\boldsymbol{u}'\,\mathrm{d}\Omega \tag{4.19}$$

Substituting the expression for $\boldsymbol{u}'$ (4.12) into (4.19) gives:

$$-\int_{\Omega'} 2\mu\left[\nabla\cdot\boldsymbol{\varepsilon}(\bar{\boldsymbol{w}})\right]\cdot\boldsymbol{u}'\,\mathrm{d}\Omega = -\int_{\Omega'} 2\mu\left[\nabla\cdot\boldsymbol{\varepsilon}(\bar{\boldsymbol{w}})\right]\cdot\boldsymbol{\tau}\boldsymbol{r}_{\Omega'}\,\mathrm{d}\Omega \tag{4.20}$$

Now returning to (3.15), employ the decomposition of $\boldsymbol{u}$ given by (3.4) to rewrite this equation as

$$\int_{\Omega'} q(\nabla\cdot\bar{\boldsymbol{u}} - p/\lambda)\,\mathrm{d}\Omega + \int_{\Omega'} q\nabla\cdot\boldsymbol{u}'\,\mathrm{d}\Omega = 0 \tag{4.21}$$

Considering the second term, we may integrate by parts and substitute (4.12) to obtain:

$$\int_{\Omega'} q\nabla\cdot\boldsymbol{u}'\,\mathrm{d}\Omega = -\int_{\Omega'}\nabla q\cdot\boldsymbol{u}'\,\mathrm{d}\Omega = -\int_{\Omega'}\nabla q\cdot\boldsymbol{\tau}\boldsymbol{r}_{\Omega'}\,\mathrm{d}\Omega \tag{4.22}$$

Inserting (4.20) into (4.18) and (4.22) into (4.21), the coarse scale problem $\mathcal{C}$ can be written in the following modified form:

Modified Coarse Scale Problem $\mathcal{M}$

$$\int_{\Omega'}\nabla\bar{\boldsymbol{w}}:\left[p\boldsymbol{I}+2\mu\bar{\boldsymbol{\varepsilon}}\right]\mathrm{d}\Omega-\int_{\Omega'}2\mu\left[\nabla\cdot\boldsymbol{\varepsilon}\left(\bar{\boldsymbol{w}}\right)\right]\cdot\boldsymbol{\tau}\boldsymbol{r}_{\Omega'}\mathrm{d}\Omega=\int_{\Omega'}\bar{\boldsymbol{w}}\cdot\boldsymbol{b}\,\mathrm{d}\Omega+\int_{\Gamma_h}\bar{\boldsymbol{w}}\cdot\boldsymbol{h}\,\mathrm{d}\Gamma \tag{4.23}$$

$$\int_{\Omega'}q\left(\nabla\cdot\bar{\boldsymbol{u}}-p/\lambda\right)\mathrm{d}\Omega-\int_{\Omega'}\nabla q\cdot\boldsymbol{\tau}\boldsymbol{r}_{\Omega'}\,\mathrm{d}\Omega=0 \tag{4.24}$$

4.4 The HVM Form

We may combine (4.23) and (4.24) to obtain a single expression that represents the HVM formulation for incompressible elasticity. Since all fine scale terms have been explicitly eliminated from the equations, the superimposed bars on the coarse scale terms will be dropped for simplicity. Rearranging the terms and introducing the expression for $\boldsymbol{r}_{\Omega'}$ from (3.27), we obtain:

$$\begin{aligned}\int_{\Omega'}\nabla\boldsymbol{w}:\left[p\boldsymbol{I}+2\mu\boldsymbol{\varepsilon}\left(\boldsymbol{u}\right)\right]\mathrm{d}\Omega+\int_{\Omega'}q\left(\nabla\cdot\boldsymbol{u}-p/\lambda\right)\mathrm{d}\Omega&\\ -\int_{\Omega'}\left[\nabla q+2\mu\nabla\cdot\boldsymbol{\varepsilon}\left(\boldsymbol{w}\right)\right]\cdot\boldsymbol{\tau}\left[\nabla p+2\mu\nabla\cdot\boldsymbol{\varepsilon}\left(\boldsymbol{u}\right)\right]\mathrm{d}\Omega&\\ =\int_{\Omega'}\boldsymbol{w}\cdot\boldsymbol{b}\,\mathrm{d}\Omega+\int_{\Gamma_h}\boldsymbol{w}\cdot\boldsymbol{h}\,\mathrm{d}\Gamma+\int_{\Omega'}\left[\nabla q+2\mu\nabla\cdot\boldsymbol{\varepsilon}\left(\boldsymbol{w}\right)\right]\cdot\boldsymbol{\tau}\boldsymbol{b}\,\mathrm{d}\Omega&\end{aligned} \tag{4.25}$$

The last terms on the left-hand and right-hand side have appeared due to the assumption of fine scales in the problem. These terms account for the subgrid scales that would otherwise have been filtered out by a given discretization. Therefore, they provide improved accuracy and stability to the formulation; consequently, the method accommodates arbitrary combinations of interpolations for the displacement and pressure fields. Since the stabilization terms are residual based, this method is consistent; when the coarse scales represent the total solution, the residual of the Euler-Lagrange equations vanishes identically, and we recover the standard Galerkin form (2.16) and (2.17). Finally, we emphasize that the structure of the stabilization tensor $\boldsymbol{\tau}$ was derived based on a variational principle and therefore is not an explicit function of the characteristic mesh parameter *h* or any other user-defined parameter.

The process of finding numerical solutions to the HVM form proceeds along the same line as the traditional finite element method. First, we consider the approximation $\boldsymbol{u} \approx \boldsymbol{u}^h$ and expand $\boldsymbol{u}^h$ in terms of shape functions defined over elements Ω^e for each $e = 1, 2, ..., n_{umel}$. The integrals in (4.25) are then evaluated in each element using this expansion, and these quantities are assembled into a system of equations that is solved to determine the coefficients of the shape functions. The only distinguishing feature of the HVM formulation from an implementation perspective is that there are additional integrals to evaluate, but these do not require any additional parameters that are not already assigned to each element in traditional methods. Therefore, the only modification to an existing code would be to add the new terms from (4.25). To facilitate such an implementation, explicit formulas for each term are provided in Appendix A.

Chapter 5: Error Estimation

Having addressed the issue of stability, our current objective is now to analyze the performance of the fine scales as an error estimator. As mentioned previously, the fine scale displacement $\boldsymbol{u}'$ represents the component of the exact solution that is unaccounted for in the coarse scale $\bar{\boldsymbol{u}}$ on a particular level of discretization, where $\bar{\boldsymbol{u}} \approx \boldsymbol{u}^h$ is the typical finite element solution. Returning to the decomposition of $\boldsymbol{u}$ in (3.4), we claim that the fine scales can exactly represent the error between the coarse solution and the exact solution:

$$\boldsymbol{e} = \boldsymbol{u} - \bar{\boldsymbol{u}} = \boldsymbol{u}' \tag{5.1}$$

This claim is true when the multiscale problem is solved exactly; namely, the true pressure field p is obtained along with both $\bar{\boldsymbol{u}}$ and $\boldsymbol{u}'$. While equality with the true error is lost in the discrete setting, the fine scales can still serve as a valid approximation for the error. Specifically, a good approximation to $\boldsymbol{u}'$ should be a good approximation to $\boldsymbol{e}$.

In order to quantify the performance of $\boldsymbol{u}'$ as an estimator, we will invoke the concept of an effectivity index I_{eff}. This concept is commonly used in the academic community to compare error estimators [3]. It is defined as the ratio between the predicted error and the true error as measured in an appropriate norm for the problem:

$$I_{\text{eff}} = \frac{\left\| \text{Predicted error} \right\|}{\left\| \text{True error} \right\|} \tag{5.2}$$

In general, a norm is an aggregate measure of the magnitude of a field. For this mixed formulation, we have elected to use the L_2 norm and H^1 seminorm, which are defined for an arbitrary vector field $\boldsymbol{v}$ (e.g. $\boldsymbol{u}$ or p) as

$$\left\| \boldsymbol{v} \right\|_{L_2(\omega)} = \sqrt{\int_\omega \boldsymbol{v} \cdot \boldsymbol{v} \, \mathrm{d}\Omega} \tag{5.3}$$

$$\left| \boldsymbol{v} \right|_{H^1(\omega)} = \sqrt{\int_\omega \nabla \boldsymbol{v} : \nabla \boldsymbol{v} \, \mathrm{d}\Omega} \tag{5.4}$$

where ω is the domain of integration, typically either a single element Ω^e or the entire domain Ω. In the latter case, we will abbreviate notation as follows: $\left\| \boldsymbol{v} \right\|_{L_2(\Omega)} = \left\| \boldsymbol{v} \right\|_{L_2}$ and $\left| \boldsymbol{v} \right|_{H^1(\Omega)} = \left| \boldsymbol{v} \right|_{H^1}$.

We are especially concerned with the following local error indicators η^e computed from the fine scale in each element as:

$$\eta^e = \left|\boldsymbol{u}'\right|_{H^1(\Omega^e)} \tag{5.5}$$

These local quantities can be agglomerated into a single global error indicator η:

$$\eta = \left\{ \sum_{e=1}^{n_{umel}} \left(\eta^e\right)^2 \right\}^{\frac{1}{2}} \tag{5.6}$$

Finally, we may define the associated local and global effectivity indices as

$$I_{\text{eff}}^e = \eta^e, \; I_{\text{eff}} = \eta \tag{5.7), (5.8}$$

As the value of the error indicator approaches the true error, these ratios will tend to one. Therefore, a desirable property of an estimator would be for this ratio to remain close to 1 regardless of the problem being solved or the resolution of a mesh. More precisely, an estimator is considered efficient if the ratio can be bounded above and below regardless of the finite element partition of the domain. It is considered robust if the ratio is bounded above and below independent of problem-specific data such as material properties or boundary conditions.

In section 5.1, we investigate the performance of the fine scale field given by (4.12) as an explicit error indicator. Then, we return to the fine scale equation $\mathcal{F}_r$ in section 5.2 to derive an implicit error estimator.

5.1 Explicit a Posteriori Error Indicator

Recall the analytical form derived for $\boldsymbol{u}'$ given by (4.12) and (4.13). Within each element of the mesh, these expressions depend only upon the element bubble function b^e, material properties, and the residual of the governing equations $\boldsymbol{r}_{\Omega'}$ (3.27). Once the modified coarse scale problem $\mathcal{M}$ has been solved numerically for $\bar{\boldsymbol{u}}$ and *p*, this expression can be directly evaluated in each element. This evaluation amounts to a simple post-processing step; thus, the fine scale field $\boldsymbol{u}'$ from the HVM formulation can be considered as an explicit error indicator. Typical explicit residual-based estimates contain unknown constants that can be found through solving dual problems [26]. In the present case, the stabilization tensor $\boldsymbol{\tau}$ is serving as an approximation of this constant, an approximation that was consistently derived from the governing equations. Thus, the HVM formulation comes equipped with an error estimator that does not require any

additional mechanisms to evaluate beyond those already utilized in the solution process. The formula for this error indicator using the H^1 seminorm is

$$\eta_{\text{exp}}^e = \left|\boldsymbol{u}'\right|_{H^1\left(\Omega^e\right)} \tag{5.9}$$

where

$$\begin{aligned}\nabla \boldsymbol{u}' &= \left(\nabla \boldsymbol{\tau}\right)\boldsymbol{r}_{\Omega'} \\ &= \nabla b^e \left(\int_{\Omega^e} b^e \mathrm{d}\Omega\right)\left[\left(\int_{\Omega^e} \mu \nabla b^e \cdot \nabla b^e \mathrm{d}\Omega\right)\boldsymbol{I} + \int_{\Omega^e} \mu \nabla b^e \otimes \nabla b^e \mathrm{d}\Omega\right]^{-1} \boldsymbol{r}_{\Omega'}\end{aligned} \tag{5.10}$$

The performance of this approximation of $\boldsymbol{u}'$ will be assessed in the numerical simulations in Chapter 6. However, we give two preliminary remarks:

- This method provides a very simple procedure that is merely a post-processing step after the main solution phase.
- The accuracy of this method depends upon the validity of the assumption that $\boldsymbol{u}' = \boldsymbol{0}$ on Γ', $\boldsymbol{r}_{\Omega'}$ is constant on element interiors, and the ability of b^e to represent $\boldsymbol{u}'$.

5.2 Alternative Approach: Localization of Fine Scale Problem

With the aim of computing an improved representation of $\boldsymbol{u}'$, we return to the fine scale equation $\mathcal{F}_r$. Once the coarse scale quantities have been obtained from the modified coarse scale problem $\mathcal{M}$, $\boldsymbol{u}'$ becomes the only unknown. Therefore, we treat the fine scale equation $\mathcal{F}_r$ as a problem to be solved numerically for $\boldsymbol{u}'$. Noting that solving (3.30) numerically by a direct scheme would be very computationally intensive, we seek to develop an approximate technique to decouple the fine scale equations into a number of localized problems over smaller domains.

To this end, we adapt a method proposed by Larson and Målqvist [42] for the multiscale approximation of the Poisson problem. Their method was designed to solve problems that possess a large disparity of scales in the solution fields due to high frequency oscillations of the material parameters spatially across the domain. It involves solving for localized components of the fine scale on overlapping regions spread throughout the domain so that a series of small problems are solved rather than one large problem. The concept of localized Dirchlet problems has been used previously for a posteriori error estimation of scalar problems by Morin *et al*. [47]. In what follows, we extend these ideas to the mixed formulation of elasticity and demonstrate the performance of simple polynomial functions as approximations of the local fine scale spaces.

We begin by recalling the partitioning of domain Ω into finite elements given by (3.1) - (3.3). Let $\mathcal{N}$ denote the set of coarse nodes on the corners of the elements in Ω'. Let $\{\varphi_i\}_{i\in\mathcal{N}}$ be a partition of unity (POU) over Ω; in general, a partition of unity is a set of functions which satisfy the following property:

$$\sum_{i\in\mathcal{N}} \varphi_i(\boldsymbol{x}) = 1 \quad \forall\, \boldsymbol{x}\in\Omega \tag{5.11}$$

The partition of unity functions may also be assigned other desirable properties such as compact support and nonnegativity. The concept of a POU is central to the Generalized Finite Element Method; one recent reference by Duarte *et al.* provides a discussion of partition of unity in that context [23]. For our purposes, the first-order Lagrange basis functions associated with the coarse nodes $\mathcal{N}$ will be used. Employing this partition of unity in the first term on the right-hand side of (3.30), we obtain:

$$\int_{\Omega'} \boldsymbol{w}'\cdot\boldsymbol{r}_\Omega \,\mathrm{d}\Omega = \int_{\Omega'} \boldsymbol{w}'\cdot\left(\sum_{i\in\mathcal{N}}\varphi_i\right)\boldsymbol{r}_\Omega \,\mathrm{d}\Omega = \int_{\Omega'} \boldsymbol{w}'\cdot\left(\sum_{i\in\mathcal{N}}\varphi_i\boldsymbol{r}_\Omega\right)\mathrm{d}\Omega = \sum_{i\in\mathcal{N}}\left[\int_{\Omega'}\boldsymbol{w}'\cdot\varphi_i\boldsymbol{r}_\Omega\,\mathrm{d}\Omega\right] \tag{5.12}$$

Using similar arguments, we may rewrite (3.23) as:

$$\int_{\Omega'}\nabla\boldsymbol{w}' : (2\mu\boldsymbol{\varepsilon}')\,\mathrm{d}\Omega = \sum_{i\in\mathcal{N}}\left[\int_{\Omega'}\boldsymbol{w}'\cdot\varphi_i\boldsymbol{r}_\Omega\,\mathrm{d}\Omega + \int_{\Gamma_h}\boldsymbol{w}'\cdot\varphi_i\boldsymbol{r}_{\Gamma_h}\,\mathrm{d}\Gamma + \int_{\Gamma_{\mathrm{int}}}\boldsymbol{w}'\cdot\varphi_i\boldsymbol{r}_{\Gamma_{\mathrm{int}}}\,\mathrm{d}\Gamma\right] \tag{5.13}$$

Equation (5.13) represents an exact equality due to the partition of unity property.

We then separate $\boldsymbol{u}'$ into components such that each component is given by:

$$\boldsymbol{u}' = \sum_{i\in\mathcal{N}}\boldsymbol{u}_i' \tag{5.14}$$

$$\begin{aligned}\int_{\Omega'}\nabla\boldsymbol{w}' : (2\mu\boldsymbol{\varepsilon}(\boldsymbol{u}_i'))\,\mathrm{d}\Omega = {} & \int_{\Omega'}\boldsymbol{w}'\cdot\varphi_i\boldsymbol{r}_{\Omega'}\,\mathrm{d}\Omega + \int_{\Gamma_h}\boldsymbol{w}'\cdot\varphi_i\boldsymbol{r}_{\Gamma_h}\,\mathrm{d}\Gamma \\ & + \int_{\Gamma_{\mathrm{int}}}\boldsymbol{w}'\cdot\varphi_i\boldsymbol{r}_{\Gamma_{\mathrm{int}}}\,\mathrm{d}\Gamma \quad \text{for each } i\in\mathcal{N}\end{aligned} \tag{5.15}$$

Thus, each component is given by the solution to the associated decoupled equation resulting from (5.13). This decoupled set of equations is equivalent to $\mathcal{F}_r$ because each equation is posed over the entire domain Ω.

We now discuss an approximate method of solving (5.15). To each node $i\in\mathcal{N}$, we associate a domain ω_i, referred to subsequently as a patch or subdomain, consisting of the elements in a neighborhood around node *i*. Specifically, let $\omega_{i,1}$ be the union of elements in the support of the

Lagrange basis function centered at node *i*, namely, all of the elements connected to node *i*. Let $\mathcal{N}_1^i$ be the set of all nodes attached to those elements in $\omega_{i,1}$. Then we define ω_i to be

$$\omega_i = \omega_{i,2} = \bigcup_{j \in \mathcal{N}_1^i} \omega_{j,1} \tag{5.16}$$

In [42], Larson and Målqvist describe $\omega_{i,2}$ as a level 2 mesh star around node *i*. They also observe that level 1 mesh starts, $\omega_{i,1}$, are too restrictive within their proposed framework and do not accurately capture the fine scale components because of the boundary conditions prescribed to the patches, described shortly. We have observed similar behavior in our studies, and therefore have opted for the use of patches defined by (5.16). Larger patches can be defined recursively by the following formula:

$$\omega_{i,L} = \bigcup_{j \in \mathcal{N}_{L-1}^i} \omega_{j,1} \tag{5.17}$$

where $\mathcal{N}_L^i$ is the set of all nodes attached to elements in $\omega_{i,L}$. However, for the purpose of error estimation, we have found a level 2 star as defined in (5.16) to be sufficient. Finally, we denote the union of element boundaries which lie in ω_i as

$$\Gamma_i' = \bigcup_{\Omega^e \in \omega_i} \Gamma^e \tag{5.18}$$

and we define the set of element boundaries on the interior of ω_i as $\Gamma_{i,\text{int}}' = \Gamma_i' \setminus \partial\omega_i$, where $\partial\omega_i$ is the boundary of the patch.

We define the appropriate fine scale displacement trial solution and weighting function spaces as:

$$\mathcal{S}_{\omega_i}' = \left\{ \boldsymbol{u}_i' \middle| \boldsymbol{u}_i' \in \mathcal{S}',\ \boldsymbol{u}_i' = \mathbf{0} \text{ in } \Omega \setminus \omega_i,\ \boldsymbol{u}_i' = \mathbf{0} \text{ on } \partial\omega_i \setminus \left(\partial\omega_i \cap \Gamma_h \right) \right\} \tag{5.19}$$

$$\mathcal{V}_{\omega_i}' = \mathcal{S}_{\omega_i}' \tag{5.20}$$

In words, fine scale component $\boldsymbol{u}_i'$ is a function from the fine scale space $\mathcal{S}'$ that vanishes outside patch ω_i and also satisfies homogenous Dirchlet boundary conditions on the boundary of the patch which is not part of the Neumann boundary of domain Ω. This definition of the spaces for the components $\boldsymbol{u}_i'$ ensures that the total fine scale solution $\boldsymbol{u}'$ given by (5.14) will be continuous everywhere. With these definitions, the approximate fine scale equation becomes:

$$\int_{\omega_i} \nabla \boldsymbol{w}_i' : \left(2\mu\boldsymbol{\varepsilon}\left(\boldsymbol{u}_i'\right)\right) \mathrm{d}\Omega = \int_{\omega_i} \boldsymbol{w}_i' \cdot \boldsymbol{\varphi}_i \boldsymbol{r}_{\Omega'} \, \mathrm{d}\Omega + \int_{\partial\omega_i \cap \Gamma_h} \boldsymbol{w}_i' \cdot \boldsymbol{\varphi}_i \boldsymbol{r}_{\Gamma_h} \, \mathrm{d}\Gamma + \int_{\Gamma_{i,\mathrm{int}}'} \boldsymbol{w}_i' \cdot \boldsymbol{\varphi}_i \boldsymbol{r}_{\Gamma_{\mathrm{int}}} \, \mathrm{d}\Gamma \qquad \text{for each } i \in \mathcal{N} \tag{5.21}$$

This approximation is reasonable if the value of $\boldsymbol{u}'$ within any particular element is not significantly influenced by the value of the coarse scale residual at a location further away than one or two element diameters. Our numerical studies have shown that approximation is valid for the HVM formulation given by (4.25).

5.3 Implicit a Posteriori Error Estimator

In order to obtain a finite element approximation of (5.21), we consider a partition of each element Ω^e into non-overlapping subregions ω_e^c, which we will call cells, in direct analogy to (3.1) - (3.3). Namely:

$$\bar{\Omega}^e = \mathrm{closure}\left(\bigcup_{c=1}^{n_{cell}} \omega_e^c \right) \tag{5.22}$$

where $c = 1, 2, ..., n_{cell}$ and n_{cell} denotes the number of cells per element, which we assume is the same for each element. However, we also require that this partitioning results in a conforming discretization along element boundaries Γ_{int}. With these definitions, we may denote the union of cell interiors ω_i' within a particular subdomain ω_i as the collection of all cells within each element Ω^e that is contained in that subdomain:

$$\omega_i' = \bigcup_{\Omega^e \in \omega_i} \left(\bigcup_{c=1}^{n_{cell}} \omega_e^c \right) \tag{5.23}$$

Figure 4 shows two typical subdomains on a sample finite element mesh.

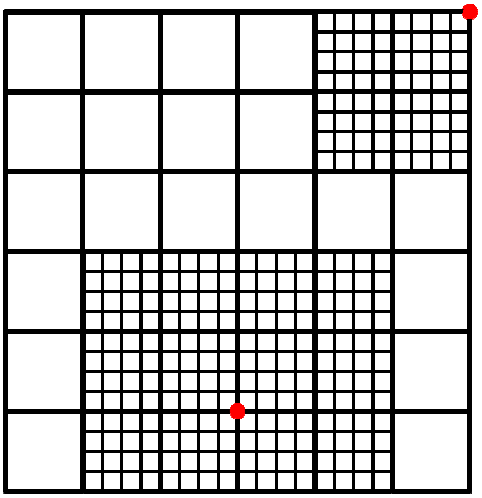

Figure 4. Example of subdomain refinement on a mesh; nodes associated with domains are highlighted

We now discuss the approximate finite element subspaces of (5.19) and (5.20). The partition of ω_i given by (5.22) suggests an analogy with typical *h*-refinement schemes; therefore, we adopt the simple approximation for $\boldsymbol{u}_i'$ as piecewise-continuous polynomials of the same degree *k* as the coarse mesh. In order to ensure the linear independence of $\bar{\boldsymbol{u}}$ and $\boldsymbol{u}'$, we require that the fine scale functions vanish identically at the coarse nodes:

$$\mathcal{S}_{\omega_i}^h = \left\{ \begin{array}{l} \boldsymbol{u}_i^h \,\middle|\, \boldsymbol{u}_i^h \in C^0\left(\omega_i\right) \cap \mathcal{S}_{\omega_i}',\ \boldsymbol{u}_i^h\big|_{\omega_e^c} \in \mathcal{P}^k\left(\omega_e^c\right) \text{ for } c = 1, 2, \ldots, n_{cell}, \\ \quad \boldsymbol{u}_i^h\left(\boldsymbol{x}_j\right) = \boldsymbol{0}\ \forall\ j \in \mathcal{N}_1^i \end{array} \right\} \tag{5.24}$$

$$\mathcal{V}_{\omega_i}^h = \mathcal{S}_{\omega_i}^h \tag{5.25}$$

where $\boldsymbol{x}_j$ are the physical coordinates of node *j*. With these definitions in place, the implicit method for a posteriori error estimation using the fine scales is given by: Find $\boldsymbol{u}' = \sum_{i \in \mathcal{N}} \boldsymbol{u}_i^h$ where $\boldsymbol{u}_i^h \in \mathcal{S}_{\omega_i}^h$ such that

$$\begin{aligned} \int_{\omega_i'} \nabla \boldsymbol{w}_i^h : \left(2\mu\boldsymbol{\varepsilon}\left(\boldsymbol{u}_i^h\right)\right) \mathrm{d}\Omega = & \int_{\omega_i'} \boldsymbol{w}_i^h \cdot \varphi_i \boldsymbol{r}_\Omega \,\mathrm{d}\Omega + \int_{\partial\omega_i \cap \Gamma_h} \boldsymbol{w}_i^h \cdot \varphi_i \boldsymbol{r}_{\Gamma_h} \,\mathrm{d}\Gamma \\ & + \int_{\Gamma_{i,\mathrm{int}}'} \boldsymbol{w}_i^h \cdot \varphi_i \boldsymbol{r}_{\Gamma_{\mathrm{int}}} \,\mathrm{d}\Gamma \qquad \text{for all } \boldsymbol{w}_i^h \in \mathcal{V}_{\omega_i}^h \text{ and } i \in \mathcal{N} \end{aligned} \tag{5.26}$$

Similar to (4.12), this method can be used to obtain both local and global estimates of the error in the coarse scale solution. The formula for this error estimator using the H^1 seminorm is

$$\eta_{\text{imp}}^e = \left|\boldsymbol{u}'\right|_{H^1(\Omega^e)} \tag{5.27}$$

While this method is more computationally intensive, its robustness is enhanced by the relaxation of the assumption $\boldsymbol{u}' = \boldsymbol{0}$ on Γ'.

The specific discretization scheme just described is only one of many ways in which the fine scale equation $\mathcal{F}_r$ could be decoupled and approximated. For example, *p*-hierarchical functions could be used to represent the fine scales rather than building the space using equal-order functions defined over cells. Other options include varying the size of patches and increasing the refinement of the fine scale by adding more cells or higher-order functions. Finally, there is the possibility of eliminating certain elements from the decoupled problems if the value of the explicit error obtained in them was below a specified tolerance. The only modification required would be to ignore those elements during the implicit solution phase and prescribe homogeneous Dirchlet boundary conditions on elements bordering them; this would result in a smooth approximation of $\boldsymbol{u}'$ when coupled with the explicit portion of $\boldsymbol{u}'$ obtained using bubble functions. In Chapter 6, the effects of increasing the number of cells in each element are explored for one family of numerical simulations.

At a higher level, one could consider applying the POU concept to the alternative form of the fine scale equation given by (3.24). While the method presented above involves directly the residuals of the governing equation or strong form, this approach utilizes the integrated-by-parts or weak form of the residual, which is less consistent with traditional error estimation techniques but is nevertheless a valid formulation. We refer to these as the strong variant and weak variant of the error estimator, respectively. Sparing the details of the derivation, which proceed along similar lines as described in section 5.2, the approximate fine scale equation analogous to (5.21) but using the weak variant is given by:

$$\begin{aligned}\int_{\omega_i} \nabla \boldsymbol{w}_i' : \left(2\mu\boldsymbol{\varepsilon}\left(\boldsymbol{u}_i'\right)\right) \mathrm{d}\Omega = &-\int_{\omega_i} \nabla \boldsymbol{w}_i' : \varphi_i \left[\, p\boldsymbol{I} + 2\mu\bar{\boldsymbol{\varepsilon}} \right] \mathrm{d}\Omega + \int_{\omega_i} \boldsymbol{w}_i' \cdot \varphi_i \boldsymbol{b}\, \mathrm{d}\Omega \\ &+ \int_{\partial\omega_i \cap \Gamma_h} \boldsymbol{w}_i' \cdot \varphi_i \boldsymbol{h}\, \mathrm{d}\Gamma \qquad\qquad \text{for each } i \in \mathcal{N}\end{aligned} \tag{5.28}$$

Employing the discrete spaces presented in (5.24) and (5.25), the discrete form of the weak variant is given by:

$$\int_{\omega_i'} \nabla \boldsymbol{w}_i^h : \left(2\mu \boldsymbol{\varepsilon}\left(\boldsymbol{u}_i^h \right) \right) \mathrm{d}\Omega = -\int_{\omega_i'} \nabla \boldsymbol{w}_i^h : \varphi_i \left[p\boldsymbol{I} + 2\mu \bar{\boldsymbol{\varepsilon}} \right] \mathrm{d}\Omega + \int_{\omega_i'} \boldsymbol{w}_i^h \cdot \varphi_i \boldsymbol{b}\, \mathrm{d}\Omega + \int_{\partial\omega_i \cap \Gamma_h} \boldsymbol{w}_i^h \cdot \varphi_i \boldsymbol{h}\, \mathrm{d}\Gamma \qquad \text{for all } \boldsymbol{w}_i^h \in \mathcal{V}_{\omega_i}^h \text{ and } i \in \mathcal{N} \tag{5.29}$$

While equations (3.24) and (3.30) are exactly equivalent, (5.26) and (5.29) produce slightly different approximations due to the effect of localization. Specifically, if ω_i is extended to Ω for all $i \in \mathcal{N}$ and both (5.26) and (5.29) are solved numerically using the same discretization in the patches and full numerical integration, etc., the approximate solutions are identical, as is discussed in section 6.4. Two of the main benefits from using the weak variant are that second derivatives of shape functions are not required and that boundary integrals are only performed on the domain traction boundaries. One observation about both methods is that the form of the decomposition of $\boldsymbol{u}'$ implies that the decoupled equations can naturally be solved in parallel.

Another important feature of both variants can be concluded by recalling the definition of the POU $\{\varphi_i\}_{i \in \mathcal{N}}$. Since these functions are defined using element-based linear Lagrange polynomial basis functions, we may observe that φ_i indeed possesses the compact support property:

$$\varphi_i(\boldsymbol{x}) = 0 \;\; \forall \boldsymbol{x} \notin \omega_{i,1}; \quad \varphi_i(\boldsymbol{x}) = 0 \;\; \forall \boldsymbol{x} \in \partial\omega_{i,1} \tag{5.30}$$

Therefore, the only nonzero contributions to the right-hand side of (5.26) and (5.29) come from cells interiors and boundaries within elements of $\omega_{i,1}$ rather than all of ω_i. This feature can be exploited in the numerical implementation.

Chapter 6: Numerical Simulations

To analyze the performance of the HVM formulation and the error estimation techniques, we present numerical results for prototypical problems on a variety of meshes. Convergence studies are performed for two problems using Lagrangian linear and quadratic triangular and quadrilateral elements with equal-order interpolations for the displacement and pressure fields; this family of elements is shown in Figure 5. All quantities computed during the solution and error estimation phases are fully integrated using appropriate quadrature rules. The numerical framework has been implemented in a FORTRAN research code called FEAP; the contour plots shown were generated from the numerical output using MATLAB.

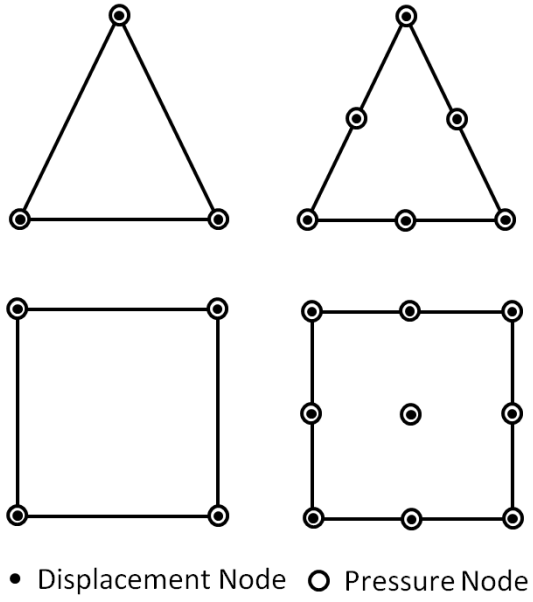

Figure 5. Family of continuous equal-order Lagrangian elements

Unless stated otherwise, all of the calculations of the implicit fine scale error were performed on patches ω_i defined by (5.16). A submesh was created within each element of the patch, consisting of four cells. The cells were generated by bisecting each edge of the parent element and drawing lines between these points. An example of submeshes for a triangular and a quadrilateral element are shown in Figure 6 below. This procedure provides sufficient refinement, enforces conformity between elements, and maintaines aspect ratios.

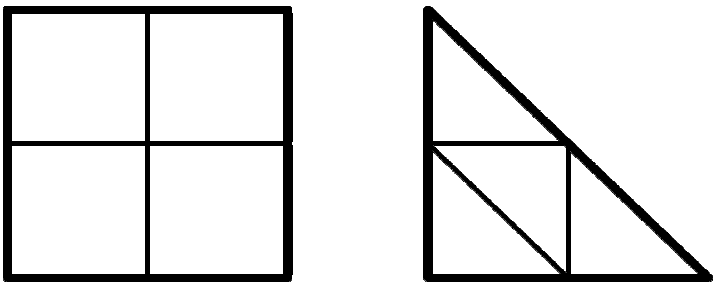

Figure 6. Submesh of cells within a triangular and quadrilateral element

6.1 Cantilever Beam Problem Description

The first simulation is of a cantilever beam loaded by a parabolic edge shear. This problem typically serves as a benchmark for numerical methods for elasticity. Plane strain conditions are assumed for this problem, as these conditions are more stringent to satisfy near the incompressible limit. The description of the problem is shown in Figure 6; the exact solution derived from elasticity theory is given in (6.1)-(6.3) [52].

Figure 7. Cantilever beam problem description

$$u_x^{\text{exact}} = -\frac{P\left(1-\nu^2\right)y}{6EI}\left[\left(6L-3x\right)x+\left(2+\frac{\nu}{1-\nu}\right)\left(y^2-C^2\right)\right] \tag{6.1}$$

$$u_y^{\text{exact}} = \frac{P\left(1-\nu^2\right)}{6EI}\left[\left(L-x\right)\frac{3\nu y^2}{1-\nu}+\left(4+5\frac{\nu}{1-\nu}\right)C^2x+\left(3L-x\right)x^2\right] \tag{6.2}$$

$$p^{\text{exact}} = -Py\nu\left(L-x\right) \tag{6.3}$$

$$I = \frac{\left(2C\right)^3}{12} \tag{6.4}$$

The values of parameters selected for the simulation were:

$$P = 2560 \quad C = 1 \qquad L = 10 \qquad I = 8/12 \qquad E = 7.5\times10^{7} \quad \nu = 0.4999 \tag{6.5}$$

6.2 Convergence Study: Uniform Meshes

In order to verify the convergence of the method with respect to this particular problem, the numerical solution was computed on sets of uniformly refined meshes. The mesh hierarchy is shown in Table 2; examples of two successive meshes obtained by bisection for triangular and quadrilateral elements are shown in Figure 8. In keeping with standard conventions, we refer to the numerical solutions for displacement and pressure as $\boldsymbol{u}^h$ and p^h, respectively.

Table 2. Listing of number of elements and nodes in mesh hierarchy

Mesh Name	Triangular (T3)		Quadrilateral (Q4)		Triangular (T6)		Quadrilateral (Q9)	
	Elements	Nodes	Elements	Nodes	Elements	Nodes	Elements	Nodes
Coarse	40	33	20	33	40	105	20	105
Medium	160	105	80	105	160	369	80	369
Fine	640	369	320	369	640	1377	320	1377
Very Fine	2560	1377	1280	1377	2560	5313	1280	5313

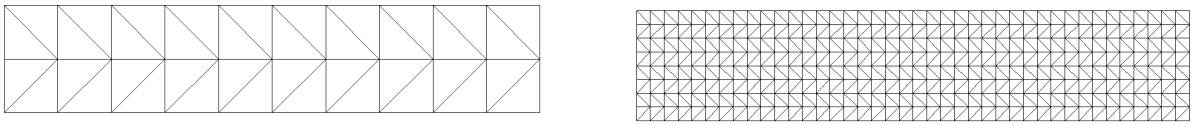

(a) (b)

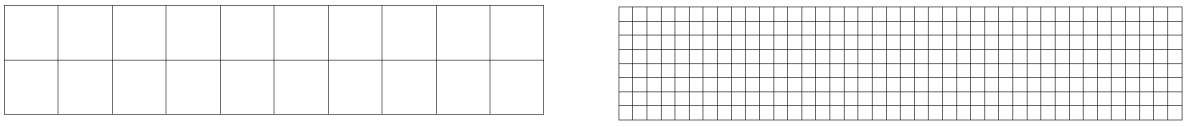

(c) (d)

Figure 8. Uniform mesh hierarchy: (a) 40 triangular element mesh; (b) 640 triangular element mesh; (c) 20 quadrilateral element mesh; and (d) 320 quadrilateral element mesh

To illustrate the convergence of the numerical method, we plot the normalized centerline tip displacement versus the characteristic mesh parameter *h* for each mesh in Figure 8. As can be seen, the predicted value of the tip displacement approaches the analytical value as the mesh is

refined. Additionally, the crudest approximation of the tip displacement is in error by only 3% for the Q4 elements and 35% for the T3 elements, which is much smaller than would be obtained by a standard finite element formulation applied near the incompressible limit. Therefore, we may conclude that the HVM formulation successfully addresses the problem of volumetric locking.

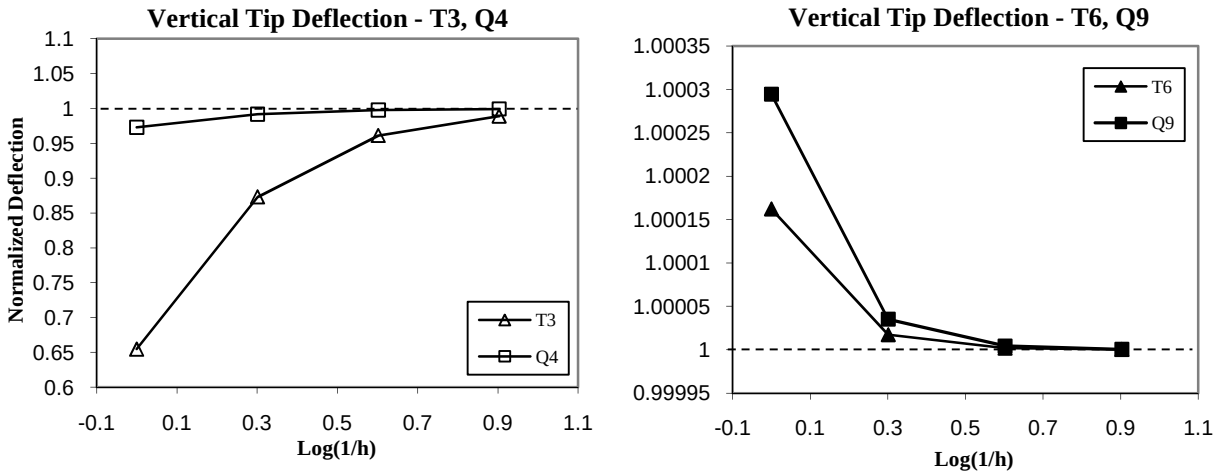

(a) (b)

Figure 9. Convergence of normalized tip displacement: (a) linear elements; (b) quadratic elements

Results of the numerical simulation performed on the medium Q4 mesh are presented in Figures 10-12. All three contour plots capture the smoothness of the exact solution. In particular, the pressure field does not exhibit spurious oscillations which can occur in simulations using unstable elements that do not satisfy the LBB stability condition. While the standard Q4 element with bilinear displacement and pressure interpolations is known to be unstable [36], Figure 12 provides evidence that the HVM formulation provides stability to this element and thereby eliminates these unphysical features.

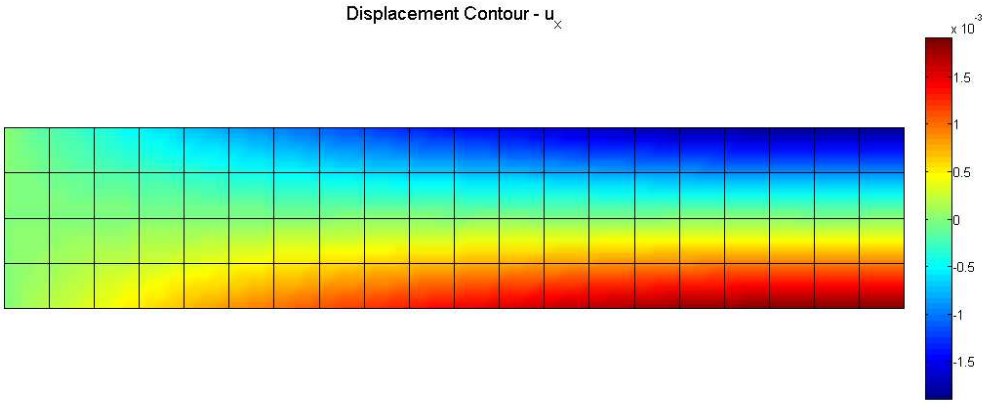

Figure 10. Displacement u_x contour, medium Q4 mesh

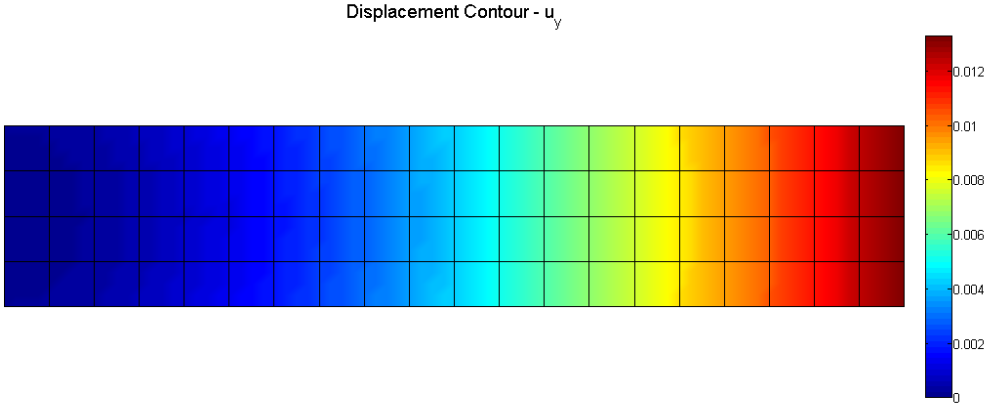

Figure 11 Displacement u_x contour, medium Q4 mesh

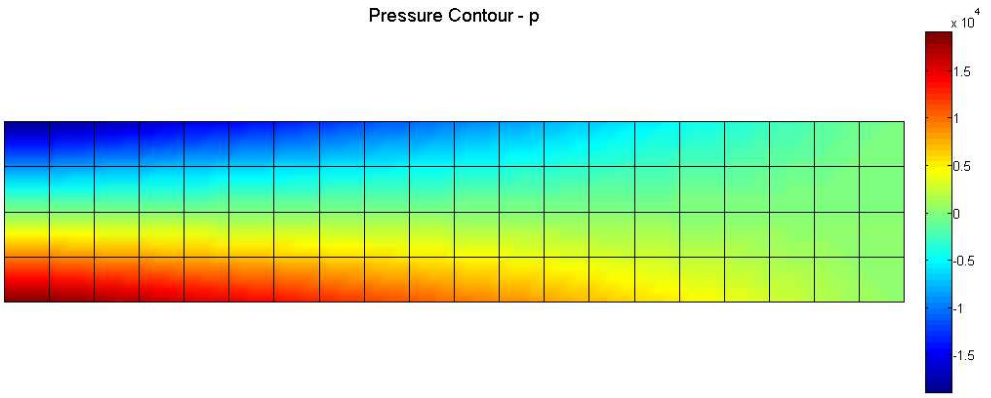

Figure 12. Pressure *p* contour, medium Q4 mesh

We now examine the error between our numerical simulations and the exact solution. We begin by evaluating the L_2 norm and H^1 seminorm of the standard error $\boldsymbol{e} = \boldsymbol{u} - \boldsymbol{u}^h$ over the entire domain as a global measure of accuracy of the numerical solutions. These quantities are evaluated using (5.3) and (5.4). Figure 13 presents the value of these error norms on a log-log scale for each element type computed on successively refined meshes as given in Table 2. The magnitudes have been normalized with respect to the exact solution fields in the corresponding norms. From finite element theory, the asymptotic rate of convergence for a primal field is $p+1$ in the L_2 norm, where p is the degree of the highest complete polynomial represented by the element basis functions [36]. The associated rate for the H^1 seminorm is p. Therefore, the optimal convergence rates for linear and quadratic elements in the L_2 norm are 2.0 and 3.0, respectively, and the associated rates for the H^1 seminorm are 1.0 and 2.0.

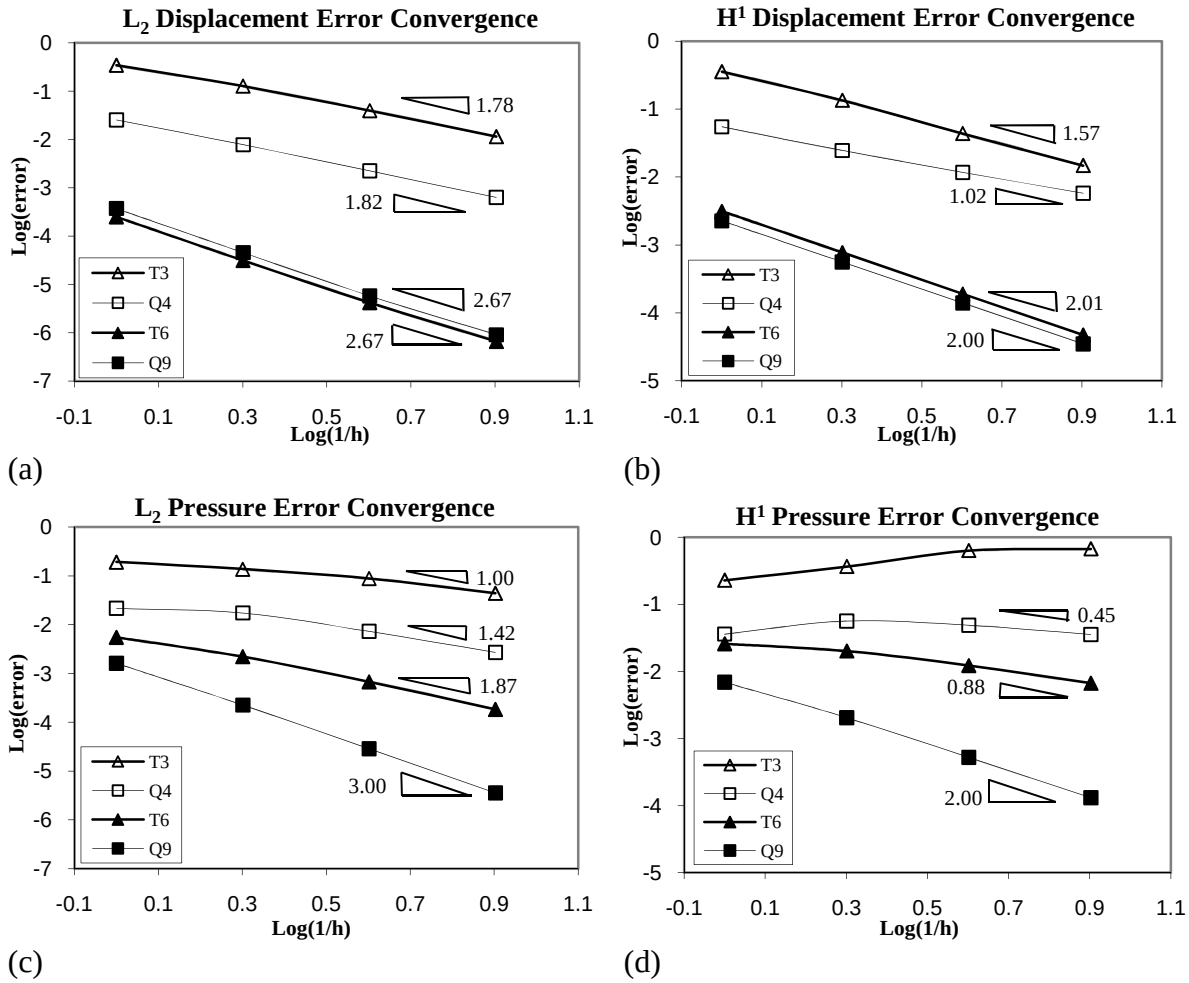

Figure 13. Convergence rates of normalized standard error: (a) L_2 norm of displacement; (b) H^1 seminorm of displacement; (c) L_2 norm of pressure; and (d) H^1 seminorm of pressure

For all element types, the displacement field converged at nearly the optimal rate in both the standard error measures. This agreement with the theoretical convergence rates indicates that the HVM formulation is stable. The stability of the pressure field is often more of a concern for mixed methods for linear elasticity. As can be seen in Figure 13 (c) and (d), the pressure fields do converge suboptimally for many of the element types. However, the trends are very smooth, and contour plots of the fields revealed that they do not exhibit spurious oscillations. Therefore, these results are considered to be positive.

6.3 Error Estimation: Uniform Meshes

As a first step in evaluating the performance of the proposed error estimators, we present convergence plots of the global norms of the fine scale field $\boldsymbol{u}'$ obtained from the explicit and implicit methods. These graphs are shown in Figure 14.

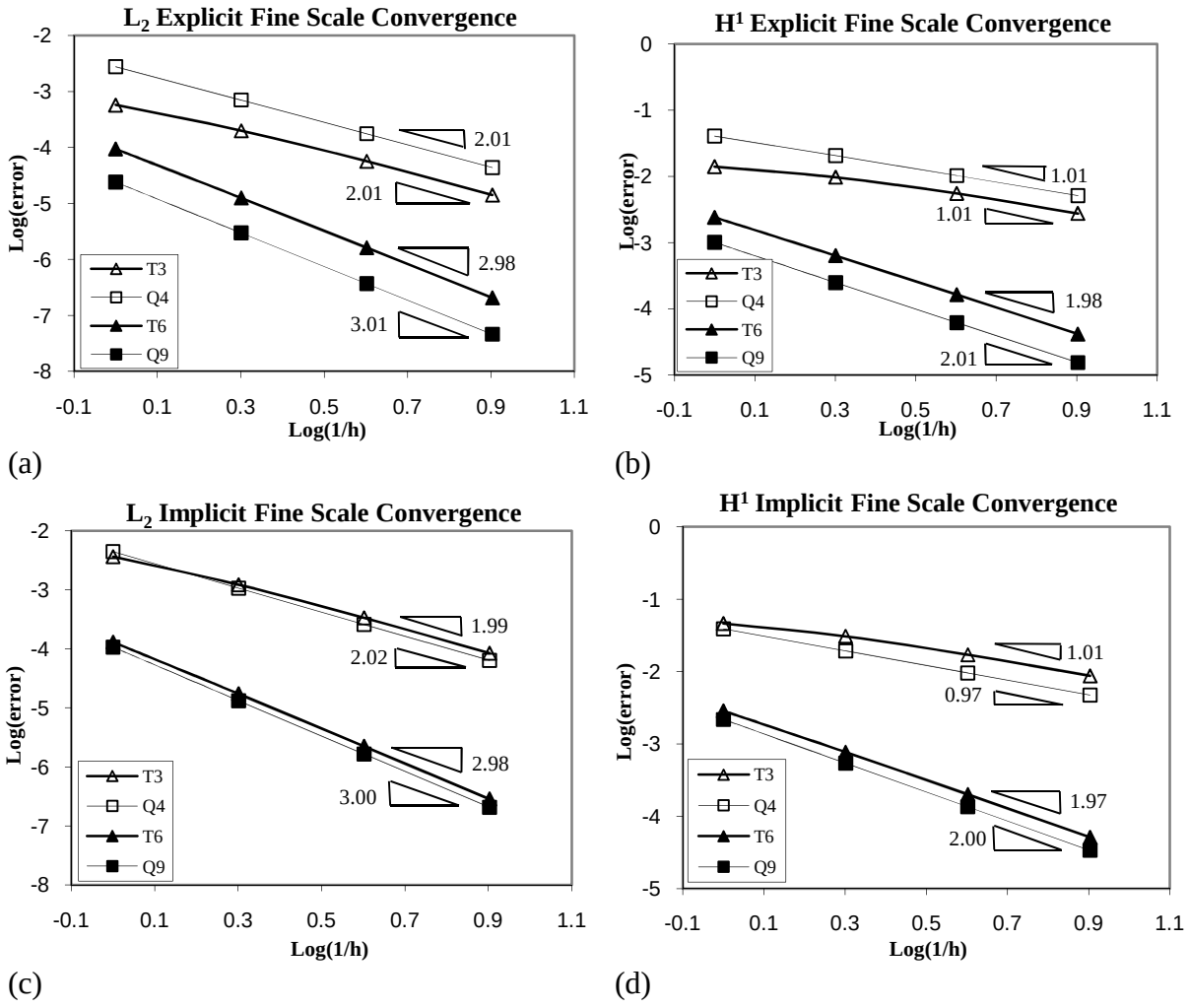

Figure 14. Convergence rates of normalized error estimates: (a) L_2 norm of explicit $\boldsymbol{u}'$; (b) H^1 seminorm of explicit $\boldsymbol{u}'$; (c) L_2 norm of implicit $\boldsymbol{u}'$; and (d) H^1 seminorm of implicit $\boldsymbol{u}'$

Upon examining the error estimates shown in Figure 14, we see that the fine scales from both the explicit and implicit methods are converging at the optimal rates. Since this convergence trend is parallel to the standard error, we may conclude that the fine scales can serve as an indicator of error reduction as the coarse mesh is refined. However, there is a significant shift in the magnitude of the norms. This is a result of our assumption that $\boldsymbol{u}'$ represents the relative component between $\bar{\boldsymbol{u}}$ and $\boldsymbol{u}$. Returning to the forms of $\boldsymbol{u}'$ given in (4.12) and (5.26), we see that in both cases the fine scales are zero at the coarse nodes; thus, these approximations of $\boldsymbol{u}'$ capture the fine part of the coarse scale residuals in the region between coarse nodes, both in Ω' and on Γ'. This approximation does imply that the fine scales should accurately capture the error in the H^1 seminorm, since the residuals of the governing equations involve derivatives of $\boldsymbol{u}$. In

fact, comparing Figure 13 (b) to Figure 14 (b) and (d) shows that this is indeed the case. Finally, we note that the implicit method typically provides a better approximation to both error norms than the explicit method, and both methods provide a consistent underestimation, or lower bound, on the error in the numerical solution. To clarify the proceeding points, we reproduce the values of the norms of the standard error and the error estimates in tabular form for the Q4 element in Table 3. From these values, we can clearly see that the implicit method produced closer estimates of the L_2 norm than the explicit method, but the explicit method provided slightly better estimates for the H^1 seminorm.

Table 3. List of error norms for Q4 elements

L_2 norms of error measures				
Number of Elements	Standard Error	Standard Error	Explicit Estimate	Implicit Estimate
	$\boldsymbol{u} - \boldsymbol{u}^h$	$p - p^h$	$\boldsymbol{u}'$	$\boldsymbol{u}'$
20	7.440 E-4	6.198 E+2	8.241 E-5	1.313 E-4
80	2.292 E-4	4.965 E+2	2.089 E-5	3.154 E-5
320	6.595 E-5	2.081 E+2	5.209 E-6	7.662 E-6
1280	1.870 E-5	7.745 E+1	1.298 E-6	1.883 E-6
H^1 norms of error measures				
Number of Elements	Standard Error	Standard Error	Explicit Estimate	Implicit Estimate
	$\boldsymbol{u} - \boldsymbol{u}^h$	$p - p^h$	$\boldsymbol{u}'$	$\boldsymbol{u}'$
20	4.965 E-4	1.797 E+3	3.688 E-4	3.526 E-4
80	2.218 E-4	2.810 E+3	1.869 E-4	1.748 E-4
320	1.060 E-4	2.428 E+3	9.319 E-5	8.629 E-5
1280	5.219 E-5	1.774 E+3	4.643 E-5	4.278 E-5

In addition to considering the performance of the error estimators in a normed sense, we may also investigate their performance at capturing the error locally throughout the domain. Figures 15-17 depict a projection of the standard error in each solution field onto the medium Q4 mesh. We can compare these results to the components of $\boldsymbol{u}'$ predicted by the explicit method, shown in Figures 18-19, and the implicit method, shown in Figures 20-21.

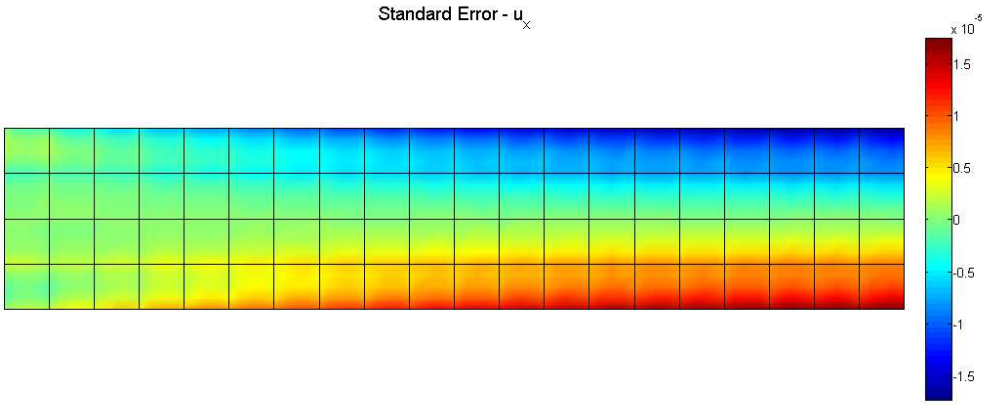

Figure 15. Standard displacement error e_x contour, medium Q4 mesh

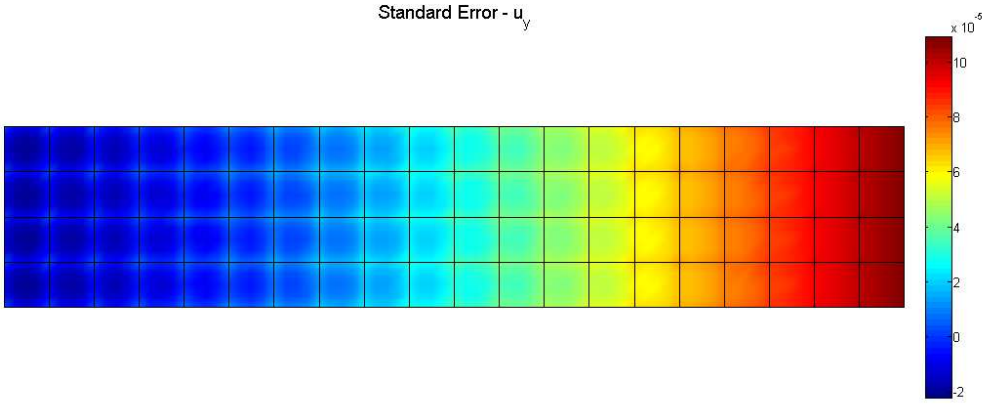

Figure 16. Standard displacement error e_y contour, medium Q4 mesh

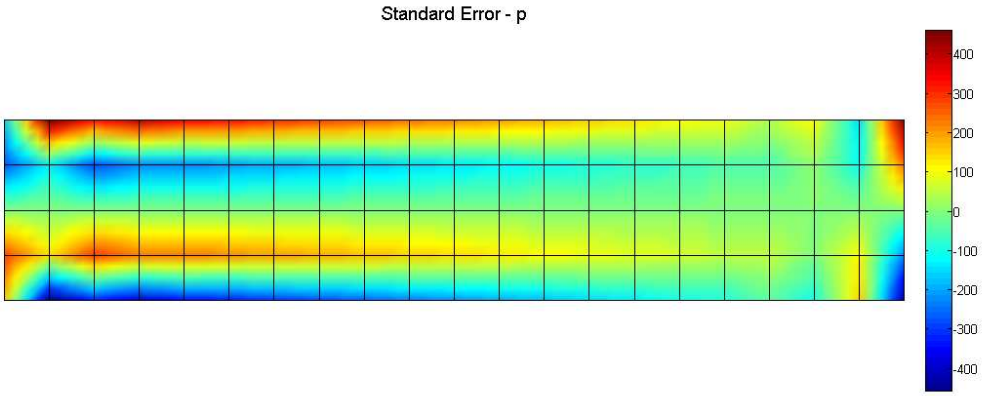

Figure 17. Standard pressure error e_p contour, medium Q4 mesh

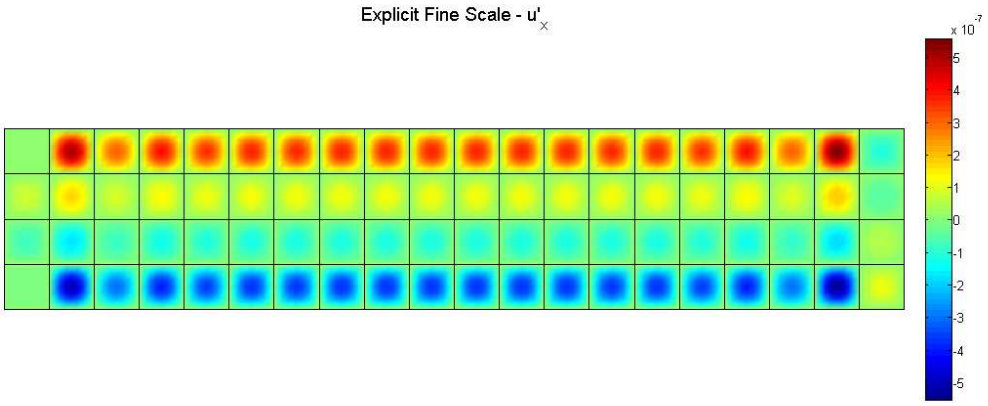

Figure 18. Explicit fine scale u_x' contour, medium Q4 mesh

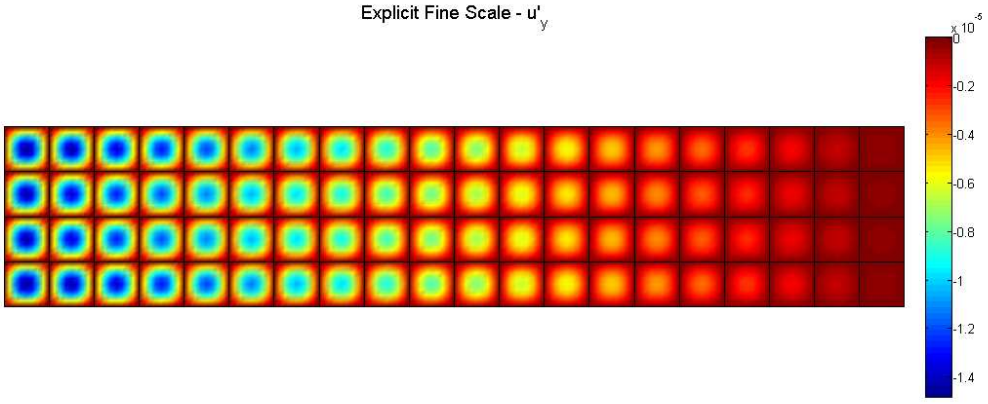

Figure 19. Explicit fine scale u_y' contour, medium Q4 mesh

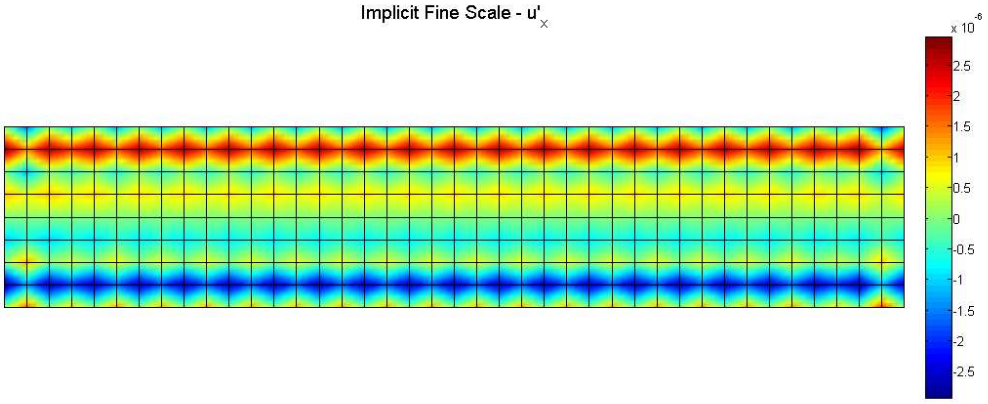

Figure 20. Implicit fine scale u_x' contour, medium Q4 mesh

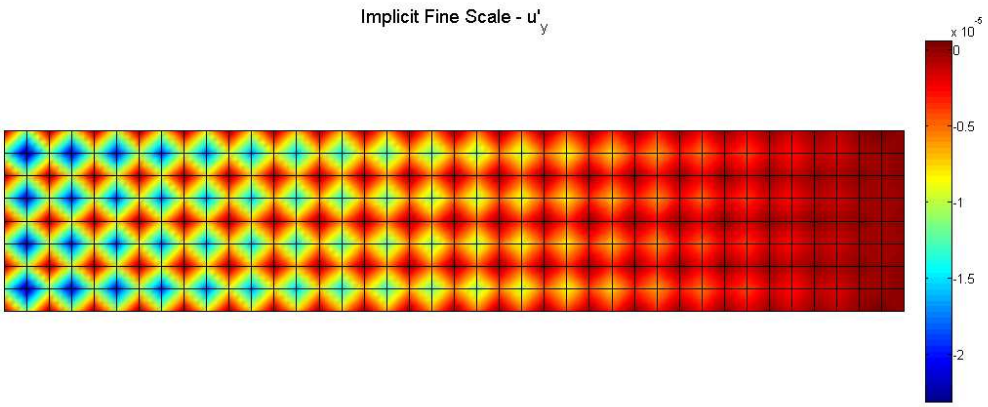

Figure 21. Implicit fine scale u_y' contour, medium Q4 mesh

A first glance at Figures 15 and 16 provides the observation that the coarse trends of the error in the displacement fields parallels the actual fields themselves: the error has higher magnitudes in regions where the solution fields have higher magnitudes. We also observe that the fine scale plots do not appear to match the standard error very well. However, by taking a closer look at Figures 15 and 16, we can observe finer features within the error fields. For example, compare the bottom left-hand corner element in Figures 16 and 21. Inside the element, the standard error value peaks at about 2.1 x 10^{-5}, and the fine scale error value is approximately 2.3 x 10^{-5} in the element center. Both of these values are fairly similar. In fact, if the coarse scale trends in the standard error are filtered out, the remaining fine scale error features match very well with the implicit fine scale field.

Additionally, we may observe that the elements with relatively larger fine scale components correspond with regions were the true solution field possesses higher displacement gradients. In Figure 20, the fine scales are concentrated on the upper and lower portions of the beam, where the bending stresses are highest. Also, in Figure 21, the fine scales increase from right to left, corresponding to the increase in shear stresses. Thus, these regions with significant fine scales represent candidate regions for local refinement in order to capture the gradients in the solution field more accurately.

Finally, while the explicit fine scales in Figures 18 and 19 provide a good qualitative match to the implicit fine scales in Figures 20 and 21, we note that the implicit fine scales appear to capture the magnitude of the fine scale effects in the standard error with higher accuracy.

The quality of the error estimators can also be evaluated through the use of the effectivity index discussed in Chapter 5. In Figure 22, we graph the value of I_{eff} for each element type, as computed by (5.8). There is a significant amount of variety across the element types. For the Q9 simulations, the index remains constant, while most of the other elements exhibit values tending toward unity upon refinement. This behavior can be linked to the size of disparity in convergence rates between the standard error and the error estimates. Comparing Figure 13 (b) to Figure 14 (b) and (d), we observe that the slopes of the curves for the Q9 elements are identical while the curves of other elements do not match exactly. A few trends are universal, however: except for the Q4 elements, the implicit estimate is closer to unity than the explicit estimate, and, except for the T6 elements, all error predictions underestimate the standard error. Finally, almost all values of the index are greater than 0.1, indicating that the estimates are on the same order of magnitude as the standard error.

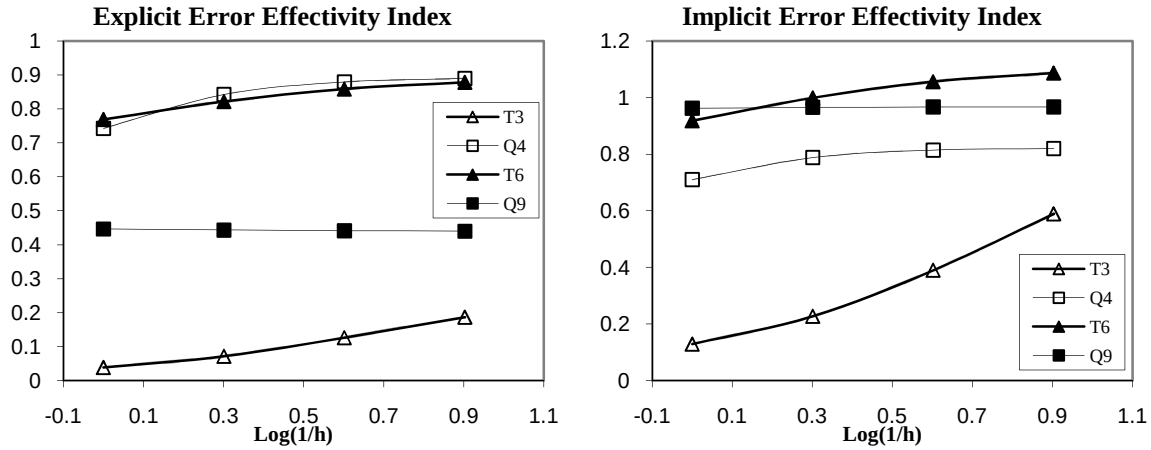

(a) (b)

Figure 22. Effectivity index for each element type in H^1 seminorm: (a) explicit error estimator; (b) implicit error estimator

The effectivity index can also be evaluated within each element using (5.7) to provide a local indication of the difference between the actual and predicted values of error. Figure 23 and Figure 24 show a contour plot of the value of I_{eff}^e on the medium Q4 mesh obtained from the explicit and implicit error estimators, respectively. Upon comparison with Figure 21, we observe that the value of I_{eff}^e is closest to unity for elements with large values of u_y' and smaller in elements with lower values. While the magnitude of $\|\boldsymbol{e}\|_{H^1(\Omega^e)}$ does decline from left to right across the domain for this simulation, the predicted values of error decline more rapidly, giving

rise to smaller values of I_{eff}^{e} . The tendency for the sharpness of an error estimate to deteriorate in regions where the actual error is reduced was also observed by [24]. By comparing Figures 23 and 24, we may conclude that the sharpness of the error estimate throughout the domain is maintained better by the implicit method than by the explicit method.

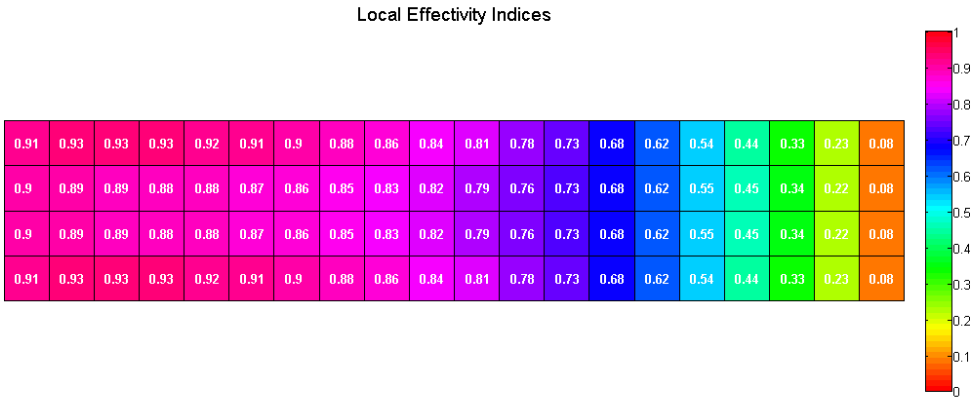

Figure 23. Local effectivity index for explicit fine scale

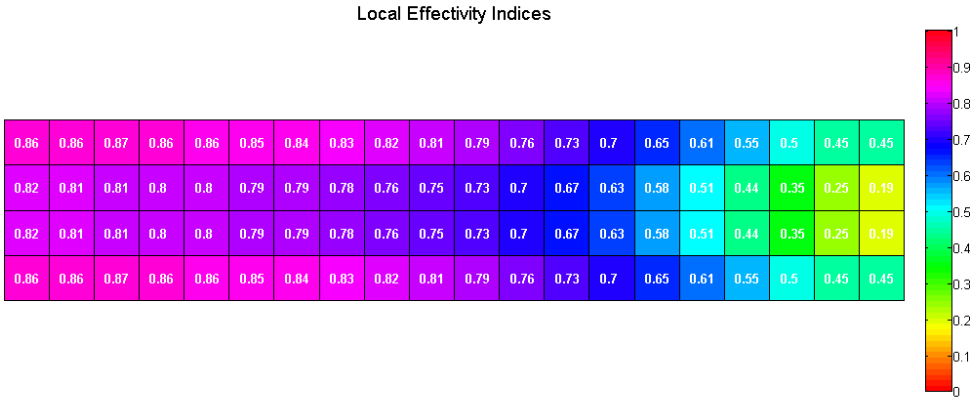

Figure 24. Local effectivity index for implicit fine scale

6.4 Error Estimator Variant Comparison

In this section, we investigate the performance of different versions of the implicit error estimator given by the localized fine scale equation. As discussed in section 5.3, two forms of the localized equation, the strong variant (5.26) and the weak variant (5.29), can be obtained from the fine scale equation $\mathcal{F}_r$ depending on whether integration by parts is invoked. Additionally,

the patches used in solving the decoupled equations can be set to various sizes by including elements further from a node using the recursive definition (5.17). Finally, the strategies of *h*-refinement or *p*-refinement could be used to provide different levels of resolution in the patches.

We conducted a study on the sequence of uniform Q4 meshes to compute the strong and weak variants and also to explore the effect of patch size on the global error estimate. The resulting L_2 norm and H^1 seminorm of the fine scale obtained from these simulations are shown in Table 4 and 5, respectively. The main conclusion is that both the strong and weak variants provide almost the same value for the norms, although the estimates from the strong variant were slightly closer to the standard error norms for this particular study. A patch size of 1, including only elements directly adjacent to a node, does not provide a sharp estimate for either of the error norms for either variant. However, a patch size of 2 is sufficient for approximating the value of the estimate obtained by solving the fine scale equation without localization. Also, the gain from increasing the patch size beyond 2 is not very significant. Therefore, a level 2 mesh star provides the optimal balance between computational efficiency and accuracy. Finally, we have numerically verified that the strong and weak variants are equivalent when solved over the entire domain.

Table 4. L_2 norm of error obtained for different patch sizes

Mesh Size	Standard Error	**Strong Variant**				
Number of Elements		Patch Size				Entire Domain
		1	2	3	4	
20	7.440 E-4	7.830 E-5	1.313 E-4	1.334 E-4	1.336 E-4	1.336 E-4
80	2.292 E-4	1.679 E-5	3.154 E-5	3.371 E-5	3.392 E-5	3.392 E-5
320	6.595 E-5	3.794 E-6	7.662 E-6	8.365 E-6	8.463 E-6	8.478 E-6
1280	1.870 E-5	8.914 E-7	1.883 E-6	2.079 E-6	2.110 E-6	2.115 E-6
Mesh Size	Standard Error	**Weak Variant**				
Number of Elements		Patch Size				Entire Domain
		1	2	3	4	
20	7.440 E-4	8.703 E-5	1.285 E-4	1.330 E-4	1.335 E-4	1.336 E-4
80	2.292 E-4	2.003 E-5	3.151 E-5	3.351 E-5	3.387 E-5	3.392 E-5
320	6.595 E-5	4.823 E-6	7.807 E-6	8.332 E-6	8.451 E-6	8.478 E-6
1280	1.870 E-5	1.212 E-6	1.960 E-6	2.075 E-6	2.107 E-6	2.115 E-6

Table 5. H^1 seminorm of error obtained for different patch sizes

Mesh Size	Standard Error	**Strong Variant**				
Number of Elements		Patch Size				Entire Domain
		1	2	3	4	
20	4.965 E-4	3.116 E-4	3.526 E-4	3.547 E-4	3.548 E-4	3.548 E-4
80	2.218 E-4	1.555 E-4	1.748 E-4	1.800 E-4	1.806 E-4	1.806 E-4
320	1.060 E-4	7.711 E-5	8.629 E-5	8.970 E-5	9.021 E-5	9.029 E-5
1280	5.219 E-5	3.831 E-5	4.278 E-5	4.467 E-5	4.499 E-5	4.505 E-5
Mesh Size	Standard Error	**Weak Variant**				
Number of Elements		Patch Size				Entire Domain
		1	2	3	4	
20	4.965 E-4	3.147 E-4	3.497 E-4	3.542 E-4	3.547 E-4	3.548 E-4
80	2.218 E-4	1.574 E-4	1.758 E-4	1.796 E-4	1.805 E-4	1.806 E-4
320	1.060 E-4	7.885 E-5	8.821 E-5	8.964 E-5	9.016 E-5	9.029 E-5
1280	5.219 E-5	4.011 E-5	4.470 E-5	4.472 E-5	4.497 E-5	4.505 E-5

A second study was conducted whereby the refinement of the submesh within each element was increased from 4 cells to 16 cells and the patch size was returned to the default of 2. The resulting L_2 norm and H^1 seminorm of the fine scale are shown in Table 6. While the accuracy of both variants increased with refinement, most notably in the H^1 seminorm, the execution time (not reported) also increased dramatically. Therefore, we conclude that the additional refinement of the fine scale trial space does not add sufficient value.

Table 6. Norms of error computed with finer submesh

Number of Elements	**Standard Error**		**Strong Variant**		**Weak Variant**	
	$L_2(\boldsymbol{e})$	$H^1(\boldsymbol{e})$	$L_2(\boldsymbol{u}')$	$H^1(\boldsymbol{u}')$	$L_2(\boldsymbol{u}')$	$H^1(\boldsymbol{u}')$
20	7.440 E-4	4.965 E-4	1.581 E-4	3.945 E-4	1.469 E-4	3.887 E-4
80	2.292 E-4	2.218 E-4	3.647 E-5	1.945 E-4	3.505 E-5	1.964 E-4
320	6.595 E-5	1.060 E-4	8.675 E-6	9.593 E-5	8.643 E-6	9.923 E-5
1280	1.870 E-5	5.219 E-5	2.108 E-6	4.754 E-5	2.190 E-6	5.084 E-5

6.5 Convergence Study: Distorted Meshes

The convergence of the stabilization framework was also investigated on meshes with significant element distortion. Such distortion may occur in practice when automatic mesh generators are

used to mesh complicated features in the geometry or at the junction between branching regions of the domain. We attempt to simulate these conditions by creating meshes containing elements of various sizes and shapes in close proximity. This study serves as an indicator of the robustness of the method. Table 7 contains data concerning the meshes used in the study; Figure 25 depicts two successive meshes for the triangular and quadrilateral elements. A very fine mesh for the Q9 elements was not simulated because the problem size exceeded the default limit of the program.

Table 7. Listing of number of elements and nodes in mesh hierarchy

Mesh Name	Triangular (T3)		Quadrilateral (Q4)		Triangular (T6)		Quadrilateral (Q9)	
	Elements	Nodes	Elements	Nodes	Elements	Nodes	Elements	Nodes
Coarse	80	53	118	146	80	185	118	527
Medium	320	185	472	527	320	689	472	1997
Fine	1280	689	1888	1997	1280	2657	1888	7769
Very Fine	5120	2657	7552	7769	5120	10433	7552	30641

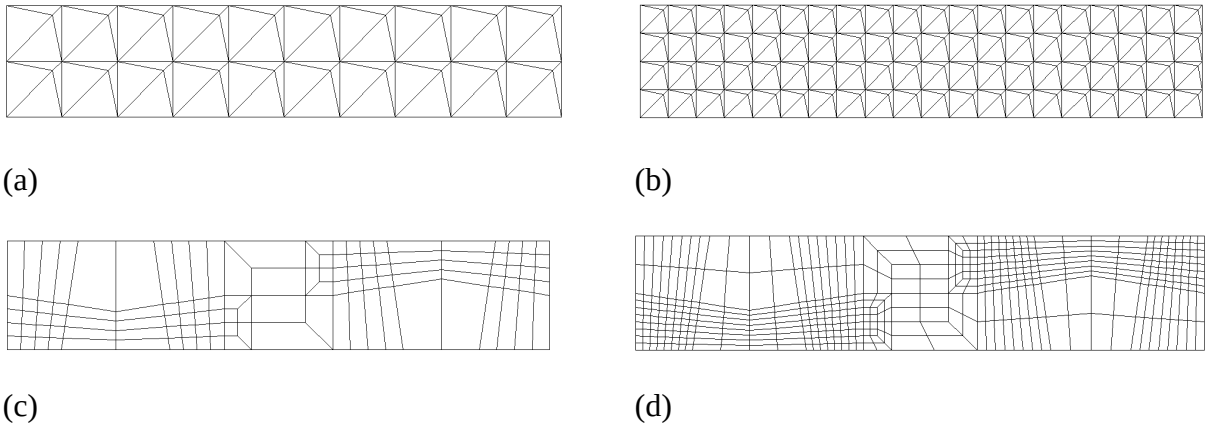

(a) (b)

(c) (d)

Figure 25. Distorted mesh hierarchy: (a) 80 triangular element mesh; (b) 1280 triangular element mesh; (c) 118 quadrilateral element mesh; and (d) 1997 quadrilateral element mesh

Results of the numerical simulation performed on the medium Q4 mesh are presented in Figures 26-28. While the displacement contours retain the symmetry of the exact solution, the pressure field became slightly unsymmetrical as a result of the severe distortion. However, the major trends of the solution are still captured.

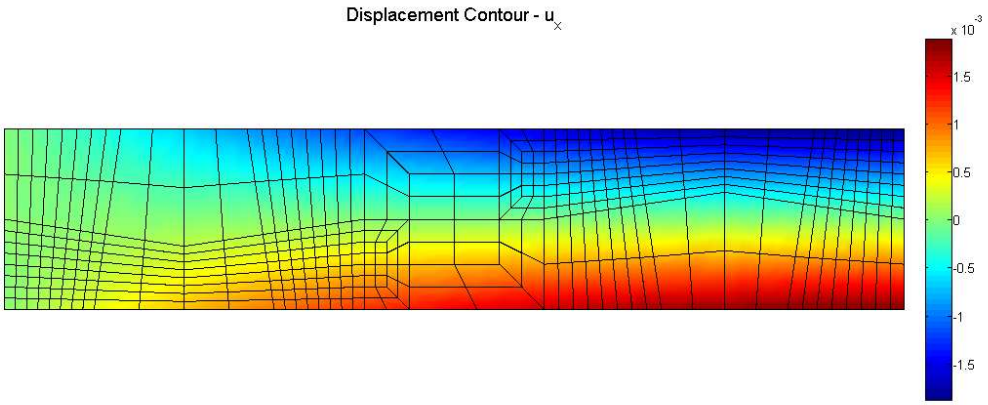

Figure 26. Displacement u_x contour, medium Q4 mesh

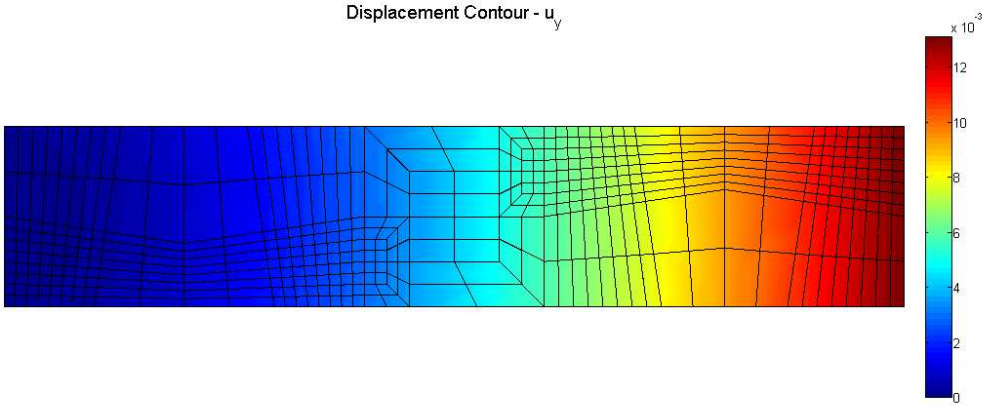

Figure 27. Displacement u_y contour, medium Q4 mesh

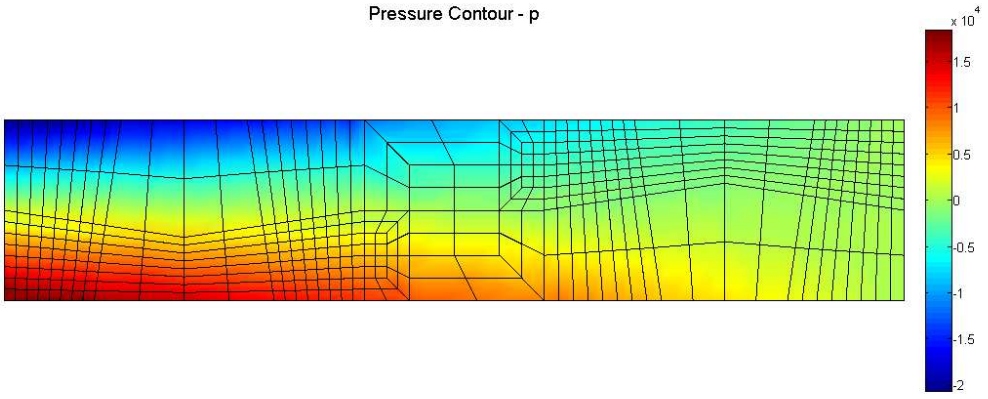

Figure 28. Pressure *p* contour, medium Q4 mesh

The convergence of the standard error norms is shown in Figure 29. The convergence rates of the displacement field are nearly optimal for all element types in both norms; however, the magnitude of the error in the solutions increased slightly from the solutions obtained on uniform meshes, which can be observed from the downward shift of the curves in Figure 29 compared to those in Figure 13. The pressure field experienced deteriorated rates compared to the uniform mesh study. In all cases, the rate for the L_2 norm was one order below the optimum. For the H^1 seminorm, the rates for the T6 and Q9 elements were one order below the optimum, the Q4 elements failed to converge, and the T3 elements exhibited a relative error greater than 1.0. This poor performance can be attributed to the effect of mesh distortion on the quality of the numerical approximation. Additionally, the norms for the first Q4 mesh appear out of sync with the subsequent simulations do to the lack of resolution on the coarsest mesh.

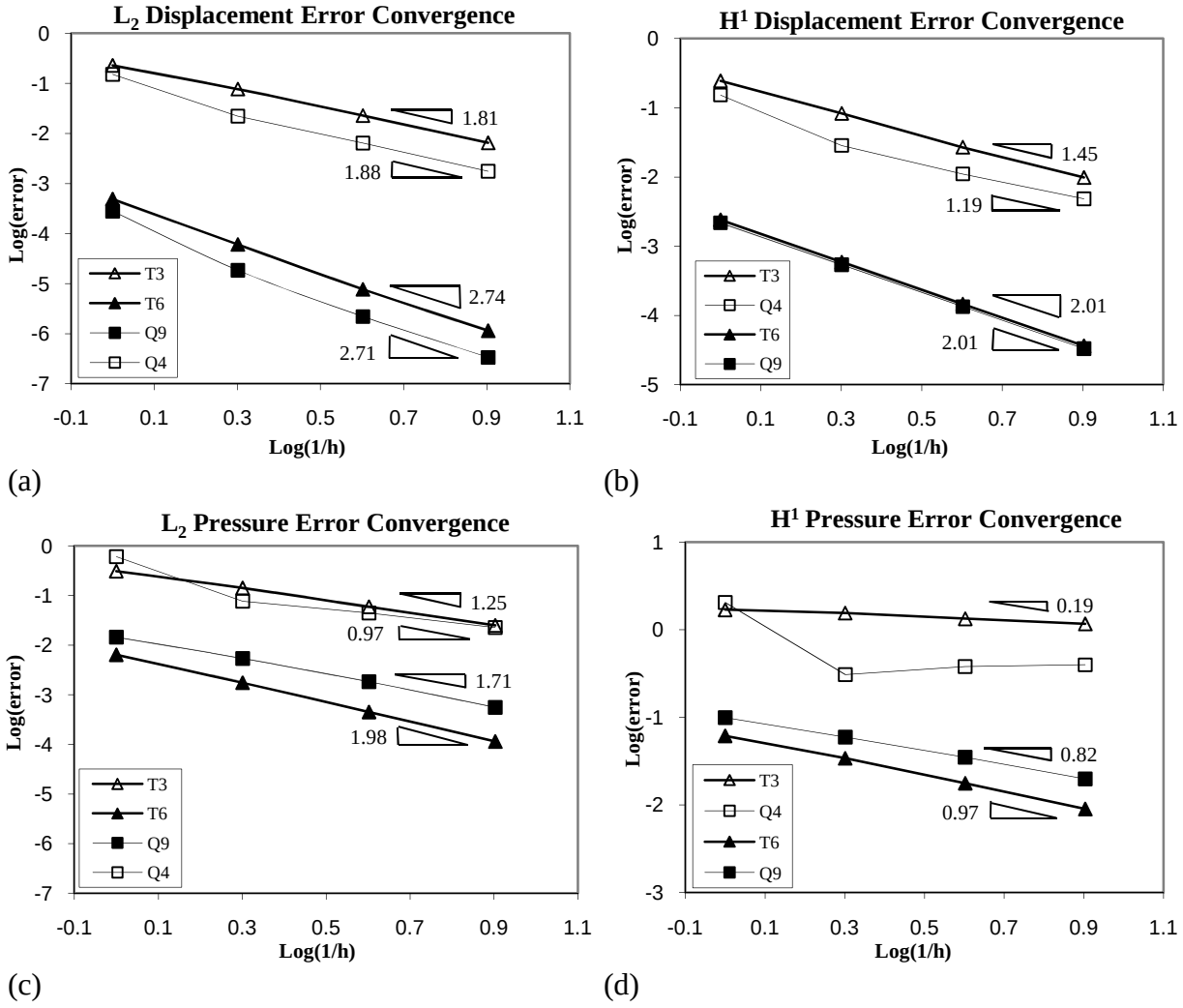

Figure 29. Convergence rates of normalized standard error: (a) L_2 norm of displacement; (b) L_2 norm of pressure; (c) H^1 seminorm of displacement; and (d) H^1 seminorm of pressure

6.6 Error Estimation: Distorted Meshes

This section presents convergence plots of the global norms of the fine scale field $\boldsymbol{u}'$ obtained from the explicit and implicit methods. As can be seen in Figure 30, both the explicit and implicit L_2 error norms converge at the optimal rates of 2.0 for linear elements and 3.0 for quadratic elements. Similarly, the H^1 seminorm converges near the optimal rate for each of the element types. By comparing the error estimates with the standard error in Figure 29 (a) and (b), we observe that the convergence rates of the error estimates parallel those of the standard error. Additionally, the estimated H^1 seminorm in Figure 30 (b) and (d) match closely with the curves in Figure 29. These trends were preserved under significant distortion of the mesh.

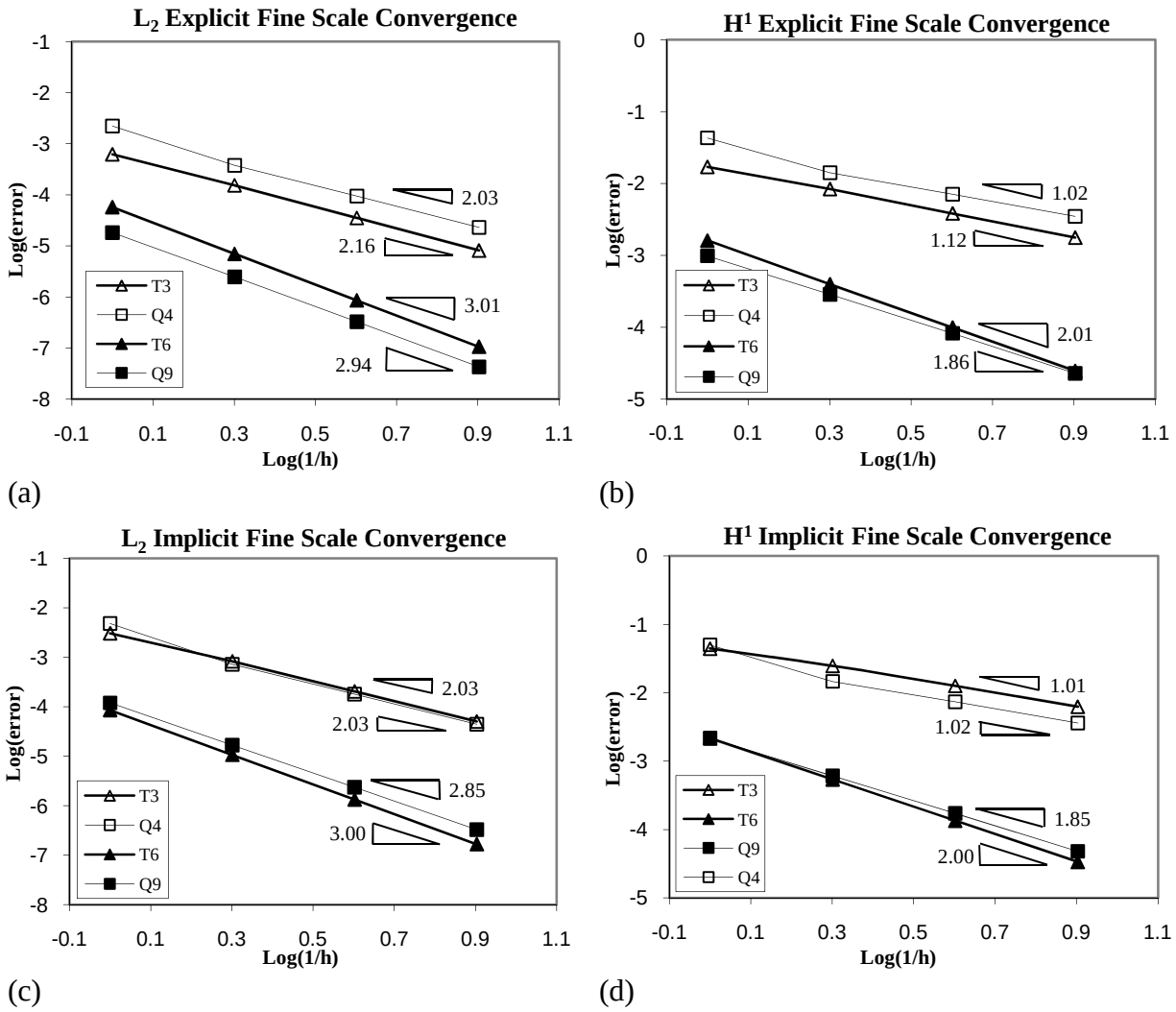

Figure 30. Convergence rates of normalized error estimates: (a) L_2 norm of explicit $\boldsymbol{u}'$; (b) H^1 seminorm of explicit $\boldsymbol{u}'$; (c) L_2 norm of implicit $\boldsymbol{u}'$; and (d) H^1 seminorm of implicit $\boldsymbol{u}'$

6.7 Simply-Supported Beam Problem Description

The second simulation is of a simply-supported beam loaded by its self weight. This problem was selected in order to verify the consistency of the stabilized formulation in the presence of a non-zero body force. Plane strain conditions are assumed, and tractions derived from the exact solution are applied to the left and right edges of the beam. The description of the problem is shown in Figure 31; the exact solution derived from elasticity theory is given in (6.6)-(6.8) [43].

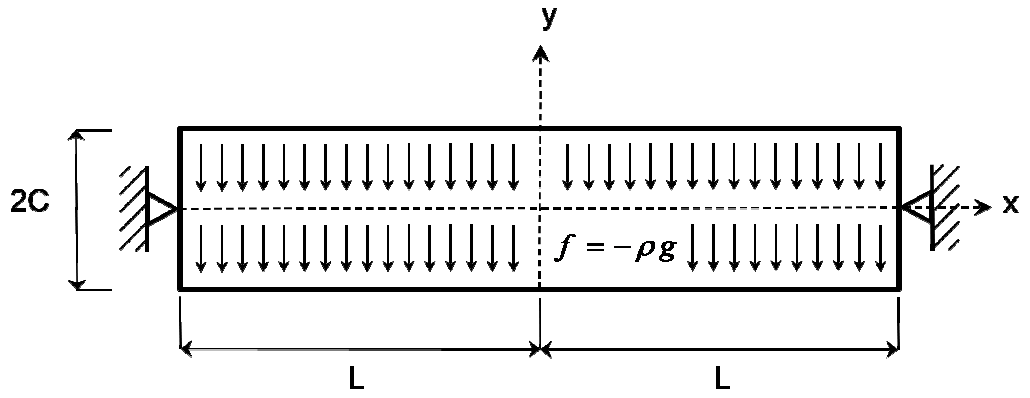

Figure 31. Simply-supported beam problem description

$$u_x^{\text{exact}} = \frac{\rho g C\left(1-\nu^2\right)xy}{EI}\left[\left(\frac{x^2}{3}-L^2\right)+\left(\frac{2}{5}+\frac{\nu}{3(1-\nu)}\right)C^2-\left(\frac{2}{3}+\frac{\nu}{3(1-\nu)}\right)y^2\right] \tag{6.6}$$

$$u_y^{\text{exact}} = \frac{\rho g C\left(1-\nu^2\right)}{EI}\left[\left(\frac{1}{12}+\frac{\nu}{6(1-\nu)}\right)y^4-\left(\frac{1}{6}+\frac{\nu}{5(1-\nu)}\right)C^2y^2+\left(L^2-x^2\right)\frac{\nu y^2}{2(1-\nu)}\right.$$
$$\left.-\frac{1}{12}\left(x^2-5L^2\right)\left(x^2-L^2\right)+\left(\frac{4}{5}+\frac{5}{6}\frac{\nu}{1-\nu}\right)\left(x^2-L^2\right)C^2\right] \tag{6.7}$$

$$p^{\text{exact}} = -\frac{\rho g C\nu y}{I}\left[\left(x^2-L^2\right)+\frac{C^2}{15}-\frac{y^2}{3}\right] \tag{6.8}$$

$$I = \frac{(2C)^3}{12} \tag{6.9}$$

The values of parameters selected for the simulation were:

$$\rho = 1000 \quad g = 9.81 \quad C = 1 \quad L = 10 \quad E = 7.5\times10^7 \quad \nu = 0.4999 \tag{6.10}$$

6.8 Convergence Study: Uniform Meshes

In order to verify the convergence of the method with respect to this particular problem, the numerical solution was computed on sets of uniformly refined meshes. Due to the overlap of the domains between the cantilever beam and the simply-supported beam, the meshes presented in Table 2 were also used for this study. The resulting values of the normalized vertical deflection at the origin of coordinates, namely the midpoint of the beam, are plotted in Figure 32. As can be seen, the predicted value of the tip displacement approaches the analytical value as the mesh is

refined. These results exhibit similar performance compared to the values obtained for the cantilever beam.

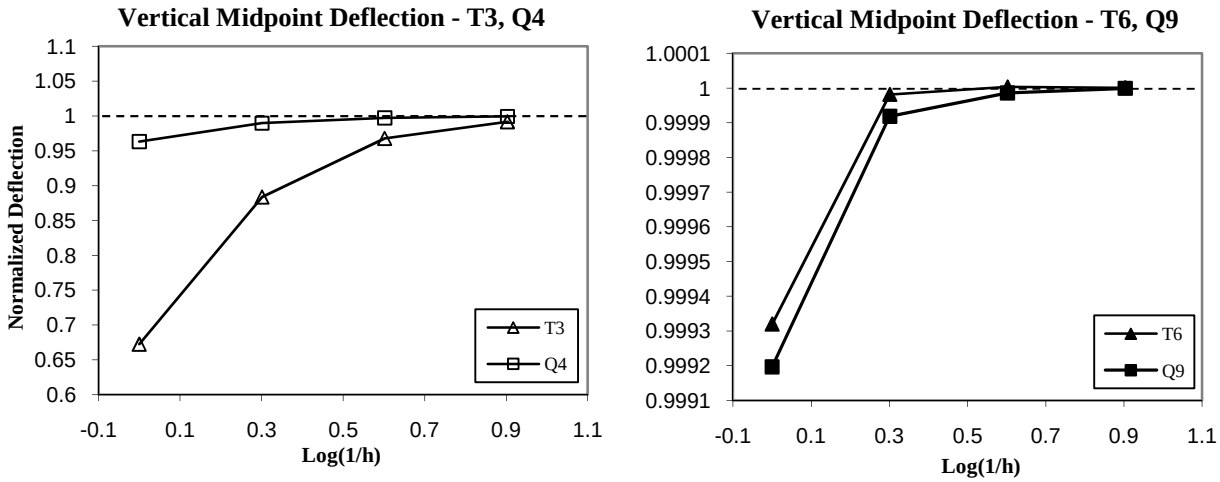

(a) (b)

Figure 32. Convergence of normalized midpoint displacement: (a) linear elements; (b) quadratic elements

Results of the numerical simulation performed on the medium Q4 mesh are presented in Figures 33-35. All three contour plots capture the smoothness of the exact solution; the pressure field is free from spurious oscillations. The symmetries and anti-symmetries of the exact solution are captured by the uniform quadrilateral meshes.

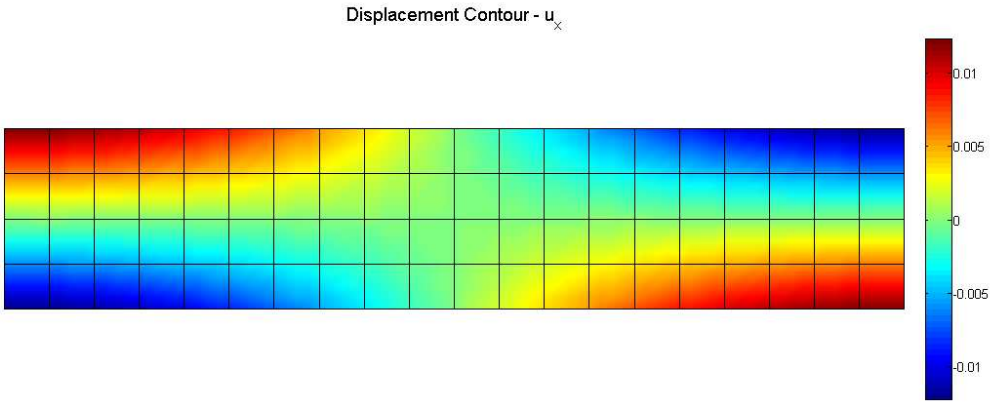

Figure 33. Displacement u_x contour, medium Q4 mesh

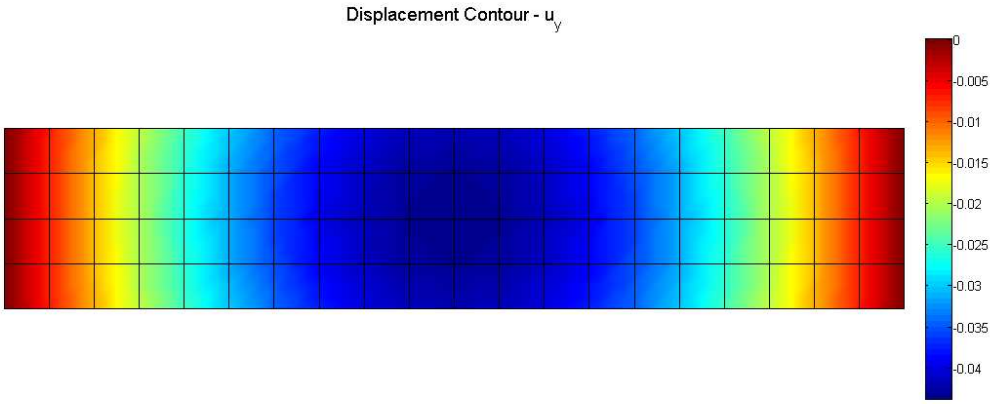

Figure 34. Displacement u_y contour, medium Q4 mesh

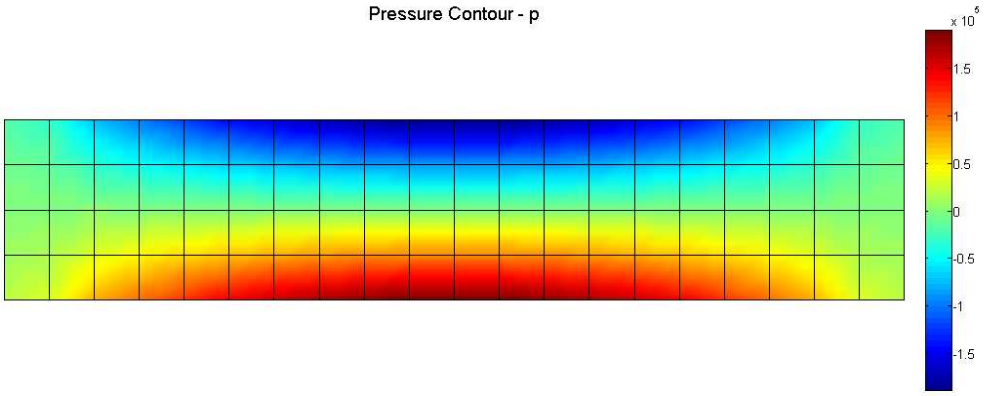

Figure 35. Pressure p contour, medium Q4 mesh

The convergence rates for the normalized standard error in the displacement and pressure fields measured in the L_2 norm and H^1 seminorm are presented in Figure 36. All element types exhibit near optimal convergence for the displacement field in both norms. The error in the pressure field converged at one order below the corresponding optimal rate for most of the element types. Additionally, the H^1 seminorm of pressure diverged for the T3 element as it did for the first problem. By comparing Figure 36 to Figure 13, we observe that the numerical solutions for the simply-supported beam as a whole contained more error than those obtained for the cantilever beam. We attribute this increase in error to the fact that the exact solution of the second problem is a fourth-order polynomial while the first problem is a cubic polynomial.

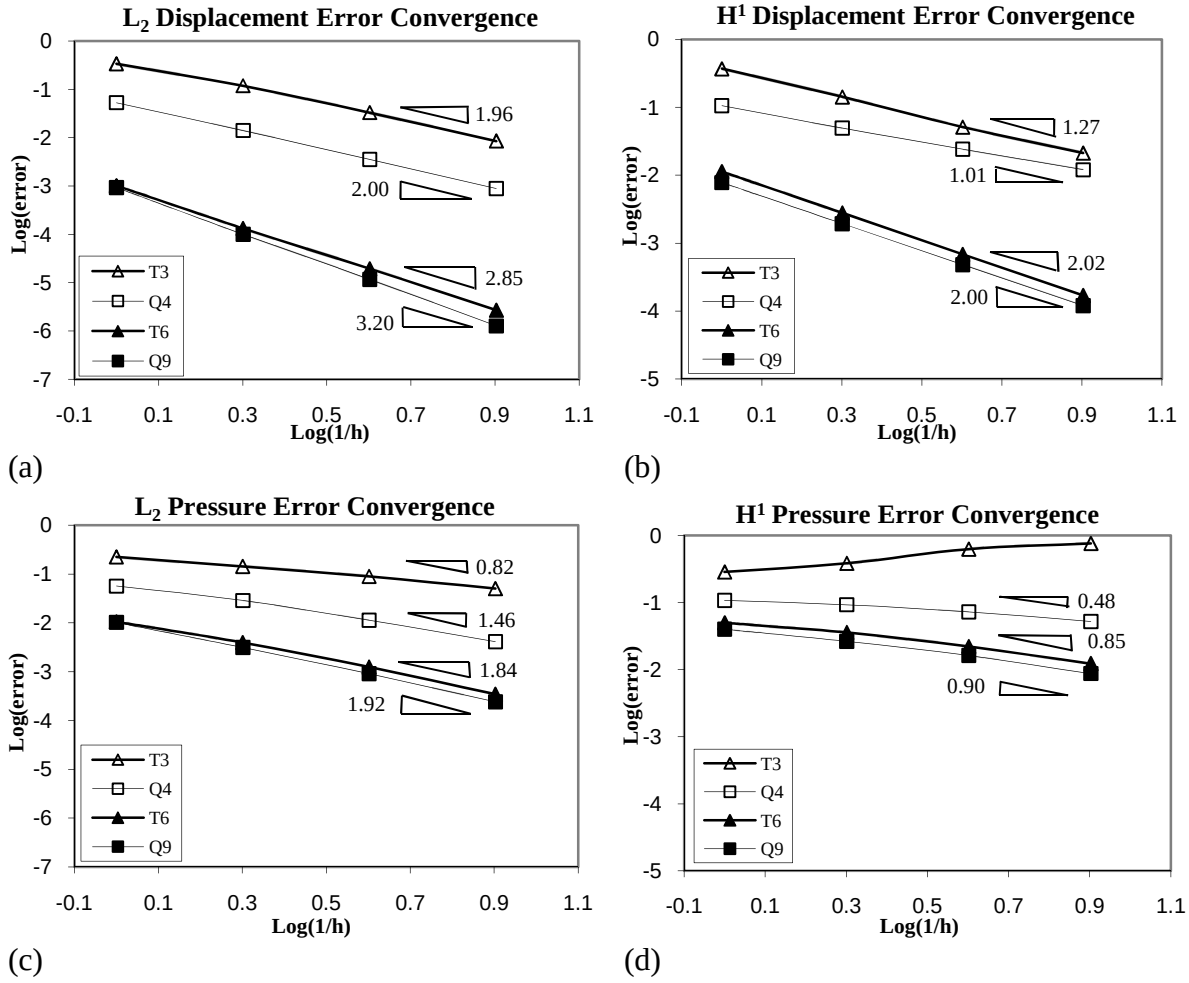

Figure 36. Convergence rates of normalized standard error: (a) L_2 norm of displacement; (b) L_2 norm of pressure; (c) H^1 seminorm of displacement; and (d) H^1 seminorm of pressure

6.9 Error Estimation: Uniform Meshes

Analogous to the cantilever beam study, we evaluate the fine scale field $\boldsymbol{u}'$ for each of the numerical simulations using explicit and implicit methods and compute the resulting global norms, which are presented in Figure 37. Many of the trends highlighted for the first problem also apply to the current study. In particular, all of the curves obtained using both error estimation methods possess optimal convergence, and each individual curve runs parallel to its counterpart in Figure 36. Also, the H^1 seminorm of the estimated error provides a sharp estimate of the standard error in displacement.

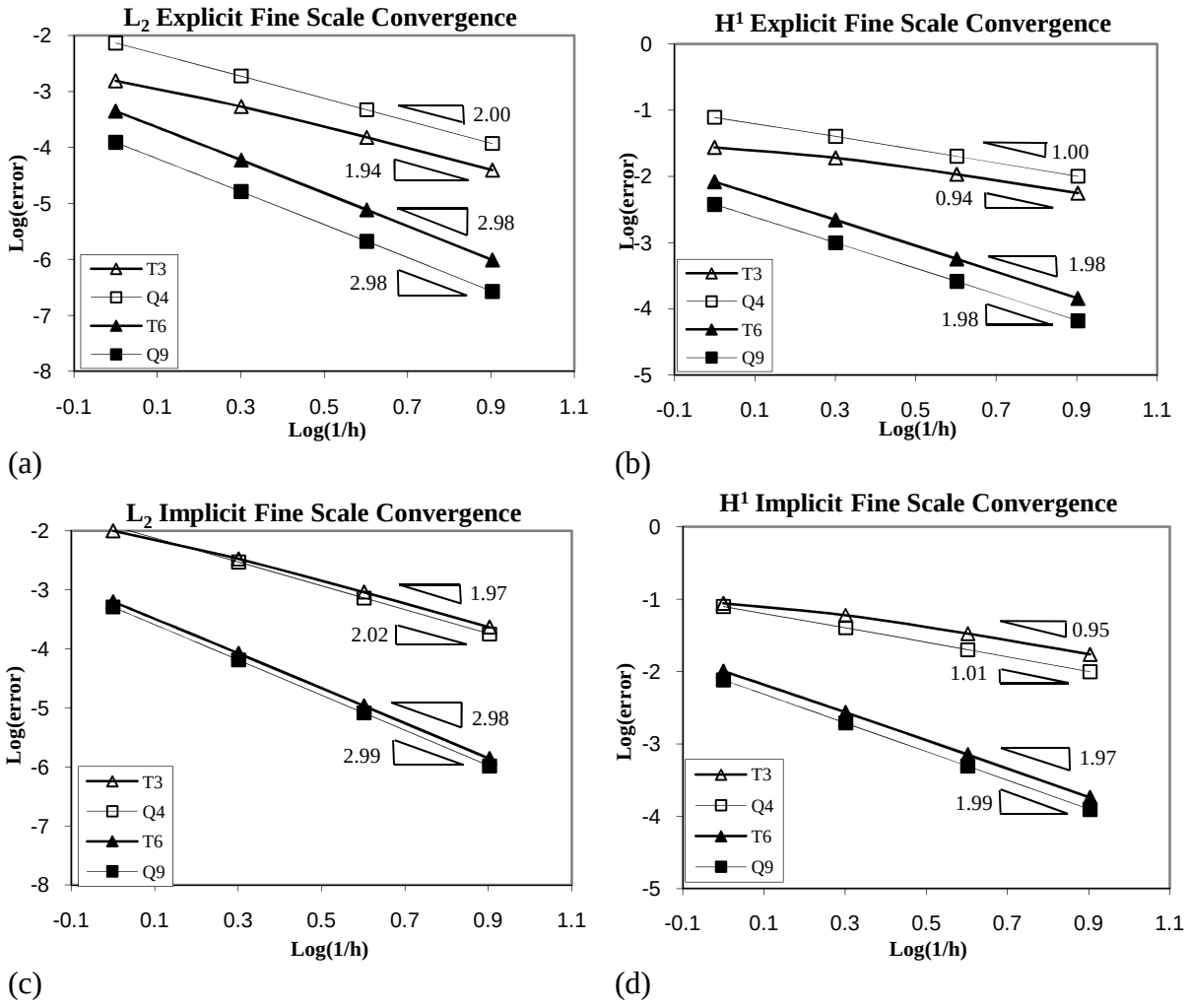

Figure 37. Convergence rates of normalized error estimates: (a) L_2 norm of explicit $\boldsymbol{u}'$; (b) H^1 seminorm of explicit $\boldsymbol{u}'$; (c) L_2 norm of implicit $\boldsymbol{u}'$; and (d) H^1 seminorm of implicit $\boldsymbol{u}'$

Next, we examine the distribution of error across the domain by presenting contour plots of the various field components. Figures 38-40 depict a projection of the standard error in each solution field onto the medium Q4 mesh. We can compare these results to the components of $\boldsymbol{u}'$ predicted by the explicit method, shown in Figures 41-42, and the implicit method, shown in Figures 43-44.

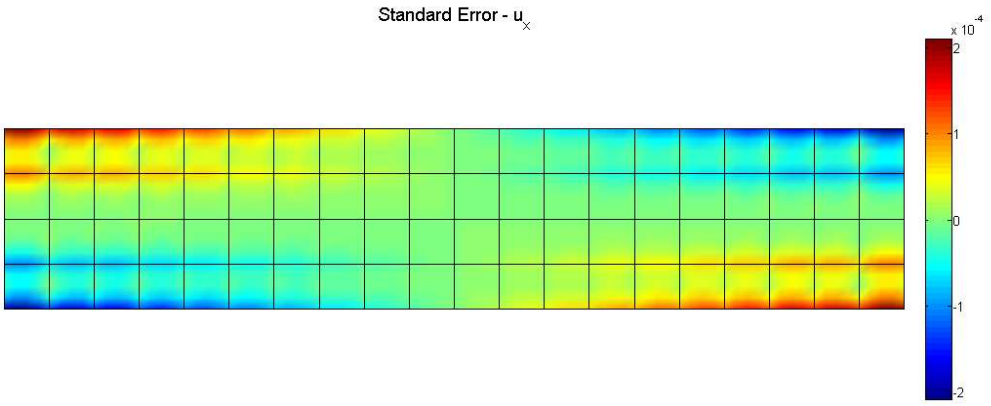

Figure 38. Standard displacement error e_x contour, medium Q4 mesh

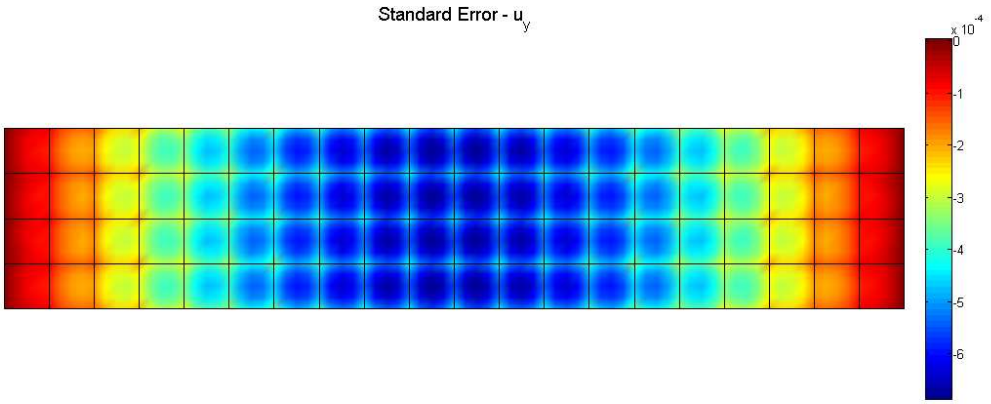

Figure 39. Standard displacement error e_y contour, medium Q4 mesh

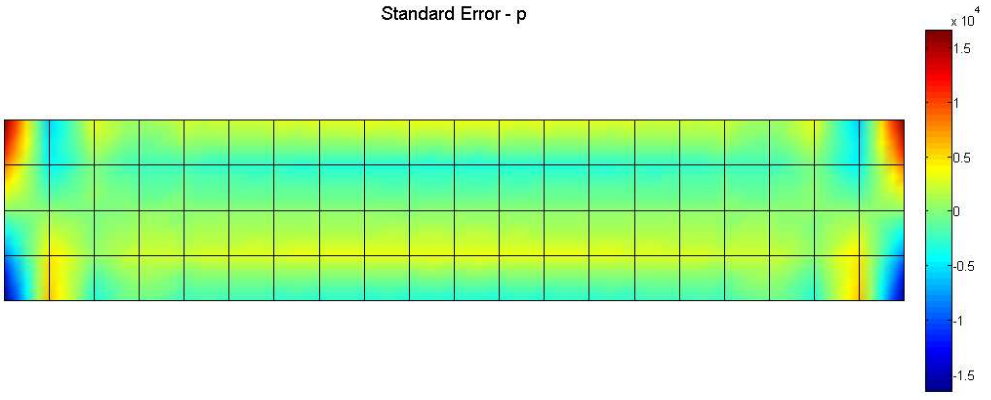

Figure 40. Standard pressure error e_p contour, medium Q4 mesh

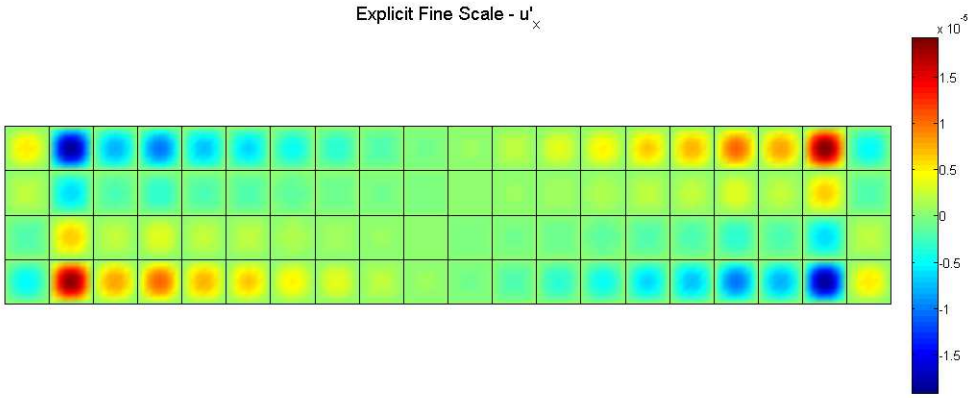

Figure 41. Explicit fine scale u_x' contour, medium Q4 mesh

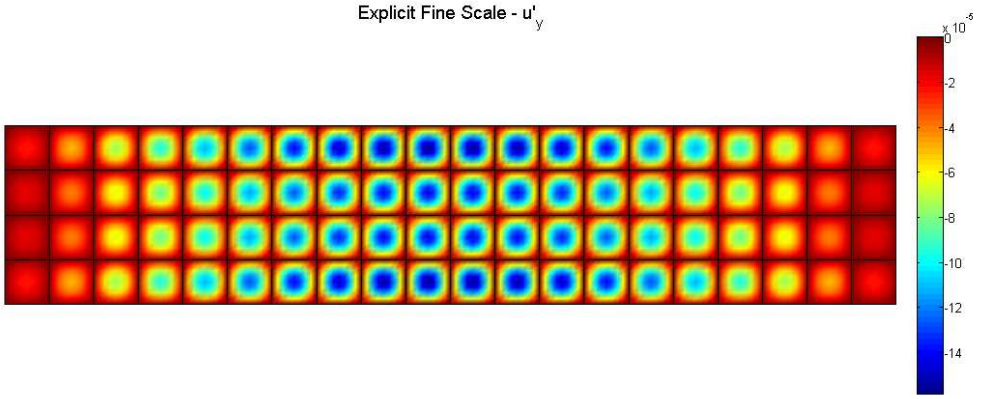

Figure 42. Explicit fine scale u_y' contour, medium Q4 mesh

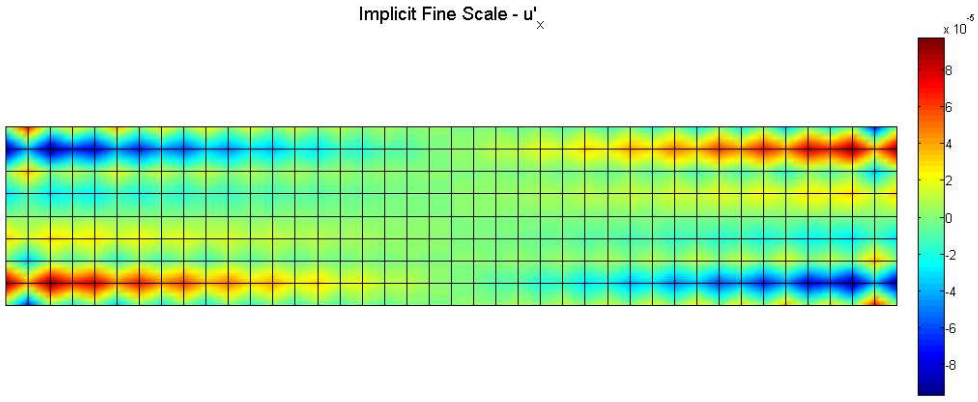

Figure 43. Implicit fine scale u_x' contour, medium Q4 mesh

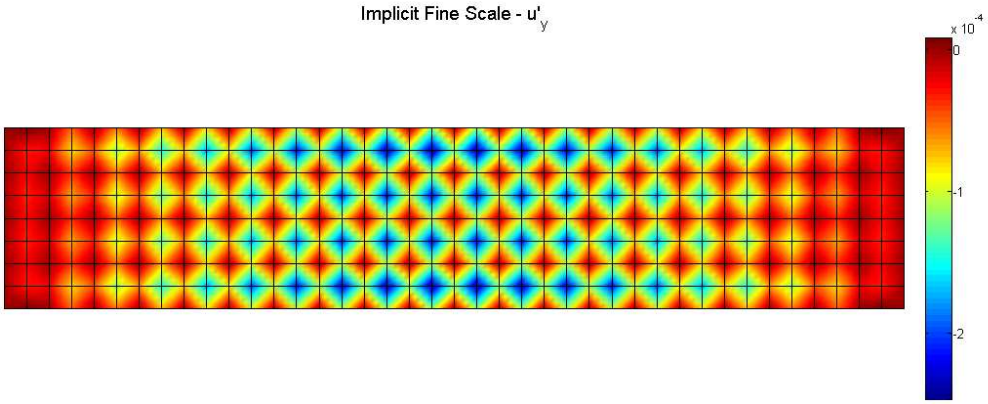

Figure 44. Implicit fine scale u_y' contour, medium Q4 mesh

By comparing Figure 38 to Figure 33, we again observe that magnitude of error is larger in regions where the solution field has higher magnitudes. Also, the fine scale features in the error distributions are more apparent for this problem compared to the first. These same features are approximated well by the fine scale error estimates. For example, consider one of the elements at mid-span on the bottom chord of the beam in Figure 39. The value of the error within the element peaks at 6.8 x 10^{-4}, but the values at the corners of the element are about 4.8 x 10^{-4}. The difference between these values is 2.0 x 10^{-4}, which is similar to the magnitude of 2.4 x 10^{-4} within the same element in Figure 44. This trend was discussed previously for the cantilever beam.

The performance of the error estimators is now quantified using the effectivity index, which is shown in Figure 45 for the explicit and implicit methods. These results are remarkably similar to those presented in Figure 22 for the cantilever beam problem. Therefore, the same comments about the proper magnitude of the error and the lower bound property still apply. Although the results from only two problems give little indication of the performance of the method for arbitrary problems, this consistent behavior is a positive result.

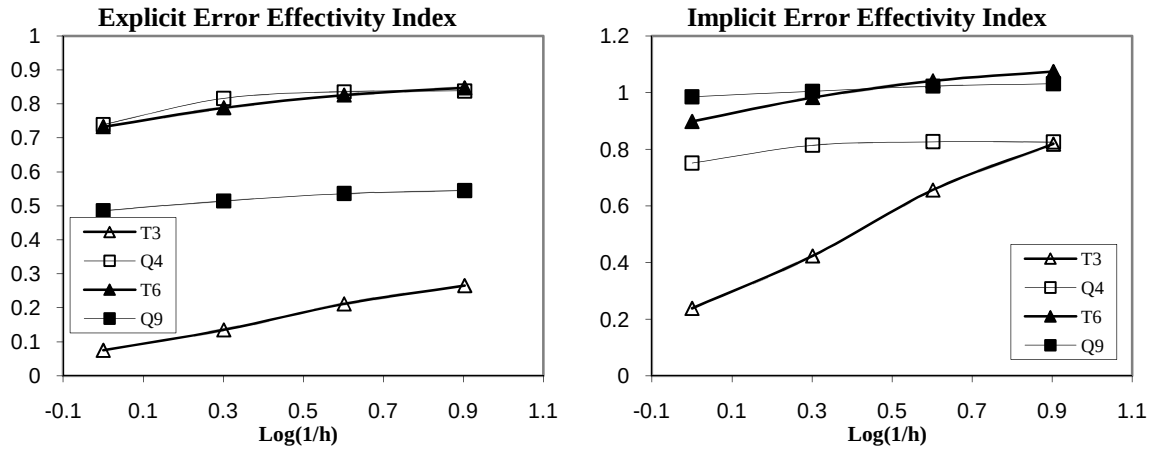

Figure 45. Effectivity index for each element type in H^1 seminorm: (a) explicit error estimator; (b) implicit error estimator

Finally, we evaluate the effectivity index locally in each element to indicate the difference between the actual and predicted values of error. Figure 46 and Figure 47 show a contour plot of the value of I^e_{eff} on the medium Q4 mesh obtained from the explicit and implicit error estimators, respectively. By looking back to Figure 44, we conclude that the value of I^e_{eff} is closest to unity for elements with large values of u'_y and smaller in elements with lower values. This behavior was also discussed in the context of the first problem in section 6.3. The distribution of I^e_{eff} shown in Figures 46 and 47 again implies that the sharpness of the error estimate throughout the domain is maintained better by the implicit method than by the explicit method.

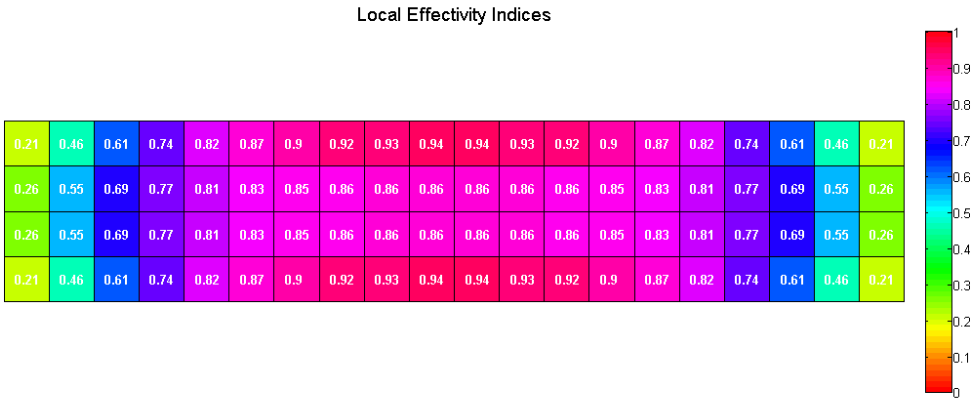

Figure 46. Local effectivity index for explicit fine scale

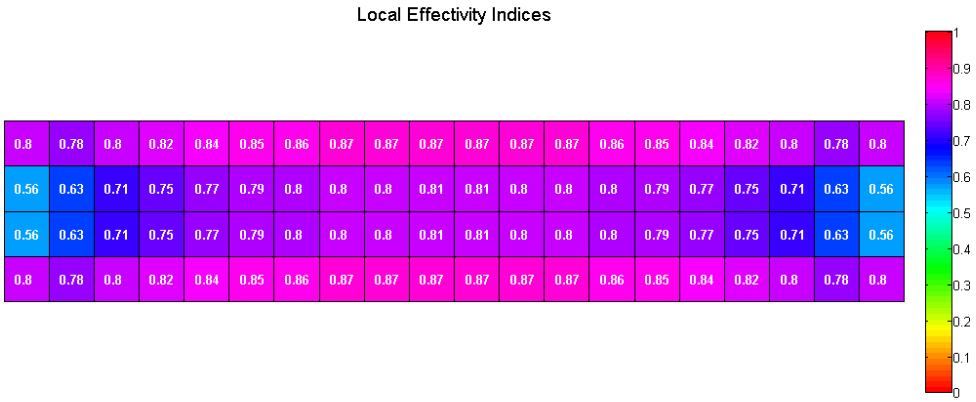

Figure 47. Local effectivity index for implicit fine scale

6.10 Convergence Study: Distorted Meshes

A convergence study involving distorted meshes was also conducted for this problem in order to assess the robustness of the numerical framework. Again, due to the overlap in dimensions for the two beams, we utilized the meshes from Table 7 for this study as well.

The convergence of the standard error norms is shown in Figure 48. The convergence rates of the displacement field are nearly optimal for all element types in both norms; however, the magnitude of the error in the solutions increased slightly from the solutions obtained on uniform meshes, which can be observed from the downward shift of the curves in Figure 48 compared to those in Figure 36. The pressure field experienced deteriorated rates compared to the uniform mesh study. In all cases, the rate for the L_2 norm was one order below the optimum. For the H^1 seminorm, the rates for the quadratic elements were one order below the optimum, and the linear elements exhibited a relative error greater than 1.0. These trends are similar to those observed for the distorted mesh simulations of the cantilever beam problem.

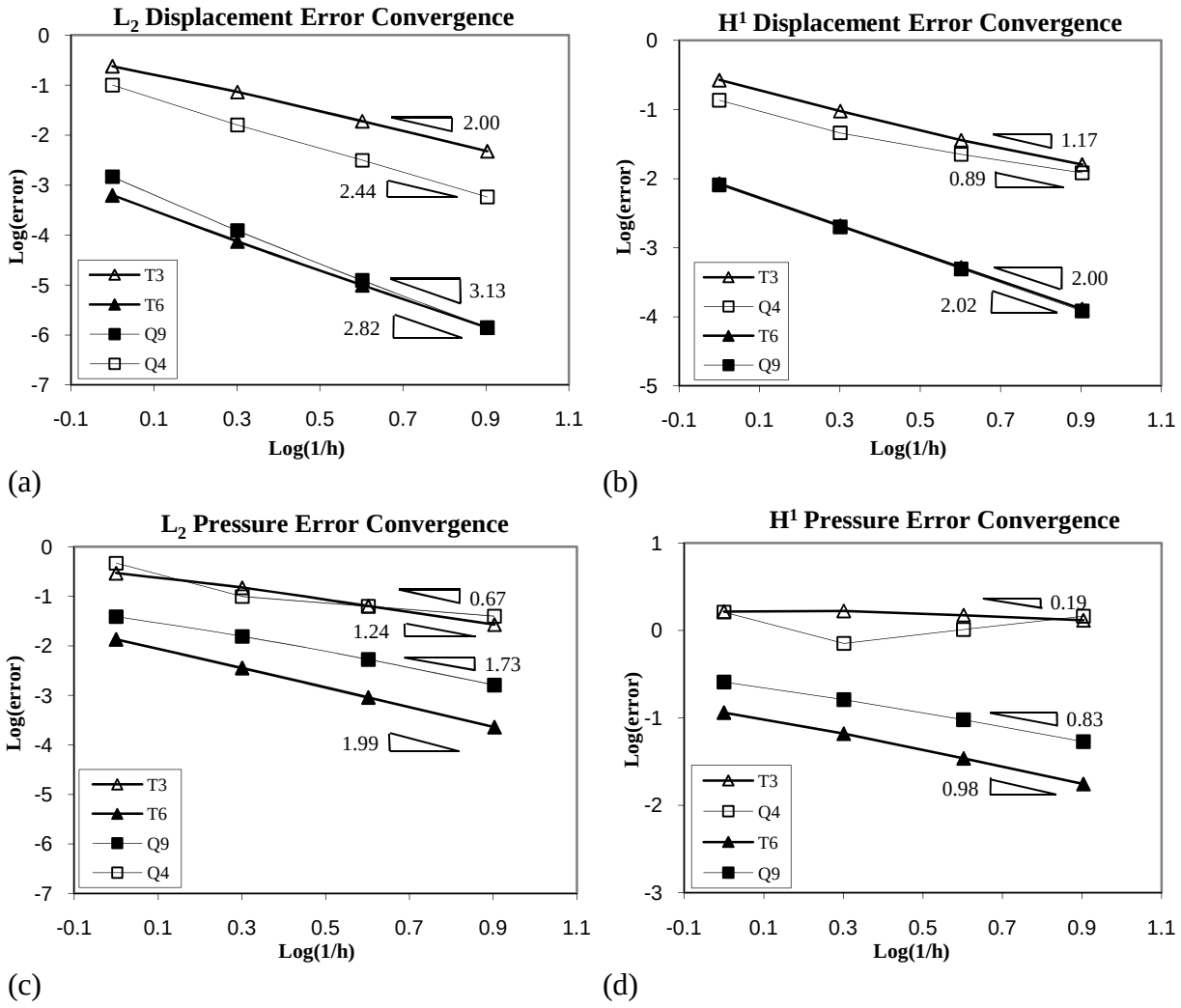

Figure 48. Convergence rates of normalized standard error: (a) L_2 norm of displacement; (b) L_2 norm of pressure; (c) H^1 seminorm of displacement; and (d) H^1 seminorm of pressure

6.11 Error Estimation: Distorted Meshes

This section presents convergence plots of the global norms of the fine scale field $\boldsymbol{u}'$ obtained from the explicit and implicit methods. As can be seen in Figure 49, both the explicit and implicit L_2 error norms converge at the optimal rates of 2.0 for linear elements and 3.0 for quadratic elements. Similarly, the H^1 seminorm converges near the optimal rate for each of the element types. By comparing the error estimates with the standard error in Figure 48 (a) and (b), we observe that the convergence rates of the error estimates parallel those of the standard error. Additionally, the estimated H^1 seminorm in Figure 49 (b) and (d) match closely with the curves in Figure 48. These trends were preserved under significant distortion of the mesh.

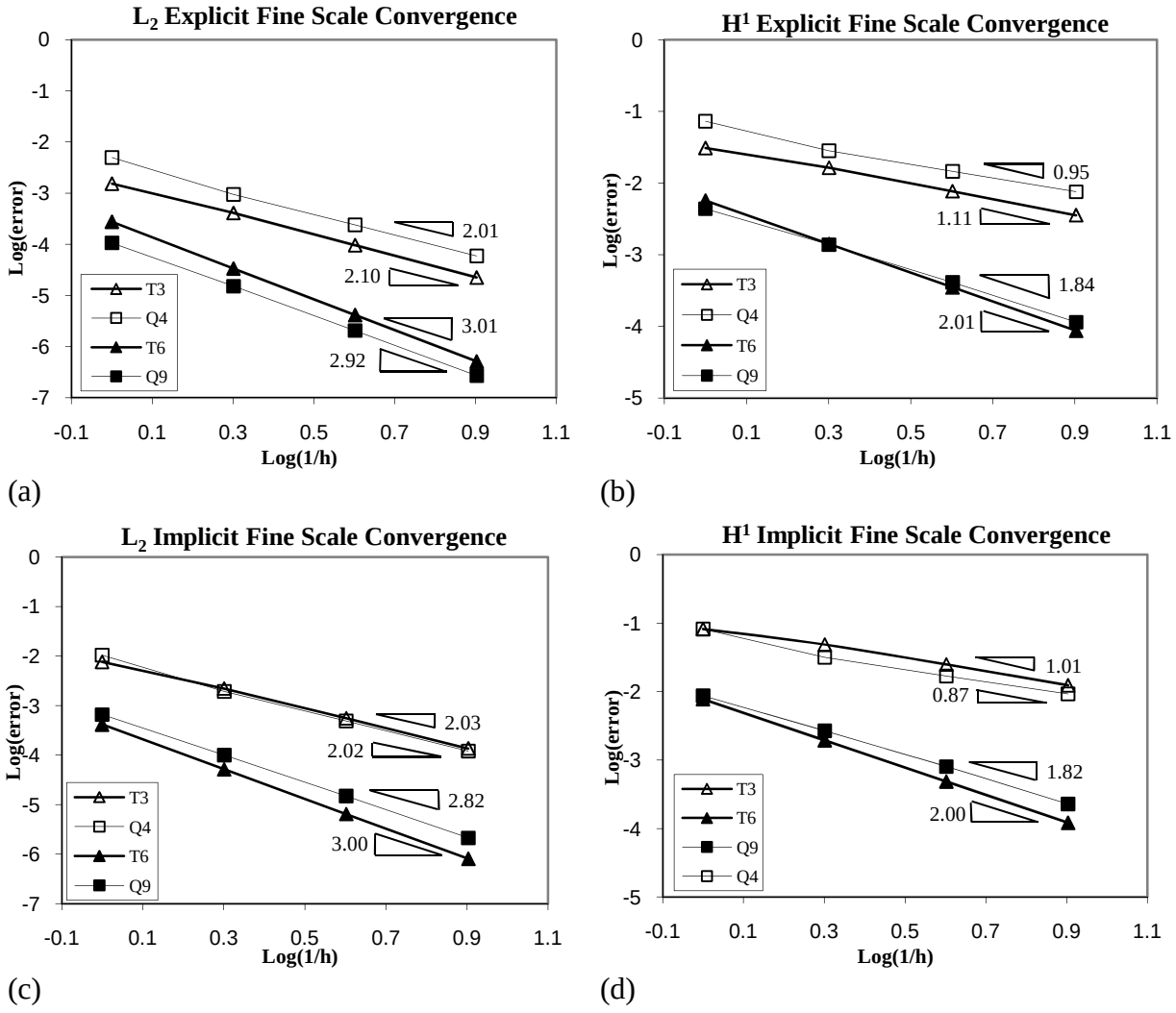

Figure 49. Convergence rates of normalized error estimates: (a) L_2 norm of explicit $\boldsymbol{u}'$; (b) H^1 seminorm of explicit $\boldsymbol{u}'$; (c) L_2 norm of implicit $\boldsymbol{u}'$; and (d) H^1 seminorm of implicit $\boldsymbol{u}'$

Chapter 7: Conclusions

We have demonstrated the application of the Hughes Variational Multiscale framework to the standard weak form of mixed elasticity in order to develop a stabilized finite element method and a posteriori error estimators. Because the method is based on sound variational principles, it produces stable and convergent solutions, as was illustrated by the numerical simulations presented in this work. Additionally, the error estimators developed from this framework provided an accurate representation of the fine scale features of the standard error for the benchmark problem. Thus, this framework represents a unified and consistent methodology for the analysis of elasticity problems involving nearly incompressible media. In our future work, we plan to investigate techniques for estimating the coarse scale trends of the error in the finite element solutions obtained from this framework.

Appendix A

In this section, we present explicit formulas using indicial notation for the HVM Form (4.25) in two-dimensions as a guide for those seeking to implement the method.

Let the discretized approximations of $\boldsymbol{u}$ be represented through a linear combination of basis functions as follows:

$$u_x^h = \sum_{b=1}^{n_{umnp}} N^b u_x^b \tag{A.1}$$

$$u_y^h = \sum_{b=1}^{n_{umnp}} N^b u_y^b \tag{A.2}$$

where n_{umnp} is the number of nodes in the mesh, N^b is the basis function associated with node *b*, and u_x^b, u_y^b are the displacement coefficients or degrees of freedom for node *b*. Similarly, the weighting functions are expressed as:

$$w_x^h = \sum_{a=1}^{n_{umnp}} N^a w_x^a \tag{A.3}$$

$$w_y^h = \sum_{a=1}^{n_{umnp}} N^a w_y^a \tag{A.4}$$

where w_x^a, w_y^a are the displacement weighting function coefficients or degrees of freedom for node *a*. Finally, the pressure field trial and weighting functions are expressed as:

$$p^h = \sum_{d=1}^{n_{umnp}} N^d p^d \tag{A.5}$$

$$q^h = \sum_{c=1}^{n_{umnp}} N^c q^c \tag{A.6}$$

For simplicity, we have assumed equal-order interpolations for the displacement and pressure fields so that the number of basis functions is the same for both fields. For economy, we utilize the comma notation to express the derivative of a function; for example, the partial derivative of w_x^h with respect to *y* is given by

$$w^h_{x,y} = \sum_{a=1}^{n_{umnp}} N^a_{,y} w^a_x \tag{A.7}$$

where $N^a_{,y} = \dfrac{\partial N^a}{\partial y}$. Similarly, $N^a_{,xy} = \dfrac{\partial N^a}{\partial x \partial y}$ is the mixed second partial derivative of N^a. Finally, in indicial notation, the components of a vector are typically numbered rather than assigned a specific coordinate direction so that the vector is not tied to any particular frame of reference and so that the summation of components can be easily expressed. Therefore, in subsequent expressions we will use 1 in place of *x* and 2 in place of *y* to represent the coordinates of the Cartesian system and the associated components of vectors and tensors.

With these expansions, we can return to HVM Form (4.25). Regrouping the terms and separating the equation via the displacement and pressure weighting functions, this equation can be written as:

$$\begin{aligned}
&\int_{\Omega'} \nabla \boldsymbol{w} : 2\mu \boldsymbol{\varepsilon}(\boldsymbol{u}) - \left[2\mu \nabla \cdot \boldsymbol{\varepsilon}(\boldsymbol{w})\right] \cdot \boldsymbol{\tau} \left[2\mu \nabla \cdot \boldsymbol{\varepsilon}(\boldsymbol{u})\right] \mathrm{d}\Omega \\
&+ \int_{\Omega'} (\nabla \cdot \boldsymbol{w})\, p - \left[2\mu \nabla \cdot \boldsymbol{\varepsilon}(\boldsymbol{w})\right] \cdot \boldsymbol{\tau} (\nabla p)\, \mathrm{d}\Omega \\
&= \int_{\Omega'} \boldsymbol{w} \cdot \boldsymbol{b} + 2\mu \nabla \cdot \boldsymbol{\varepsilon}(\boldsymbol{w}) \cdot \boldsymbol{\tau} \boldsymbol{b}\, \mathrm{d}\Omega + \int_{\Gamma_h} \boldsymbol{w} \cdot \boldsymbol{h}\, \mathrm{d}\Gamma
\end{aligned} \tag{A.8}$$

$$\begin{aligned}
&\int_{\Omega'} q(\nabla \cdot \boldsymbol{u}) - (\nabla q) \cdot \boldsymbol{\tau} \left[2\mu \nabla \cdot \boldsymbol{\varepsilon}(\boldsymbol{u})\right] \mathrm{d}\Omega \\
&- \int_{\Omega'} qp/\lambda + (\nabla q) \cdot \boldsymbol{\tau} (\nabla p)\, \mathrm{d}\Omega \\
&= \int_{\Omega'} (\nabla q) \cdot \boldsymbol{\tau} \boldsymbol{b}\, \mathrm{d}\Omega
\end{aligned} \tag{A.9}$$

Sparing the details, the expansions for the trial and weighting functions can be substituted into (A.8) and (A.9) to obtain the following equations:

$$\sum_{a=1}^{n_{umnp}} \sum_{b=1}^{n_{umnp}} w^a_i \bar{K}^{ab}_{ij} u^b_j + \sum_{a=1}^{n_{umnp}} \sum_{d=1}^{n_{umnp}} w^a_i \tilde{K}^{ad}_i p^d = \sum_{a=1}^{n_{umnp}} w^a_i \bar{F}^a_i + \sum_{a=1}^{n_{umnp}} w^a_i F^a_i \tag{A.10}$$

$$\sum_{c=1}^{n_{umnp}} \sum_{b=1}^{n_{umnp}} q^c \tilde{K}^{bc}_j u^b_j + \sum_{c=1}^{n_{umnp}} \sum_{d=1}^{n_{umnp}} q^c \breve{K}^{cd} p^d = \sum_{c=1}^{n_{umnp}} q^c \tilde{F}^c \tag{A.11}$$

where the summation convention is in force for repeated indices *i* and *j*. These equations are indicative of the iconic finite element equation $\boldsymbol{Kd} = \boldsymbol{F}$. In particular, let $\hat{\boldsymbol{u}}$ be the vector of displacement coefficients and $\hat{\boldsymbol{p}}$ be the vector of pressure coefficients; then, equations (A.10) and (A.11) can be expressed as the following system of equations:

$$\begin{bmatrix} \bar{\boldsymbol{K}} & \tilde{\boldsymbol{K}} \\ \tilde{\boldsymbol{K}}^T & \breve{\boldsymbol{K}} \end{bmatrix} \begin{bmatrix} \hat{\boldsymbol{u}} \\ \hat{\boldsymbol{p}} \end{bmatrix} = \begin{bmatrix} \bar{\boldsymbol{F}} + \boldsymbol{F} \\ \tilde{\boldsymbol{F}} \end{bmatrix} \tag{A.12}$$

The formulas for the stiffness matrix terms are given as follows:

$$\begin{aligned} \bar{K}_{ij}^{ab} &= \mu \int_{\Omega'} N_{,k}^a \delta_{ij} N_{,k}^b + N_{,j}^a N_{,i}^b \mathrm{d}\Omega \\ &\quad -\mu^2 \int_{\Omega'} N_{,mm}^a \tau_{ij} N_{,nn}^b + N_{,ik}^a \tau_{kj} N_{,nn}^b + N_{,mm}^a \tau_{il} N_{,lj}^b + N_{,ik}^a \tau_{kl} N_{,lj}^b \, \mathrm{d}\Omega \end{aligned} \tag{A.13}$$

$$\tilde{K}_i^{ad} = \int_{\Omega'} N_{,i}^a N^d \mathrm{d}\Omega - \mu \int_{\Omega'} N_{,mm}^a \tau_{ij} N_{,j}^d + N_{,ik}^a \tau_{kj} N_{,j}^b \, \mathrm{d}\Omega \tag{A.14}$$

$$\breve{K}^{cd} = -\frac{1}{\lambda} \int_{\Omega'} N^c N^d \mathrm{d}\Omega - \int_{\Omega'} N_{,i}^c \tau_{ij} N_{,j}^d \, \mathrm{d}\Omega \tag{A.15}$$

where the summation convention is in force for repeated indices. The formulas for the force vector terms are given as follows:

$$\bar{F}_i^a = \int_{\Omega'} N^a b_i \, \mathrm{d}\Omega + \int_{\Omega'} N_{,mm}^a \tau_{ij} b_j + N_{,ik}^a \tau_{kj} b_j \mathrm{d}\Omega \tag{A.16}$$

$$F_i^a = \int_{\Gamma_h} N^a h_i \, \mathrm{d}\Gamma \tag{A.17}$$

$$\tilde{F}^c = \int_{\Omega'} N_{,i}^c \tau_{ij} b_j \mathrm{d}\Omega \tag{A.18}$$

References

1. M. Ainsworth, J.T. Oden, A unified approach to a posteriori error estimation using element residual methods, Numerische Mathematik. 65 (1993) 23-50.
2. M. Ainsworth, J.T. Oden, A posteriori error estimation in finite element analysis, Computer Methods in Applied Mechanics and Engineering. 142 (1997) 1-88.
3. M. Ainsworth, J.T. Oden, A Posteriori Error Estimation in Finite Element Analysis, John Wiley & Sons, 2000.
4. D.N. Arnold, F. Brezzi, M. Fortin, A stable finite element for the Stokes equations, Calcolo 21 (4) (1984) 337-344.
5. I.M. Babuška, Error Bounds for finite element methods, Numerische Mathematik. 16 (1971) 322-333.
6. I.M. Babuška, A. Miller, A feedback finite element method with a posteriori error estimation Part I. The finite element method and some basic properties of the a posteriori error estimator, Computer Methods in Applied Mechanics and Engineering. 61 (1987) 1-40.
7. I.M. Babuška, W.C. Rheinboldt, A posteriori error estimates for the finite element method, International Journal for Numerical Methods in Engineering. 12 (1978) 1597-1615.
8. I.M. Babuška, W.C. Rheinboldt, Adaptive approaches and reliability estimations in finite element analysis, Computer Methods in Applied Mechanics and Engineering. 17 (1979) 519-540.
9. I.M. Babuška, W.C. Rheinboldt, Analysis of optimal finite element meshes in R^1, Mathematics of Computation. 33 (1979) 435-463.
10. I.M. Babuška, T. Strouboulis, The Finite Element Method and Its Reliability, Oxford University Press, 2001.
11. C. Baiocchi, F. Brezzi and L.P. Franca, Virtual bubbles and the Galerkin/least-squares method, Computer Methods in Applied Mechanics and Engineering. 105 (1993) 125-142.
12. R.E. Bank, A. Weiser, Some a posteriori error estimators for elliptic partial differential equations, Mathematics of Computation. 44 (1985) 283-301.
13. R. Becker, R. Rannacher, An optimal control approach to a posteriori error estimation in finite element methods, Acta Numerica. 10 (2001) 1-102.
14. D. Boffi, L. Gastaldi, Mixed Finite Elements, Compatibility Conditions, and Applications: Lectures given at the C.I.M.E. Summer School held in Cetraro, Italy, Springer, 2008.
15. D. Braess, Finite Elements: Theory, Fast Solvers, and Applications in Solid Mechanics, Cambridge, 2007.
16. D. Braess, O. Klaas, R. Niekamp, E. Stein, F. Wobschal, Error indicators for mixed finite elements in 2-dimensional linear elasticity, Computer Methods in Applied Mechanics and Engineering. 127 (1995) 345-356.
17. F. Brezzi, M. Fortin, Mixed and Hybrid Finite Element Methods, Vol. 15, Springer Series in Computational Mathematics, Springer, 1991.
18. F. Brezzi, L.P. Franca, T.J.R. Hughes, A. Russo, $b = \int g$, Computer Methods in Applied Mechanics and Engineering. 145 (1997) 329-339.

19. F. Brezzi, J. Pitkäranta, On the stabilization of finite element approximations of the Stokes equation, Rept. MAT-A219, Helsinki University of Technology, Institute of Mathematics, Finland. Also in: W. Hackbusch, ed., Efficient Solutions of Elliptic Systems, Proceedings of a GAMM-Seminar, Kiel (Vieweg, Braunschweig, 1985) 11-19.
20. C. Carstensen, J. Thiele, Partition of unity for localization in implicit a posteriori finite element error control for linear elasticity, International Journal for Numerical Methods in Engineering. 73 (2008) 71-95.
21. R. Codina, Stabilization of incompressibility and convection through orthogonal sub-scales in finite element methods, Computer Methods in Applied Mechanics and Engineering. 190 (2000) 1579-1599.
22. M. Crouziex, P.A. Raviart, Conforming and non-conforming finite element methods for solving the stationary Stokes equations, RAIRO Analyse Numerique. 7 (R-3) (1973) 33-76.
23. C.A. Duarte, I.M. Babuška, J.T. Oden, Generalized finite element methods for three-dimensional solid mechanics problems, Computers and Structures, 77 (2000) 215-232.
24. A.H. ElSheikh, S.E. Chidiac, W.S. Smith, A posteriori error estimation based on numerical realization of the variational multiscale method, Computer Methods in Applied Mechanics and Engineering. 197 (2008) 3637-3656.
25. K. Eriksson, C. Johnson, An adaptive finite element method for linear elliptic problems, Mathematics of Computation. 50 (1988) 361-383.
26. K. Eriksson, D. Estep, P. Hansbo, C. Johnson, Introduction to adaptive methods for differential equations, Acta Numerica. 4 (1995) 105-158.
27. L.P. Franca, T.J.R. Hughes, Two classes of mixed finite element methods, Computer Methods in Applied Mechanics and Engineering. 69 (1988) 89-129.
28. L.P. Franca, A. Russo, Unlocking with residual-free bubbles, Computer Methods in Applied Mechanics and Engineering. 142 (1997) 361-364.
29. P.R. Garabedian, Partial Differential Equations, Wiley & Sons, 1964.
30. G. Hauke, M. Doweidar, D. Fuster, A. Gómez, J. Sayas, Application of variational a-posteriori multiscale error estimation to higher-order elements, Computational Mechanics. 38 (2006) 382-389.
31. G. Hauke, M. Doweidar, M. Miana, The multiscale approach to error estimation and adaptivity, Computer Methods in Applied Mechanics and Engineering. 195 (2006) 1573-1593.
32. G. Hauke, M. Doweidar, M. Miana, Proper intrinsic scales for a-posteriori multiscale error estimation, Computer Methods in Applied Mechanics and Engineering. 195 (2006) 3983-4001.
33. G. Hauke, D. Fuster, M. Doweidar, Variational multiscale a-posteriori error estimation for multi-dimensional transport problems, Computer Methods in Applied Mechanics and Engineering. 197 (2008) 2701-2718.
34. P. Hood, C. Taylor, Numerical solution of the Navier-Stokes equations using the finite element technique, Computers and Fluids. 1 (1973) 1-28.
35. T.J.R. Hughes, Multiscale phenomena: Green's functions, the Dirchlet-to-Neumann formulation, subgrid scale models, bubbles, and the origins of stabilized methods, Computer Methods in Applied Mechanics and Engineering. 127 (1995) 387-401.
36. T.J.R. Hughes, The Finite Element Method: Linear Static and Dynamic Finite Element Analysis, Dover, 2000.

37. T.J.R. Hughes, L. Franca, M. Balestra, A new finite element formulation for computational fluid dynamics: V. Circumventing the Babuška-Brezzi condition: a stable Petrov-Galerkin formulation for the Stokes problem accommodating equal-order interpolations, Computer Methods in Applied Mechanics and Engineering. 59 (1986) 85-99.
38. T.J.R. Hughes, G. Feijóo, L. Mazzei, J.-B. Quincy, The variational multiscale method–a paradigm for computational mechanics, Computer Methods in Applied Mechanics and Engineering. 166 (1998) 3-24.
39. S. Korotov, P. Neittaanmäki, S. Repin, A posteriori error estimation of goal-oriented quantities by the superconvergence patch recovery, Journal of Numerical Mathematics. 11 (2003) 33-59.
40. M. Larson, A. Målqvist, Adaptive Variational Multiscale Methods Based on A Posteriori Error Estimation, problems, in: P. Neittaanmäki, T. Rossi, S. Korotov, E. Onate, J. Periaux, D. Knörzer (Eds.), Proceedings of the 4th European Congress on Computational Methods in Applied Sciences and Engineering, 2004.
41. M. Larson, A. Målqvist, Adaptive variational multiscale methods based on a posteriori error estimation: duality techniques for elliptic problems, in: B. Engquist, P. Lötstedt, O. Runborg (Eds.), Lecture Notes in: Computational Science and Engineering, vol. 44, Springer, Berlin, 2005, pp. 181-193.
42. M. Larson, A. Målqvist, Adaptive variational multiscale methods based on a posteriori error estimates: Energy estimates for elliptic problems, Computer Methods in Applied Mechanics and Engineering. 196 (2007) 2313-2324.
43. R. W. Little, Elasticity, Prentice-Hall, 1973.
44. A. Masud, L.P. Franca, A hierarchical multiscale framework for problems with multiscale source terms, Computer Methods in Applied Mechanics and Engineering. 197 (2008) 2692-2700.
45. A. Masud, J. Kwack, A stabilized mixed finite element method for the first-order form of advection–diffusion equation, International Journal for Numerical Methods in Fluids. 57 (2008) 1321-1348.
46. A. Masud, K. Xia, A stabilized mixed finite element method for nearly incompressible elasticity, Journal of Applied Mechanics. 72 (2005) 711-720.
47. P. Morin, R.H. Nochetto, K.G. Siebert, Local problems on stars: a posteriori error estimators, convergence, and performance, Mathematics of Computation. 72 (2003) 1067-1097.
48. K.B. Nakshatrala, A. Masud, K.D. Hjelmstad, On finite element formulations for nearly incompressible linear elasticity, Computational Mechanics. 41 (2008) 547-561.
49. J.T. Oden, Optimal *h-p* finite element methods, Computer Methods in Applied Mechanics and Engineering. 112 (1994) 309-331.
50. N. Parés, P. Díez, A. Huerta, Subdomain-based flux-free a posteriori error estimators, Computer Methods in Applied Mechanics and Engineering. 195 (2006) 297-323.
51. A. Russo, A posteriors error estimators via bubble functions, Mathematical Models and Methods in Applied Sciences. 6 (1996) 33-41.
52. M. H. Sadd, Elasticity: Theory, Applications, and Numerics, Elsevier, 2005.
53. J.C. Simo, M.S. Rafai, A class of mixed assumed strain methods and the method of incompatible modes, International Journal for Numerical Methods in Engineering. 29 (1900) 27-57.
54. W. Strauss, Partial Differential Equations: An Introduction, Wiley & Sons, 2008.

55. R. Verfürth, A posteriori error estimators for the Stokes equations, Numerische Mathematik. 55 (1989) 309-325.
56. R. Verfürth, A Review of A Posteriori Error Estimation and Adaptive Mesh-Refinement Techniques, Wiley-Teubner, 1996.
57. N. Yan, A. Zhou, Gradient recovery type a posteriori error estimates for finite element approximations on irregular meshes, Computer Methods in Applied Mechanics and Engineering. 190 (2011) 4289-4299.
58. O.C. Zienkiewicz, J.Z. Zhu, A simple error estimator in the finite element method, International Journal for Numerical Methods in Engineering. 24 (1987) 337-357.
59. O.C. Zienkiewicz, J.Z. Zhu, Adaptivity and mesh generation, International Journal for Numerical Methods in Engineering. 32 (1991) 783-810.
60. O.C. Zienkiewicz, J.Z. Zhu, The superconvergent patch recovery and a posteriori error estimates. Part 1: The recovery technique, International Journal for Numerical Methods in Engineering. 33 (1992) 1331-1364.
61. O.C. Zienkiewicz, J.Z. Zhu, The superconvergent patch recovery and a posteriori error estimates. Part 2: Error estimates and adaptivity, International Journal for Numerical Methods in Engineering. 33 (1992) 1365-1382.